DEVELOPMENT AND ASSESSMENT OF ADVANCED QUANTITATIVE BODY DIFFUSION WEIGHTED MRI

By

Yuxin Zhang

A dissertation submitted in partial fulfillment of

the requirements for the degree of

Doctor of Philosophy

(Medical Physics)

at the

UNIVERSITY OF WISCONSIN-MADISON

2021

Date of final oral examination: April 09, 2021

The dissertation is approved by the following members of the Final Oral Committee:

Diego Hernando, Assistant Professor, Medical Physics, Radiology and Biomedical Engineering

Scott Reeder, Professor, Biomedical Engineering, Medical Physics and Radiology

Walter Block, Professor, Biomedical Engineering and Medical Physics

Oliver Wieben, Professor, Medical Physics, Radiology and Biomedical Engineering

Shane Wells, Associate Professor, Radiology

Abstract

Diffusion-Weighted MRI (DW-MRI) has a unique ability to non-invasively probe tissue microstructure without the need for ionizing radiation or contrast agent administration. This ability makes DW-MRI a powerful tool for the detection, staging, and treatment monitoring of cancer. However, DWI remains limited by multiple imaging challenges, especially in extracranial organs such as liver and prostate. The major challenges include: 1) relatively long acquisition time in multi-parametric mapping, 2), T2-shinethrough effect 3) artifacts caused by tissue motion and 4) image distortions arising from local magnetic field heterogeneities. In this thesis, technical developments are introduced to address these challenges in prostate and liver DWI. A STimulated-Echo based mapping (STEM) approach is developed and optimized to achieve simultaneous T1, T2 and ADC mapping within five minutes. The STE-DWI sequence is also evaluated in patients with prostate cancer, in order to achieve high contrast-to-noise ratio (CNR) with moderate b-values. To address the motion artifacts in liver DWI caused by cardiac motion, a M1-Optimized Diffusion Imaging (MODI) method is proposed to compensate the motion sensitivity while maintaining the blood-suppression effect using optimized diffusion encoding gradient waveforms. Additionally, reduced Field-of-View and multi-shot EPI acquisitions are assessed in prostate DWI to reduce the geometric distortion artifacts. Finally, a synergistic combination of MODI and multi-shot EPI acquisitions are proposed for motion-robust, reduced-distortion liver DWI. In this work, the feasibility, quantitative accuracy and reproducibility of the proposed techniques are evaluated in simulations, quantitative diffusion phantoms, healthy volunteers and a small number of patients with known or suspected cancer.

Acknowledgements

I have been so lucky to be a PhD student at UW MRI group, to be surrounded and mentored by so many talented people, and to be a member of this big supportive family.

To my PhD advisor, Dr. Diego Hernando –

Right now, every single piece of memory over the last five years is lingering in my head. All those small pieces of care, support, encouragement, and guidance, which seemed so trivial back then, comes together to make me who I am today. Maybe they were just small things to you, but the Thanksgiving night we spent at your house, the countless ‘go for it’ ‘great plan’ you said to me, and even when once you helped me correct my email language, were what made the five-year Wisconsin life so warm.

It is a long journey to train a PhD from scratch, especially an international student. Five-year, for someone who just got out of college and stepped onto a foreign land to start a new life, is a short and long time. Short, in the sense that it’s going to be such a sharp learning curve, from knowing nothing about American culture, PhD life, and career, to being a mature adult who is able to think and work independently, knows clearly what I want and who I want to become. Long, simply because it is five years and a lot can happen to define my path. Thus, it is so important to be able to have an advisor like you, who is a mentor to me and to other students, not only about research and science, but also about communications, attitude of life and how to be a decent person.

It’s time to graduate. But I know it’s not an end of this mentorship. Instead, it’s the very beginning of all the positive impacts you had on me to take effect, no matter where I am.

All in all, thank you!

To my co-advisor, Dr. Scott Reeder and my PhD committee members, Dr. Shane Wells, Dr. Oliver Wieben, and Dr. Wally Block -

I am very fortunate to have your mentorship and endless support over the past five years. Thank you, Scott, for motivating me with your passion and attitude in scientific research and sharing your insights with me whenever I have questions or concerns. Thank you, Shane, for your valuable input in my research and career path. I truly learned a lot from our interactions and discussions. Thank you, Oliver and Wally, for providing great insights in my projects, as well as generously offering resources for my next step.

To my friends, my dear labmates at LIRP and QIML -

You are the ones who closely witnessed my step by step growth. I still remember how excited I was when first meeting some of you in Singapore, back in early 2016; our first Pokémon trip together to the picnic point; our daily lunch in the cafeteria or the patio; our wonderful travel together in Hawaii, Paris, and Montreal… All of these made my PhD journey so beautiful. Special thanks to Nathan Roberts, Dr. Ante Zhu, Dr. Curtis Wiens and Dr. Timothy Colgan for guiding me patiently from my first day in lab. Thank you to Dr. Ali Pirasteh, Dr. Matthias Muhler and Dr. Jitka Starekova for supplementing clinic aspects to this thesis. Special thanks to Óscar Peña-Nogales, Ruiqi Geng, Iñaki Rabanillo Viloria, Dr. David Rutkowski, Colin Kim, James Rice, and Dr. Alejandro Roldan for your contributions to this thesis. I am also grateful to Dr. David Harris and Ashley Hinrichs for their assistance and support during my PhD. Additionally, I would also like to thank Ruiyang Zhao, Collin Buelo, Dr. Debra Horng, Dr. Gesine Knobloch, Ruvini Navaratna, Yavuz Muslu, Zihan Wang, Dr. Sasha Archer and Dr. Greg Simchick for their friendship and collaboration. Being in the lab is a truly enjoyable experience. I hope the collaboration will continue and the friendship will last long.

To the UW MRI group and GE Healthcare collaborators -

It's been a great honor to work in the UW MRI group where I had chances to work with brilliant scientists, talented students, and friendly staff. I would like to express my appreciation to Dr. Jim Holmes and Dr. Kevin Johnson for their help in my PSD programming and their insights in my research projects. I also want to thank Dr. Fang Liu, Dr. David Mummy, Pingni Wang, Jeff Kammerman, Luis Torres, Katie Carey, Mulan Jen, and every friend I have made in this group. And my great gratitude to all MRI techs and patient coordinators, Kelli Hellenbrand, Sara John, Jenelle Grogan, Haley Jarvi, Martha Garcia, Molly Ellertson and Frances Theisen, who support this research. This thesis would not have been possible without the research support from GE Healthcare. Thanks to Dr. Arnaud Guidon, Dr. Tim Sprenger, Dr. Ty Cashen for their support on many MRI pulse sequence and reconstruction problems. I am also grateful to all supports I obtain from Department of Radiology and Medical Physics in UW-Madison.

Also, I want to thank my past advisors Dr. Kui Ying and Dr. Will Grissom who introduced me to the MRI field. I started to learn MR physics, write MR pulse sequence and reconstruction codes when I was in their labs.

Lastly, I want to thank my family, my mom Yue Li, dad Xiaokun Zhang, my dear husband Chuhan Gao, my beloved friend Yunyingying Xu for your endless love and support throughout my entire life. You are the ones who made sure I could pursue my dream without worries. Then to my special little babies, Echo and Proton, you are my source of happiness, always staying by my side meowing and giving me headache. But I love you two so much. Also many thanks to my friends who share my happiness and sadness with me during the pandemic, Ante, Wenying Wang, Huiwen Luo, Yao Jiang, Feiran Li, Cong Cao, Yu Xu, and Kaiwen Guo.

Table of Contents

List of Figures

List of Tables

List of Abbreviations

DWI – Diffusion Weighted Imaging

ADC – Apparent Diffusion Coefficient

EPI – Echo-Planer Imaging

DESS – Dual-Echo Steady State

MRF – MRI Fingerprinting

TE – Echo Time

TM – Mixing Time

STEM – Stimulated-Echo based Mapping

M1 – First Moment

M2 – Second Moment

MODI – M1-Optimized Diffusion Imaging

MONO – Monopolar

ssEPI – Single-Shot EPI

rFOV – reduced Field of View

msEPI – Multi-Shot EPI

SE – Spin Echo

PCa – Prostate Cancer

PZ – Peripheral zone

CNR – Contrast-to-Noise Ratio

BPH - Benign Prostatic Hyperplasia

SNR – Signal-to-Noise Ratio

Chapter

1. Introduction of Diffusion Weighted MRI

1.1 Body Diffusion Weighted MRI

Diffusion, in biological tissue, describes the Brownian motion of water molecules. The characterization of diffusion has the capability to probe the microstructural changes of tissue, thus distinguish lesions from normal tissue. Diffusion Weighed MRI has a unique ability to non-invasively characterize diffusion without the need for ionizing radiation or contrast agent administration[1].

The most widely used Diffusion Weighted Imaging (DWI) technique[2,3] applies a pair of diffusion encoding gradients that are sensitive to diffusion to attenuate the transverse magnetization, where the first gradient lobe dephases the spins and the second lobe rephrases them. In the case of stationary spins, the effect of the two encoding gradients will be cancelled out; however, with diffusion, spins are experiencing different magnetic fields as they move around different locations, thus have incomplete rephrasing and generate attenuated signal. With this mechanism, the diffusion weighted signal can be expressed as

$$S(b, D) = S_0 e^{-b \cdot D}, \quad (1)$$

where S_0 is the signal without diffusion, b is the b-value of the sequence and D is the diffusion coefficient. In reality, the true diffusion coefficient is not able to be measured given the limited imaging resolution. Thus, apparent diffusion coefficient (ADC) is widely used to represent D and quantify the overall diffusion coefficient in a given voxel. The b-value is defined by the following equation:

$$b = \gamma^2 \int_0^{T_{diff}} \left(\int_0^t G(t)dt \right)^2 dt, \quad (2)$$

where γ is the gyromagnetic ratio of proton, T_{diff} is the time of the end of diffusion encoding and $G(t)$ is the gradient strength of the diffusion encoding gradient over time. In a typical Stejskal–Tanner DWI sequence, b-value equation can be simplified as

$$b = (\gamma \cdot G \cdot \delta)^2 \left(\Delta - \frac{\delta}{3} \right). \quad (3)$$

In this case, the b-value is determined directly by the strength of diffusion gradients G, diffusion time Δ (i.e. the duration between the start of the first diffusion lobe and the start of the second diffusion lobe), as well as the duration of one diffusion coding lobe δ.

In the past decades, DWI has shown promising value in the body as a powerful tool for the detection, staging, and treatment monitoring of cancer[4–6]. For example, qualitative use of DW-MRI has been the standard routine for multi-parametric prostate imaging[7,8]. The correlation between quantitative diffusion (i.e. ADC measurements) and Gleason score in prostate cancer patients have also been thoroughly investigated[9]. The application of DW-MRI is less popular and robust in the liver in clinics but DW-MRI has been shown to be a potential biomarker for liver metastases. For example, Woo-Suk et al. has demonstrated the high diagnostic accuracy and high sensitivity of combined DWI and gadoxate disodium (Gd-EOB-DTPA) imaging in patients with

colorectal liver metastases[10]. Researchers have also evaluated the accuracy and sensitivity of DW-MRI and different DW-MRI models in assessing post-therapy response[11,12].

1.2 Challenges of Body Diffusion Weighted MRI

DWI has been shown to be a potential biomarker due to its highly sensitivity to tissue cellularity, and ability to reveal lesions that are otherwise undetectable. However, despite continued technical developments over the past three decades, diffusion MRI remains limited in body applications by the following imaging challenges[4,13], including 1) relatively long acquisition time in multi-parametric mapping, 2), T2-shinethrough effect 3) artifacts caused by tissue motion and 4) image distortions arising from local magnetic field heterogeneities.

1.2.1 Rapid Multi-Parametric Mapping

Quantitative MRI multi-parametric mapping methods have the potential to enable improved diagnosis and treatment monitoring for multiple conditions, as well as providing imaging-based biomarkers for drug-development clinical trials. For example, quantitative T1 and T2 mapping have potential in the diagnosis of brain[14] and cardiac[15] diseases. Additionally, quantitative mapping of T1 or T2, together with ADC has applications in the diagnosis and treatment monitoring of prostate disease[16,17] and breast cancer[18]. Mapping of relaxation and diffusion parameters may enable advanced characterization of healthy and diseased tissue, with emerging clinical and research applications[19,20]. Indeed, Importantly, it is essential that such quantitative MRI methods are reproducible (both longitudinally and across sites) and that they are clinically feasible (e.g. that they can be acquired within a moderate scan time).

Mapping of relaxation and diffusion parameters is typically performed using multiple separate acquisitions, including one or several relaxometry pulse sequences[21–23] and a separate DWI sequence[2]. However, the need for multiple separate acquisitions is often not practical for clinical applications, due to long acquisition times and the challenges of obtaining co-registered parametric maps. Therefore, simultaneous mapping of relaxation (e.g., T1 and T2) and diffusion (e.g., ADC) parameters based on a single acquisition sequence is highly desirable in order to provide rapid and co-registered quantitative multi-parametric MRI.

Previous studies have explored simultaneous T1, T2 and ADC mapping with methods including diffusion-weighted Dual-Echo Steady State (DESS)[24] and MR Fingerprinting (MRF)[25]. However, these previously proposed techniques face substantial limitations. For the DESS method, the signal from steady-state sequence is complicated to model, especially with diffusion encoding, which may result in inaccuracy and large variance in diffusion measurements[24]. Although preliminary results have shown promise for MRF with simultaneous ADC mapping, probing diffusion within the MRF framework is challenging and may be subject to multiple confounding factors[26,27].

Therefore, there is an unmet need for a method that enables rapid and co-registered simultaneous mapping of T1, T2 and ADC that is able to overcome the limitations of previous techniques. In this work, we will develop a rapid and co-registered simultaneous T1, T2 and ADC mapping method by adding T1 and T2 mapping to a diffusion MRI sequence (which by design addresses the difficulties of diffusion MRI). Specifically, this proposal will use the stimulated-echo DWI sequence[28] (**Figure 1**), which enables the modulation of T1, T2 and diffusion weighting by varying the mixing time (TM), echo time (TE) and b-values, respectively. The feasibility and

reproducibility of this technique will be evaluated in diffusion phantoms as well as brain imaging and prostate imaging.

1.2.2 T2-shinethrough Effect in Prostate DWI

Prostate cancer is the second most frequent cancer of men worldwide[29,30]. Increasingly, multiparametric MRI is used to diagnosis and stage prostate cancer (PCa)[31–33]. The multiparametric MRI sequences described in the PI-RADS 2.1 guidelines[31] include T2-weighted imaging, diffusion-weighted imaging (DWI), as well as T1-weighted dynamic contrast enhanced imaging which is also often performed. Correlating T2-weighted images with DWI is essential in the diagnosis of prostate cancer, particularly in the peripheral zone, due to its sensitivity to tissue microstructure.

DWI is routinely performed using conventional Spin Echo (SE) DWI sequences as part of clinical prostate MRI exams. However, no consensus has been reached in terms of the choice of b-values to balance cancer conspicuity in the peripheral zone (PZ) and image quality[34–38]. High b-values larger than 1000 s/mm^2 have been shown to provide improved lesion conspicuity[34–36,38,39]. However, the echo time (TE) of SE DWI is substantially increased when the b-value is increased, which leads to T2 shine-through effects and reduced Signal-to-Noise Ratio (SNR), as well as other imaging artifacts[40]. In contrast, SE DWI with moderate b-values ranging from 800 s/mm^2 to 1000 s/mm^2 provides reduced contrast between PCa and normal tissue, but higher SNR and lower artifacts. Additionally, moderate b-values enable reliable mapping of apparent diffusion coefficient (ADC) with improved ADC contrast between PCa and normal tissue[36]. Due to these tradeoffs, many clinical sites acquire two DWI series[31]: one with high b-value (1500 s/mm^2) to

optimize the Contrast-to-Noise Ratio (CNR) between PCa and healthy PZ, and one with moderate b-value (800 s/mm^2) to provide reliable ADC maps.

In order to provide high CNR between PCa and normal PZ (as enabled by high b-value DWI) while maintaining the image quality of moderate b-values, a number of previous studies attempted to overcome this tradeoff by using various approaches including: DWI ratio calculation[38], synthetic DWI[41], DWI subtraction[42] and other post-processing methods. However, there is an unmet need for methods that overcome this tradeoff directly through the DWI acquisition.

Stimulated-Echo (STE) DWI has the potential to overcome this tradeoff. Compared to standard SE DWI acquisitions, STE DWI[28] is able to achieve the same b-value with shorter TE than SE DWI by slightly increasing the mixing time (TM) (**Figure 1**). Consequently, STE DWI enables reduced T2 shine-through effect, potentially leading to high CNR between PCa and normal PZ, while maintaining higher SNR and reliable ADC mapping compared to high b-value SE DWI. For these reasons, STE DWI may be able to overcome the limitations of SE DWI for prostate imaging, combining the advantages of low b-value and high b-value SE DWI acquisitions.

Therefore, the purpose of this study is to propose and evaluate a STE DWI acquisition strategy for high-CNR imaging of prostate cancer while also enabling reliable ADC mapping.

1.2.3 Motion Artifacts in Liver DWI

Physiological (e.g. respiratory and cardiac) motion presents a fundamental challenge for reliable diffusion MRI in various abdominal organs, particularly the liver. The presence of motion between multiple DW images (e.g. with different b-values, diffusion directions or repetitions) can lead to mis-registration and is often mitigated by the use of respiratory-gated or breath-held scans.

However, the presence of motion within a single image acquisition, particularly non-rigid tissue motion during the application of DW gradients, will also introduce motion artifacts to DW images.

In conventional DWI sequences, diffusion encoding is typically performed with a monopolar gradient waveform[2] operating at hardware limits, which is designed to be sensitive to microscopic motion. However, because of the motion sensitivity of diffusion encoding sequences, it is also sensitive to non-rigid bulk tissue motion. This non-rigid bulk motion will introduce additional phase dispersion in liver DWI signals, particularly in the left lobe as a result of cardiac motion[43,44]. This motion-induced phase dispersion results in signal voids in the DW images (Fig.2) and bias in subsequent quantitative diffusion measurements, including overestimation of ADC. Importantly, these non-rigid tissue motion related signal voids (e.g. arising from cardiac related motion in the left lobe of the liver) are often not suitable for mitigation using gating or breath-holds.

In previous studies, advanced DW gradient waveform design techniques have been proposed to provide first-moment (M1) and/or second-moment (M2) motion moment-nulled DWI[45,46]. However, these moment-nulled gradient waveforms also compensate the signal from moving blood, which is nulled in traditional liver DWI. This lack of blood signal nulling will result in bright spots from blood vessels and bias in ADC measurements. Consequently, methods to mitigate motion-induced signal voids while maintaining blood suppression are needed in order to obtain accurate and reproducible DWI of the abdomen.

In summary, development of a motion-robust, blood-suppressed DWI of liver with optimized diffusion encoding waveforms may enable reliable diagnosis as well as accurate and reproducible ADC measurements across the entire liver. In this work, we will propose a technique that formulates the design of diffusion gradient waveforms as an optimization problem (e.g.

minimizing the achievable echo time), subject to a set of constraints (as described in detail in the Approach). Compared to the previously proposed motion moment-nulled diffusion waveform designs, where unsuppressed blood signal will confound the assessment and detection of true focal lesions[47], this proposal will, for the first time, develop and evaluate a M1-Optimized Diffusion Imaging (MODI) technique for motion-robust and blood-suppressed liver DWI with optimized diffusion gradient waveforms.

1.2.4 Image Distortions in Body DWI

DWI is typically performed with single-shot echo planar imaging (ssEPI) techniques because of their reliability and short acquisition time. However, ssEPI often suffers from severe image distortion due to the presence of susceptibility-related field inhomogeneity. Distortion in qualitative DW images will result in false diagnosis or inaccurate localization of lesions and will also introduce bias in quantitative diffusion measurements.

Novel pulse sequences based on reduced field-of-view (rFOV)[48–50] and multi-shot EPI (msEPI)[51–53] acquisitions have been proposed to reduce these image distortions by enabling shorter EPI readout times. Specifically, rFOV enables a shorter EPI echo-train length by applying a spatially-selective RF pulse to excite a limited FOV in the phase encoding direction. Alternatively, msEPI acquires multiple shots (where each shot requires a shorter echo train with reduced readout time) in the phase-encoding direction to reduce distortion artifacts. Importantly, both rFOV and msEPI enable DWI imaging with higher resolution and higher overall image quality including greater resolvable spatial resolution and reduced distortions[50,51].

However, the effectiveness of distortion reduction techniques in body DWI, especially msEPI, has not been fully investigated. In this work, by addressing the remaining challenges

through optimization of the msEPI acquisition and reconstruction, we aim to provide diffusion MRI of the abdomen and pelvis with unprecedented image quality and quantitative reproducibility.

In this study, we will apply msEPI to abdominal and pelvic DWI, as well as evaluate and optimize its robustness and reproducibility in the body. This proposal will also evaluate, for the first time, the accuracy and reproducibility of quantitative diffusion measurements from advanced low-distortion msEPI acquisition and reconstruction. Furthermore, we will combine motion-robust diffusion waveform design and msEPI techniques in the abdomen in order to enable motion-robust diffusion imaging with high spatial resolution and minimized image distortions. By optimizing the acquisition and reconstruction, we aim to provide diffusion MRI of the abdomen with unprecedented image quality and quantitative reproducibility.

1.3 Innovation

The primary innovation of this proposal is the development of novel diffusion imaging techniques that enable simultaneous co-registered T1, T2 and ADC mapping, motion-robust and blood-suppressed abdominal DWI, low-distortion, high-resolution body DWI, as well as high CNR Prostate DWI with reliable ADC mapping. The innovations are summarized below:

Simultaneous T1, T2 and ADC mapping Based on Stimulated-echo DWI. This is the first study to develop rapid and co-registered simultaneous T1, T2 and ADC mapping by adding T1 and T2 mapping to a diffusion MRI sequence (which by design addresses the difficulties of diffusion MRI). Specifically, this proposal will use the stimulated-echo DWI sequence, which enables the modulation of T1, T2 and diffusion weighting by varying the mixing time (TM), echo time (TE) and b-values, respectively.

High-SNR, High-CNR Imaging of Prostate Cancer with Stimulated-Echo DWI. This work is the first to propose and evaluate a STE DWI acquisition strategy for high-CNR imaging of prostate cancer while also enabling reliable ADC mapping.

Optimized Motion-robust, Blood-suppressed Diffusion Gradient Waveforms. This work will, for the first time, develop and evaluate a M1-Optimized Diffusion Imaging (MODI) technique for motion-robust and blood-suppressed liver DWI with optimized diffusion gradient waveforms.

Low-distortion Multi-shot EPI DWI. This work will apply msEPI to abdominal and pelvic DWI, as well as evaluate and optimize its robustness and reproducibility in the body. This proposal will also evaluate, for the first time, the accuracy and reproducibility of quantitative diffusion measurements from advanced low-distortion msEPI acquisition and reconstruction.

Combined Motion-robust, Low-distortion, High-resolution Abdominal DWI. This is the first application of combined motion-robust diffusion waveform design and msEPI techniques in the abdomen in order to enable motion-robust diffusion imaging with high spatial resolution and minimized image distortions.

1.4 Thesis Outline

In this study, we aim to develop and validate novel DWI methods to address these challenges respectively, i.e. 1) fast simultaneous T1, T2 and ADC mapping acquisition, 2) DWI with reduced T2-shinethrough effect, and 3) high-resolution, low-distortion, motion-robust, and blood-suppressed DWI.

In accordance with the aforementioned aims of this work, the thesis is organized as follows:

- **Chapter 2**: A Stimulated-Echo Based Mapping technique for simultaneous quantification of T1, T2 and ADC is developed and optimized. Phantom experiments, healthy volunteer studies in brain and prostate imaging, as well as a patient study with a suspected prostate cancer patient cohort, are described to demonstrate the feasibility and reproducibility of the proposed approach.
- **Chapter 3**: Stimulated-Echo DWI is evaluated to provide high-CNR prostate diffusion images at moderate b-values. Digital simulation was performed as a proof-of-concept. *In-vivo* experiment in patients with suspected prostate cancer are described to assess the SNR, CNR, as well as lesion detectability of Stimulated-Echo DWI, in comparison to the conventional Spin-Echo DWI technique.
- **Chapter 4**: A M1-Optimized Diffusion Imaging technique is introduced to achieve both motion-robustness and blood-suppression effect in liver DW-MRI. Theory and practical considerations of the diffusion encoding gradient waveform design is explained. Healthy volunteer experiments are described to evaluate the feasibility, quantitative accuracy and reproducibility of the proposed method.
- **Chapter 5**: Two distortion-reducing DWI techniques, reduced FOV and multi-shot EPI, are evaluated and compared in prostate imaging, both qualitatively and quantitatively. Diffusion phantom experiment, healthy volunteer study and patient study are described do demonstrate the two hypotheses: 1) both reduced FOV and multi-shot EPI acquisitions are able to reduce the distortion artifacts, and 2) both sequences are able to maintain clinically accurate and reproducible quantitative ADC measurements.
- **Chapter 6**: A synergy between motion-robust diffusion encoding gradient waveform design and distortion-reducing multi-shot EPI techniques is hypothesized and tested in this

chapter. Anthropomorphic liver phantom validation is performed with highly controlled experiment setup. Healthy volunteer experiments in liver DWI are also described to further demonstrate the synergetic effect and the reproducibility of the combined approach.

- **Chapter 7**: A final summary of this work and discusses on potential future works are described.

Chapter

2. Stimulated-Echo based Mapping (STEM) of T1, T2 and Apparent Diffusion Coefficient[1]

2.1 Purpose

In this section, we aim to address the challenge discussed in **Section 1.2.1**. A STimulated-Echo based Mapping (STEM) method is proposed for rapid and co-registered simultaneous mapping of T1, T2 and ADC. The feasibility, accuracy, and protocol optimization of STEM are evaluated in diffusion phantoms, brain tissues and prostate tissues of healthy volunteers.

[1] This work has been published in: Zhang Y, Wells SA, Hernando D. Stimulated-Echo based Mapping (STEM) of T1, T2 and Apparent Diffusion Coefficient: Validation and Protocol Optimization. *Magn Reson Med.* 2019;81(1):167-181.

2.2 Theory

2.2.1 STimulated-Echo DWI Acquisition

The proposed STEM acquisition is based on the STE-DWI sequence[28], as shown in **Figure 1**. Compared to a SE-DWI sequence, STE-DWI uses a pair of 90°-pulses instead of a 180°-pulse to select the stimulated echo pathway, with an adjustable TM in between. In this study, multiple STE images with various values of TM, TE, and b-values are acquired to obtain different T1, T2 and diffusion contrasts. In this study, TR is fixed for each TM, TE and b-value combination.

2.2.2 Signal Model

In this work, the signal from a STE-DWI acquisition is modeled as four exponential decays, including T1 dependence from repetition time (TR), T1-weighting from TM, T2-weighting from TE and diffusion-weighting from b-value. The acquired STEM signal is modeled as

$$S = A\left(1 - e^{-\frac{TR_{eff}}{T1}}\right)e^{\left(-\frac{TM}{T1}\right)}e^{\left(-\frac{TE}{T2}\right)}e^{(-bADC)}, \quad (4)$$

where

$$TR_{eff} = TR - TM - \frac{TE}{2}. \quad (5)$$

Multiple images with different TM, TE and b-value combinations are used to fit the signal model. In the proposed method, T1 relaxation, T2 relaxation and ADC, as well as proton density weighted maps A, are jointly estimated by voxel-wise non-linear least-squares fitting of **Equation 4**.

More sophisticated models including non-Gaussian diffusion[54,55] and multi-compartment models[30,56,57] may also be feasible from the STEM acquisitions. However, the scope of this study is restricted to the model in **Equation 4** for simplicity.

2.3 Methods

2.3.1 Phantom Validation

A twelve-vial (50mL each) T1/T2/diffusion phantom was constructed by mixing acetone (as a signal source) with various concentrations of DI water (to modulate the ADC of acetone) and $MnCl_2$ (to modulate both T1 and T2 of acetone)[58]. Images were acquired at room temperature on a 3T scanner (Discovery MR750, GE Healthcare, Waukesha, WI) with a 32-channel Torso coil (GE Healthcare, Waukesha, WI). The proposed STEM acquisition was obtained with four TM-TE combinations, each with six b-values. Total acquisition time for STEM images was 8 minutes. Additionally, reference T1[21], T2 and ADC maps were acquired (see details in **Table 1**). Quantitative T1, T2 and ADC maps were calculated from the STEM images following the signal model described in **Equation 4**. Measurements were made from each quantitative map using a $1cm^2$ region-of-interest (ROI) within each vial.

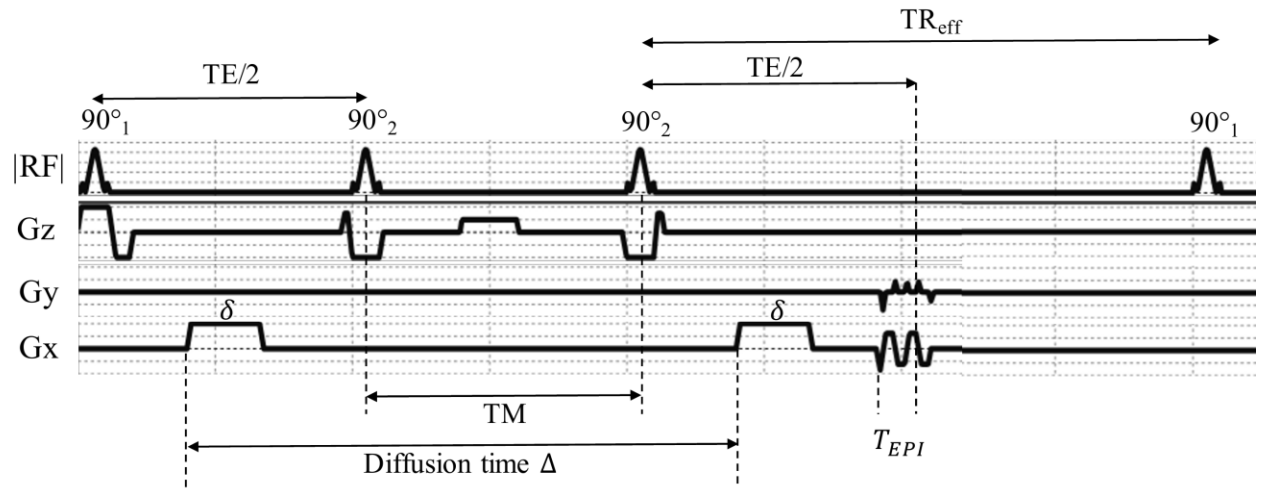

Figure 1. Sequence profile and timing of Stimulated-Echo (STE) DWI. δ is the duration of each diffusion lobe, Δ is the diffusion time and T_{EPI} is the time between the start of EPI readout to TE.

Brain Imaging

After IRB approval and informed written consent, healthy volunteers (n=8) were scanned at the 3T scanner with an eight-channel head coil (GE Healthcare, Waukesha, WI) for brain mapping. The STEM acquisitions and reference T1, T2 and ADC mapping sequences were performed in each volunteer with interleaved slices were acquired within a TR (detailed imaging protocol shown in **Table 2**(a)). A single diffusion direction was used in this early stage study to save acquisition time. Note that the ADC maps from a single STE-DWI acquisition (TE=40ms, TM=100ms) instead of Spin-Echo DWI were used as reference to match the diffusion time of the proposed method under restricted diffusion. Histograms of pixel-wise quantitative measurements covering the entire slice were plotted in two different slices. In order to measure T1, T2 and ADC, co-localized ROIs were drawn in the parietal right white matter within the corona radiata (WM, ~1cm^2), as well as in the parietal right gray matter (GM, 40mm^2) for statistical analysis[59]. ROIs were drawn in the same region for all volunteers, and the averaged measurements as well as standard deviation across volunteers were calculated.

Table 1. Phantom Imaging Protocol.

<table>
<tr><td>IR FSE
(Reference T1 mapping)
(15min24s)</td><td colspan="2">FOV = 28cm x 28cm, In-plane resolution = 1.1mm x 1.75 mm
Slice thickness = 6mm, Average = 1, Bandwidth = ±15.63kHz, TR=6s
TI = [50, 60, 70, 80, 90, 100, 110, 120, 130, 140, 150, 160, 170, 180] ms</td></tr>
<tr><td>Multi-TE SE
(Reference T2 mapping)
(18min18s)</td><td colspan="2">FOV = 28cm x 28cm, In-plane resolution = 2.2mm x 2.2 mm
Parallel imaging factor = 2, Slice thickness = 6mm,
Bandwidth = ±62.5kHz, TR=2s
TE = [20, 40, 60, 80, 100, 140, 160, 180, 200] ms</td></tr>
<tr><td>SE-DWI
(Reference ADC mapping)
(2min02s)</td><td colspan="2">FOV = 28cm x 28cm, In-plane resolution = 2.2mm x 2.2 mm
Parallel imaging factor = 2, Slice thickness = 6mm,
Bandwidth = ±62.5kHz, TR=2s,
Diffusion direction = three orthogonal diffusion directions (x,y, and z),
b = [20, 50, 100(2), 300(4), 500(6), 800(6)] s/mm2</td></tr>
<tr><td rowspan="4">STEM
(8min08s)</td><td>TM = 25ms, TE = 49.04ms</td><td rowspan="4">FOV = 28cm x 28cm,
In-plane resolution = 2.2mm x 2.2 mm
Parallel imaging factor = 2,
Slice thickness = 6mm,
Bandwidth = ±62.5kHz, TR=2s
Same diffusion directions and b-values as SE-DWI</td></tr>
<tr><td>TM = 100ms, TE = 39.84ms</td></tr>
<tr><td>TM = 100ms, TE = 100ms</td></tr>
<tr><td>TM = 200ms, TE = 36.34ms</td></tr>
</table>

Table 2. *In-vivo* Imaging Protocol.

(a) Brain Imaging

IR FSE (Reference T1 mapping) (8min48s)	FOV = 28cm x 28cm, In-plane resolution = 1.1mm x 1.75 mm Slice thickness = 5mm, Average = 1, Bandwidth = ±15.63kHz, TR=6s TI = [50, 200, 350, 425, 500, 750, 900, 1100] ms	
Multi-TE SE (Reference T2 mapping) (10min10s)	FOV = 28cm x 28cm, In-plane resolution = 2.2mm x 2.2 mm Parallel imaging factor = 2, Slice thickness = 5mm, Bandwidth = ±62.5kHz, TR=1.8s TE = [30, 60, 90, 120, 150] ms	
STE-DWI (Reference ADC mapping) (1min40s)	FOV = 28cm x 28cm, Resolution = 2.2mm x 2.2 mm, Parallel imaging factor = 2, Slice thickness = 5mm, Bandwidth = ±62.5kHz, TR=4s, Diffusion direction = R/L, TM=100ms, TE =40ms, b== [50, 100, 200(2), 400(4), 600(6), 800(8)] s/mm^2	
STEM (13min20s)	TM = 25ms, TE = 49ms	FOV = 28cm x 28cm, Resolution = 2.2mm x 2.2 mm Parallel imaging factor = 2, Slice thickness = 5mm, Bandwidth = ±62.5kHz, TR=4s Diffusion direction = R/L, Same b-values as STE-DWI
	TM = 100ms, TE = 40ms	
	TM = 100ms, TE = 50ms	
	TM = 100ms, TE = 80ms	
	TM = 500ms, TE = 40ms	
	TM = 500ms, TE = 50ms	
	TM = 500ms, TE = 80ms	
	TM = 1000ms, TE = 40ms	

(b) Prostate Imaging

DESPOT1 with B1 correction (Reference T1 mapping) (4min36s)	FOV = 28cmx28x14cm, In-plane resolution = 0.8mm x 0.57 mm Slice thickness = 5mm, Average = 4, Bandwidth = ±62.5kHz, TR=4s Flip angle = [10°, 5°, 1.8°]	
Multi-TE SE (Reference T2 mapping) (8min08s)	FOV = 26cm x 32cm, In-plane resolution = 2.5mm x 2.5 mm Parallel imaging factor = 2, Slice thickness = 5mm, Bandwidth = ±62.5kHz, TR=1.8s TE = [20, 60, 80, 120] ms	
STE-DWI (Reference ADC mapping) (2min52s)	FOV = 32cm x 32cm, Resolution = 2.5mm x 2.5 mm, Parallel imaging factor = 2, Slice thickness = 5mm, Bandwidth = ±62.5kHz, TR=4s, Diffusion direction = R/L, TM=100ms, TE =40ms, b= [50, 100, 200(2), 400(4), 600(6), 800(8)] s/mm^2	
STEM (22min56s)	TM = 25ms, TE = 49ms	FOV = 32cm x 32cm, Resolution = 2.5mm x 2.5 mm Parallel imaging factor = 2, Slice thickness = 5mm, Bandwidth = ±62.5kHz, TR=4s Diffusion direction = R/L
	TM = 100ms, TE = 40ms	
	TM = 100ms, TE = 50ms	
	TM = 100ms, TE = 65ms	
	TM = 500ms, TE = 40ms	
	TM = 500ms, TE = 50ms	
	TM = 500ms, TE = 65ms	
	TM = 1000ms, TE = 40ms	

2.3.2 Prostate Imaging

After IRB approval and informed written consent, healthy volunteers (n=8) were scanned at the same 3T scanner with a 32-channel torso coil for prostate mapping. No antiperistaltic agents were used in this study. As shown in **Table 2**(b), the STEM acquisitions were performed with eight TE and TM combinations, each with six b-values and a single diffusion direction. Interleaved slices were acquired within a TR. Due to scan time limitations, DESPOT1[23] was performed as the reference T1 map. Also, similar to brain imaging, a single STE-DWI acquisition (TE=40ms, TM=100ms was used as reference because of restricted diffusion in the prostate. Histograms of pixel-wise quantitative T1, T2, and ADC measurements within the prostate were evaluated from a single slice covering the mid-gland of the prostate. Co-localized ROIs were drawn in the peripheral zone (PZ, 40mm^2) and central gland (CG, 40mm^2) for further quantitative evaluation of T1, T2, and ADC. ROIs were drawn in the same region for all volunteers, and the averaged measurements as well as standard deviation across volunteers were calculated.

2.3.3 Protocol Optimization for Rapid STEM Acquisitions

In the validation experiments described above, relatively dense sampling of the TM-TE-b space was used to validate the feasibility of STEM. However, this dense sampling results in time-consuming acquisitions. Ideally, in order to estimate T1, T2 and ADC from the signal model in Eq.1, it suffices to acquire two different TM, TE and b-values (ie: at least four total images are needed). The choice of TM, TE and b-values can be formulated as an optimization problem. In this work, this protocol optimization problem was formulated as a minimax problem of the

Cramér-Rao Lower Bound (CRLB)-based standard deviation of the resulting T1, T2 and ADC estimates. The optimization problem was formulated as follows:

$$\widehat{\boldsymbol{\theta}} = \underset{\boldsymbol{\theta}\in\boldsymbol{\Theta}}{\mathbf{argmin}}\ \mathbf{max}\{\boldsymbol{\sigma}^{\mathbf{2}}|_{(\boldsymbol{T1},\boldsymbol{T2},\boldsymbol{ADC})\boldsymbol{\epsilon}\boldsymbol{\Omega}}\} = \underset{\boldsymbol{\theta}\in\boldsymbol{\Theta}}{\mathbf{argmin}}\ \mathbf{max}\left\{\left(\frac{\boldsymbol{\sigma_{T1}}}{\boldsymbol{T1}}\right)^{\mathbf{2}} + \left(\frac{\boldsymbol{\sigma_{T2}}}{\boldsymbol{T2}}\right)^{\mathbf{2}} + \left(\frac{\boldsymbol{\sigma_{ADC}}}{\boldsymbol{ADC}}\right)^{\mathbf{2}}|_{(\boldsymbol{T1},\boldsymbol{T2},\boldsymbol{ADC})\boldsymbol{\epsilon}\boldsymbol{\Omega}}\right\} \tag{6}$$

In this optimization problem, $\boldsymbol{\Omega}$ is the given T1-T2-ADC space that defines the range of tissue parameters under consideration, and $\boldsymbol{\Theta}$ is the constraint space determined by the scanner and pulse sequence properties. Additionally, $\widehat{\boldsymbol{\theta}}$ is a vector containing the optimized protocol parameters, which in this work are defined as TE_1, TE_2, TM_1, TM_2 and two b-values b_1 and b_2. These acquisition parameters determine the four acquired images with [TE_1, TM_1, b_1], [TE_2, TM_1, b_1] and [TE_1, TM_2, b_1] and [TE_1, TM_1, b_2], respectively. Further, $\boldsymbol{\sigma_{T1}}$, $\boldsymbol{\sigma_{T2}}$ and $\boldsymbol{\sigma_{ADC}}$ are the standard deviation from CRLB analysis of the magnitude signal with a given SNR (Rician noise)[60]. The sum of squares of the relative standard deviations is chosen as the cost function to ensure a balanced consideration of the noise performance of T1, T2 and ADC estimation.

The constraint space $\boldsymbol{\Theta}$ includes constraints on the sequence timing and the achievable b-values. First, the two echo times should have a lower bound defined by the RF pulse durations $\boldsymbol{T_{90}^1}$ and $\boldsymbol{T_{90}^2}$ and EPI readout train length $\boldsymbol{T_{EPI}}$:

$$\boldsymbol{TE} \geq \mathbf{max}\left\{\frac{\boldsymbol{T_{90}^1}+\boldsymbol{T_{90}^2}}{\mathbf{2}}, \frac{\boldsymbol{T_{90}^2}}{\mathbf{2}} + \boldsymbol{T_{EPI}}\right\}. \tag{7}$$

Similarly, the two mixing times should be longer than the second and the third 90° pulse:

$$\boldsymbol{TM} > \boldsymbol{T_{90}^2}. \tag{8}$$

Second, the maximum achievable b-value with the given TE and TM should be larger than both $\boldsymbol{b_1}$ and $\boldsymbol{b_2}$, as follows:

$$\boldsymbol{b} \leq (\boldsymbol{\gamma G_{max}\delta})^{\mathbf{2}}\left(\boldsymbol{\Delta} - \frac{\boldsymbol{\delta}}{\mathbf{3}}\right), \tag{9}$$

where $\boldsymbol{\gamma}$ is the gyromagnetic ratio and $\boldsymbol{G_{max}}$ is the maximum gradient strength of the scanner. $\boldsymbol{\Delta}$ is the diffusion time and $\boldsymbol{\delta}$ is the duration of diffusion encoding lobe, assuming infinite slew rate to simplify the description. With minimized TE, $\boldsymbol{\Delta}$ and $\boldsymbol{\delta}$ can be expressed in terms of the remaining pulse sequence timing parameters including TE, TM and RF pulse durations:

$$\boldsymbol{\delta} = \mathbf{min}\left\{\frac{\boldsymbol{TE}-\boldsymbol{T_{90}^2}}{\mathbf{2}} - \boldsymbol{T_{EPI}}, \frac{\boldsymbol{TE}-\boldsymbol{T_{90}^1}-\boldsymbol{T_{90}^2}}{\mathbf{2}}\right\} \quad (10)$$

$$\Delta = \boldsymbol{\delta} + \boldsymbol{T_{90}^2} + \boldsymbol{TM}. \quad (11)$$

In this study, sequence parameter constraints included $\boldsymbol{G_{max}} = \mathbf{50}\ \boldsymbol{mT/m}$, $\boldsymbol{T_{90}^1} = \mathbf{12}\boldsymbol{ms}$ for water selective excitation pulse, $\boldsymbol{T_{90}^2} = \mathbf{6.5}\boldsymbol{ms}$ and $\boldsymbol{T_{EPI}} = \mathbf{10}\boldsymbol{ms}$. SNR in the simulation, which was equal to the proton density weighted signal **A** divided by the standard deviation, was set as 50. Optimization was run with different T1-T2-ADC space $\boldsymbol{\Omega}$ for healthy brain and healthy prostate tissues respectively, where $\boldsymbol{T1} \in (\mathbf{700}, \mathbf{1350})\boldsymbol{ms}$, $\boldsymbol{T2} \in (\mathbf{50}, \mathbf{150})\boldsymbol{ms}$ and $\boldsymbol{ADC} \in (\mathbf{550}, \mathbf{1400}) \times \mathbf{10^{-6}}\boldsymbol{mm^2/s}$ for brain and $\boldsymbol{T1} \in (\mathbf{600}, \mathbf{1500})\boldsymbol{ms}$, $\boldsymbol{T2} \in (\mathbf{50}, \mathbf{100})\boldsymbol{ms}$ and $\boldsymbol{ADC} \in (\mathbf{800}, \mathbf{1500}) \times \mathbf{10^{-6}}\boldsymbol{mm^2/s}$ for prostate.

With this optimization scenario, the optimal combinations of TE, TM and b-values will be obtained. In this study, optimized rapid acquisitions were selected retrospectively by choosing the optimal combination of TE_1, TE_2, TM_1, TM_2, b_1, b_2 from the densely-sampled acquisitions described above for brain and prostate. Data from the resulting rapid acquisitions were re-fitted to the signal model (**Equation 4**), to obtain T1, T2, and ADC parametric maps. These parametric maps were compared between the rapid acquisition and the densely-sampled acquisition, in order to preliminarily evaluate the feasibility of the rapid STEM acquisition.

2.3.4 Evaluation of B1 Inhomogeneity Effects

T1 mapping methods are often confounded by B1 inhomogeneity effects. To evaluate the effect of imperfect B1 fields on the quantitative STEM measurements, several STEM acquisitions with different actual flip angles were obtained by adjusting the scanner transmit gain. With this setup, the actual STE sequence performed included three $\alpha°$ pulses instead of the idealized three 90° pulses. A NiCl2-doped water phantom was scanned at 3T using an eight-channel head coil with default transmit gain. To adjust the actual flip angle, two additional acquisitions were obtained with transmit gains equal to 45% and 135% of the original transmit gain, respectively. STEM was implemented with TM = [25, 100, 100]ms, TE = [50, 42, 80]ms and b-values(#average) = [0(2),100(2),200(2),400(4),800(8)]s/mm^2. Other parameters included TR=3s, slice thickness = 5mm, FOV = 26cm, in-plane resolution = 2mm × 2mm and diffusion direction = R/L. Bloch-Siegert B1 maps[61] were acquired to measure the actual flip angle in different regions within the acquired slice. Two ROIs (~1cm2) were drawn from each actual flip angle map of the images acquired with different transmit gains (6 ROIs in total).

The corresponding STEM-based T1, T2 and ADC measurements co-localized with the previously described ROIs were used to analyze the relationship between the quantitative measurements and actual flip angle. Linear regression between each quantitative measurement and the actual flip angles was performed to evaluate the effects of B1 inhomogeneity on STEM measurements.

2.3.5 Dependence of T1, T2, and ADC Quantification on Acquisition Parameters

The proposed STEM acquisition, which samples the MR parameter space along multiple relaxometry and diffusion dimensions, may enable more sophisticated multi-parametric tissue characterization beyond the simplified signal model described in **Equation 4**. For instance, **Equation 4** jointly fits all the data without accounting for the potential dependence of T1/T2/ADC on the acquisition parameters. However, this dependence might occur in tissue, e.g.: due to the presence of partial volume effects or non-Gaussian diffusion. Therefore, the measured T1 or T2 may vary with increasing b-value, and the measured ADC may vary with increasing TE or TM (even for a constant set of b-values). To evaluate this dependence in both brain and prostate data, separate estimation of each quantitative parameter was performed within four groups of acquisition parameters:

1) Fixed TE = 40ms, for each b-value, calculate T1 maps with TM = [100, 500, 800, 1000]ms (to evaluate the effect of b-value on measured T1);

2) Fixed TM=100ms, for each b-value, calculate T2 maps with TE = [40, 50, 80]ms for the brain and TE = [40, 50, 65]ms for the prostate (to evaluate the effect of b-value on measured T2);

3) Fixed TE = 40ms, for each TM, calculate ADC maps with all six b-values (to evaluate the effect of TM on measured ADC);

4) Fixed TM = 100ms, for each TE, calculate ADC maps with all six b-values (to evaluate the effect of TE on measured ADC).

ROI measurements from the same regions described above for brain and prostate scans were performed in the corresponding maps from each group of parameters, and displayed using box-plots. A Linear Mixed-Effect (LME) fitting model[62] was applied to evaluate the association between measurements and acquisition parameters.

2.3.6 Patient Evaluation

After IRB approval and informed written consent, 16 patients with suspected PCa and/or Benign Prostatic Hyperplasia (BPH) were recruited to evaluate the T1, T2 and ADC values from STEM acquisitions. STEM acquisitions were performed with in-plane resolution = 2mm×2mm, slice thickness = 4.8mm, acquisition bandwidth = ±62.5kHz, TR=4s, Diffusion direction = three orthogonal directions and parallel imaging factor = 2 with partial Fourier acquisition. Based on the protocol optimization and scanner limitations, rapid STEM acquisition parameters described above were used in patient scans. ROIs were drawn in the healthy PZ, healthy CG, PCa and BPH respectively for each patient. Two-sample t-test was applied without assuming equal variance to evaluate the difference of measurements between lesion and healthy tissue.

2.4 Results

2.4.1 Phantom Validation

Figure 2 shows T1, T2, and ADC mapping results in the phantom. STEM results in quantitative maps with high image quality and good SNR, although EPI related distortion artifacts

remain. Further, these results show excellent quantitative agreement between STEM and the reference T1, T2, and ADC mapping techniques. The R^2 for T1, T2 and ADC are all nearly 0.999. The slope for each parameter is 1.01±0.01, 1.03±0.01 and 0.97±0.01, respectively. The intercept for each parameter is 1.94±2.31ms, -2.51±1.5ms and 0.04±0.01× 10^{-3}mm^2/s respectively.

2.4.2 Brain and Prostate Imaging in Healthy Volunteers

Representative quantitative maps for two different slices in the brain of a healthy volunteer, with histograms from each entire slice are presented in **Figure 3**. Orange bars in the histograms are from the reference maps, blue bars are from the STEM maps and red-colored areas are the overlap between the proposed and reference methods. The high overlap between STEM and reference measurement histograms illustrates the accuracy of the proposed STEM method. Nevertheless, the STE-DWI sequence used in STEM has limited spatial resolution compared to the reference IR-FSE T1 mapping and SE T2 mapping.

Figure 4 shows representative maps and histograms of the prostate. Although high overall agreement is observed between STEM and the reference mapping methods, some estimation bias and image artifacts may be present in STEM, especially near the edges of the prostate.

Table 3 summarizes the T1, T2, and ADC measurements in the brain and prostate across all subjects. Overall, STEM measurements are in excellent agreement with reference measurements, with similar standard deviation across subjects.

2.4.3 Protocol Optimization for Rapid STEM Acquisition

In the protocol optimization simulations, the optimized acquisition parameters for rapid STEM imaging are TE_1=39.4ms, TE_2=92.2ms, TM_1=123.1ms, TM_2=1026.2ms and b_1=0 s/mm^2 and b_2=826.5 s/mm^2 in the brain and TE_1=39.6ms, TE_2=95.0ms, TM_1=124.2ms, TM_2=1244.5ms and b_1=0 s/mm^2 and b_2=863.9 s/mm^2 in the prostate. Among the parameters acquired in the previously obtained densely-sampled *in-vivo* datasets, the optimal combinations are TE_1=40ms, TE_2=80ms, TM_1=100ms, TM_2=1000ms and b_1=50s/mm^2 and b_2=800s/mm^2 in the brain and TE_1=40ms, TE_2=65ms, TM_1=100ms, TM_2=1000ms and b_1=50s/mm^2 and b_2=800s/mm^2 in the prostate. The optimized rapid STEM acquisitions are less than 2 minutes for both brain and prostate imaging.

Figure 5 shows an example plot of the cost function σ^2 (ie: the sum-of-squares of relative standard deviation for T1-T2-ADC estimation, as a function of the acquisition parameters) used for optimization of rapid acquisition protocols. **Figure 6** shows the T1, T2 and ADC maps estimated from the resulting optimized rapid protocol (Figure 6a: brain, Figure 6b: prostate). Quantitative maps from the rapid STEM acquisition are noisier than the original densely-sampled maps; however, the measurements remain accurate. ROI measurements from the rapid STEM acquisitions in brain and prostate are also summarized in **Table 3**.

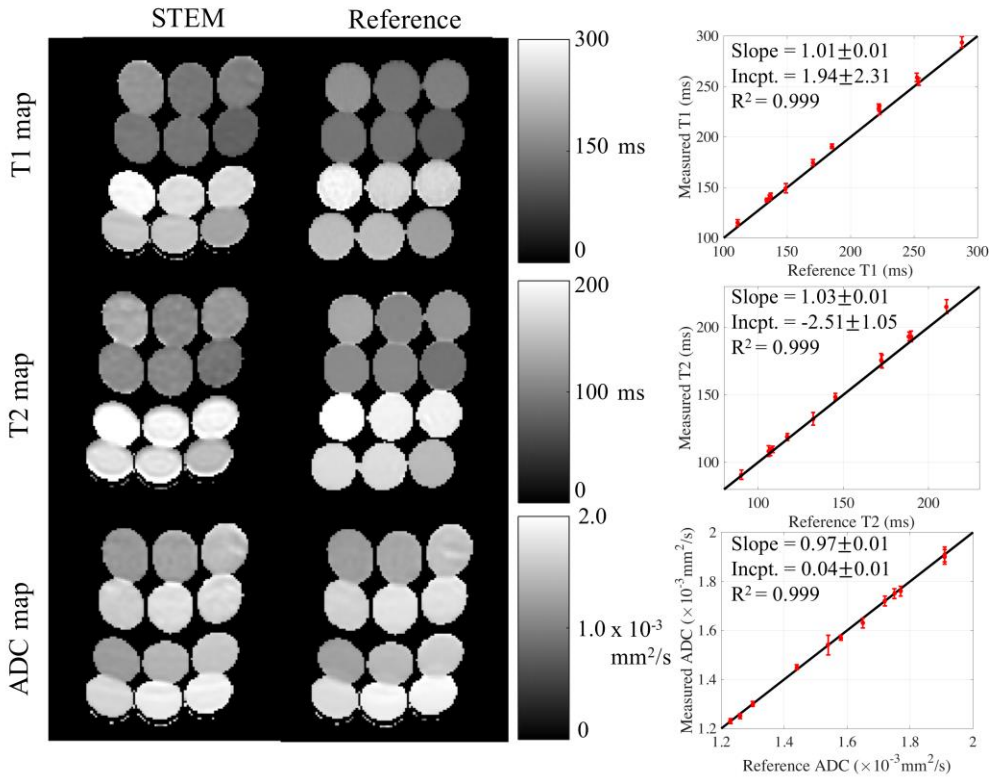

Figure 2. Comparison of estimated T1, T2 and ADC maps in diffusion phantom. T1, T2 and ADC maps estimated from STEM are accurate compared to the reference maps. The vials in the parametric maps have EPI distortion artifacts in the STEM images and the reference spin echo ADC map because of the EPI acquisitions. ROI measurements for each vial from STEM agree with the co-localized ROI results from the reference maps. The black lines in the plots to the right are the identity lines representing equal measurements and references.

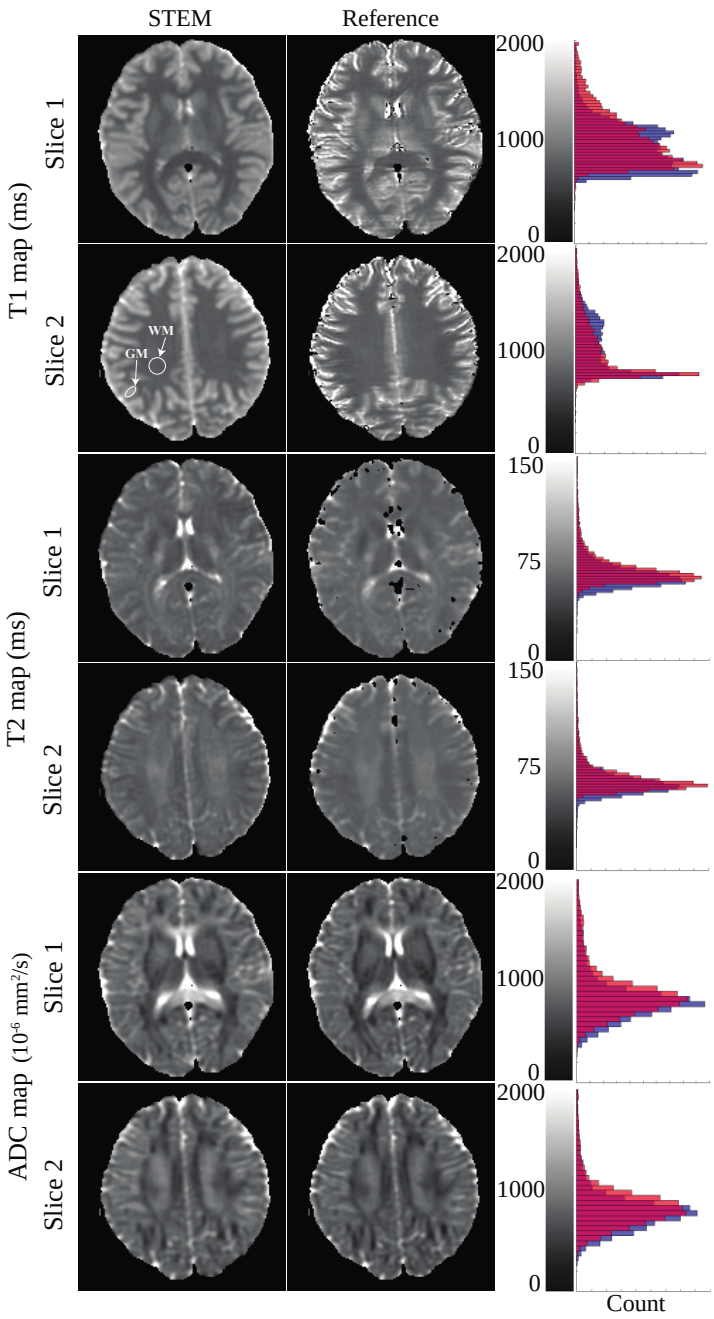

Figure 3. Example estimated T1, T2 and ADC maps in the brain. The distributions of T1, T2 and ADC measurements in the brain from STEM are in good qualitative agreement with the reference measurements. The histograms to the right show the overall accuracy of each measurement from the entire slice. Orange bars in the histograms are from the reference maps, blue bars are measurements from STEM and the red color represents the overlapping area of reference and STEM-based histograms. The white arrows point to the ROIs in the white matter and gray matter.

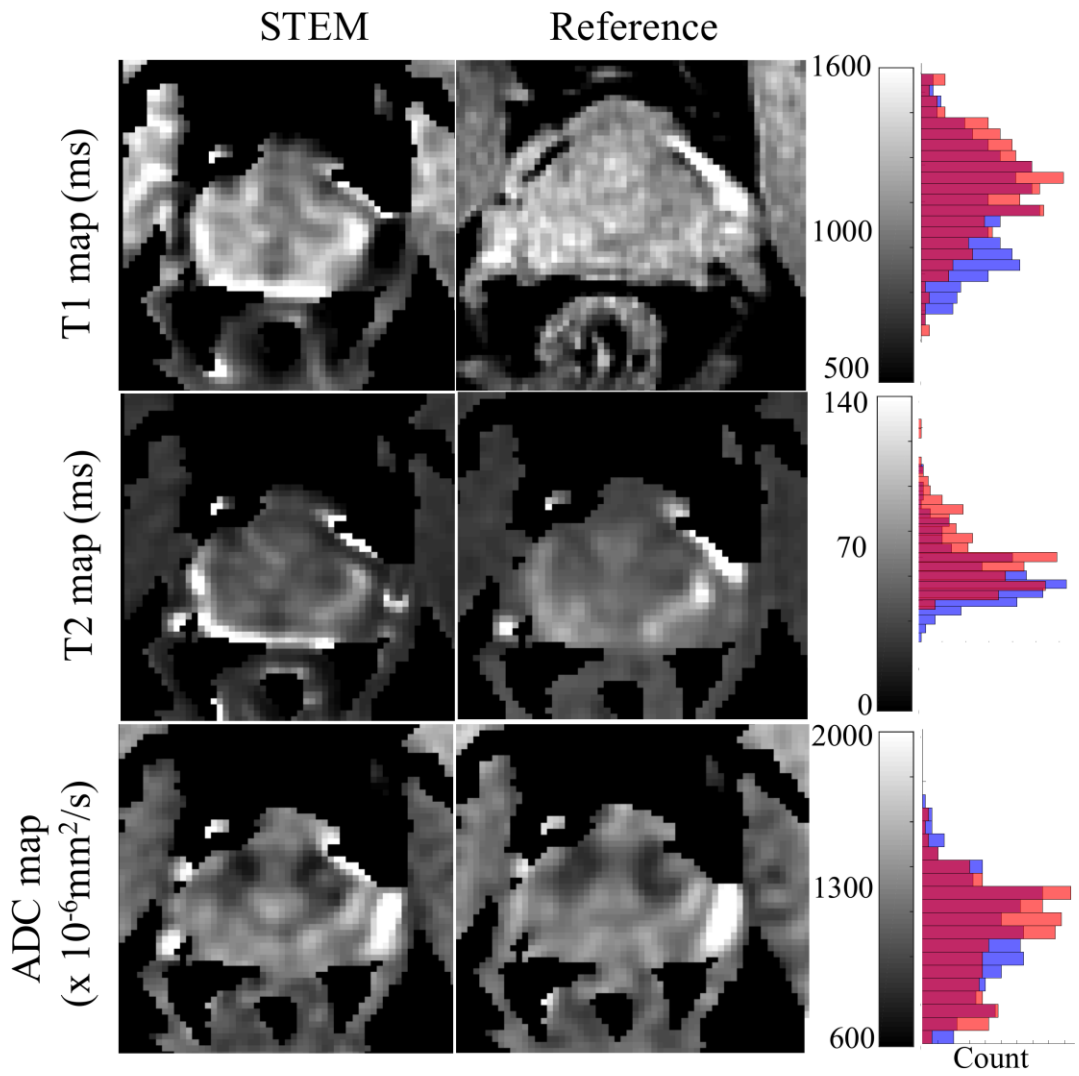

Figure 4. Example estimated T1, T2, and ADC maps in the prostate.
The distributions of T1, T2 and ADC measurements in the prostate from STEM agree with the references, though with some bias in the T1 and T2 maps. Artifacts appearing at the edge of the prostate are mainly from the inter-acquisition motion from series to series. The histograms to the right show the overall accuracy of each measurement covering only the prostate area. Orange bars in the histograms are from the reference maps, blue bars are measurements from STEM and the red color represents the overlapping area of orange and blue bars.

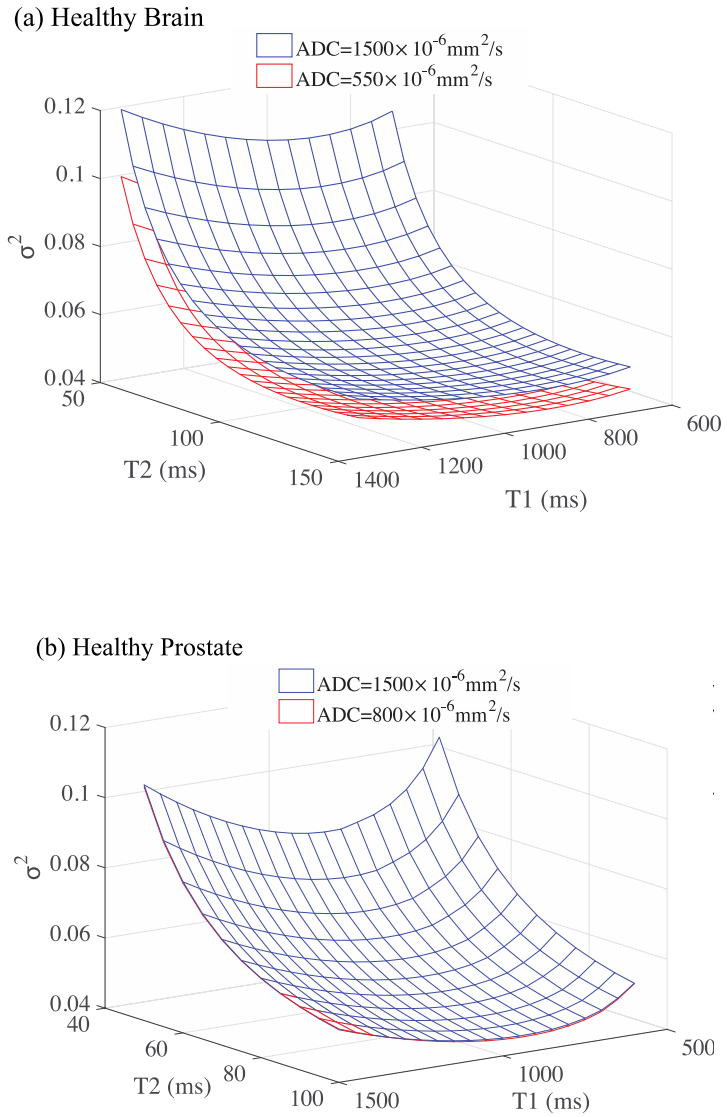

Figure 5. Example plot of the cost function in rapid STEM optimization.
An example plot of the cost function σ^2 (ie: the sum-of-squares of relative standard deviation for T1-T2-ADC estimation, as a function of the acquisition parameters) used for optimization of rapid acquisition protocols is shown to the left for both healthy brain (a) and prostate (b).

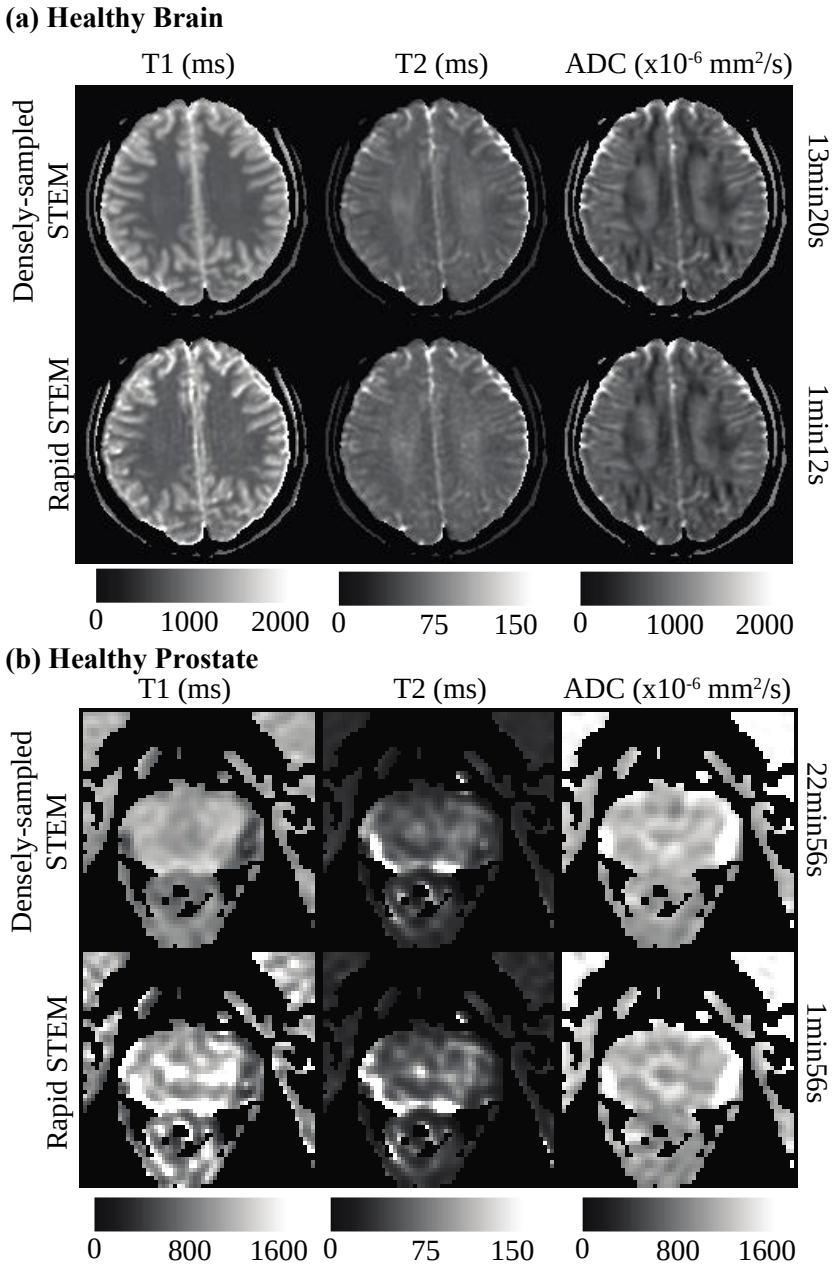

Figure 6. Example re-estimated *in-vivo* T1, T2 and ADC maps with rapid STEM acquisitions. An example of T1, T2 and ADC maps re-estimated retrospectively with the optimized rapid acquisition protocol (rapid STEM) are shown for healthy brain (a) and healthy prostate (b). The overall measurements are accurate even though the maps are noisier. The T1 map of healthy prostate shows some artifacts, likely due to motion without antiperistatic agents.

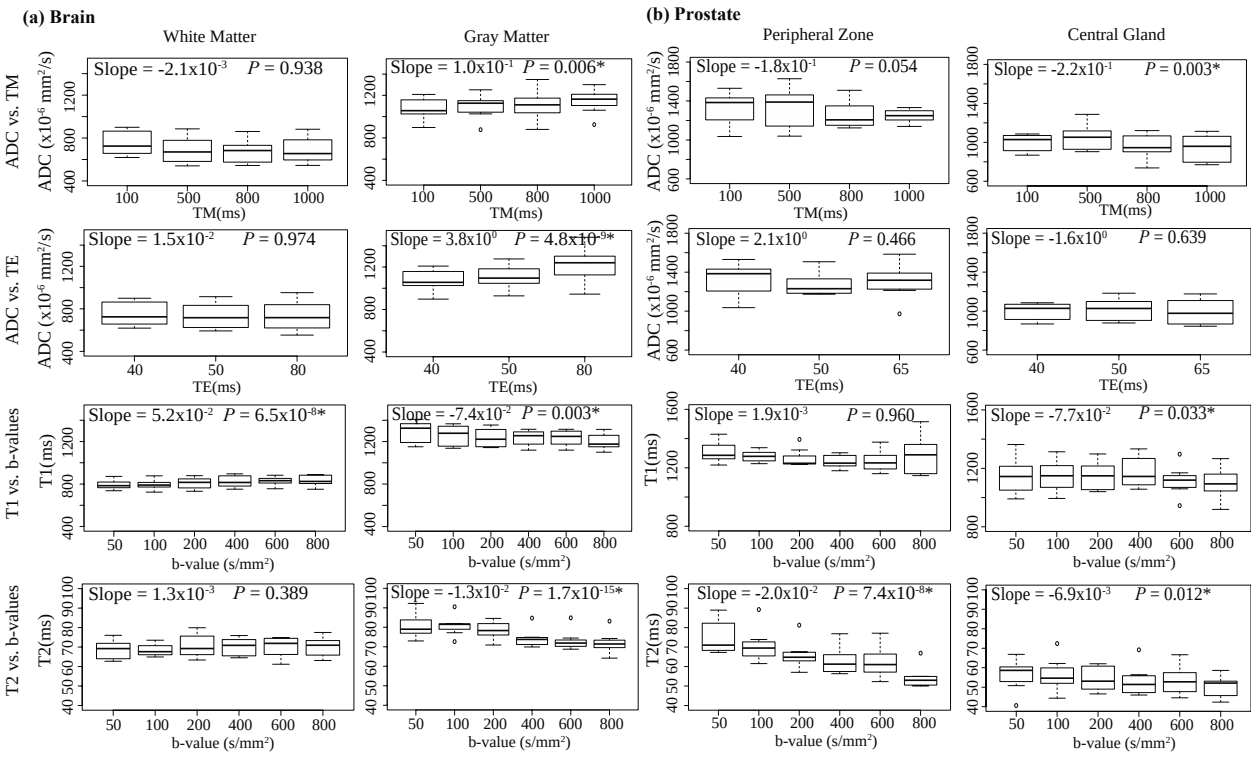

Figure 7. Dependence of T1, T2 and ADC Quantification on Acquisition Parameters. Box-plots from ROIs measurements in the maps of each controlled group are shown for brain and prostate tissues, respectively. The linear mixed effect analysis results, including the slope and P-values, are labeled in each Box-plot.

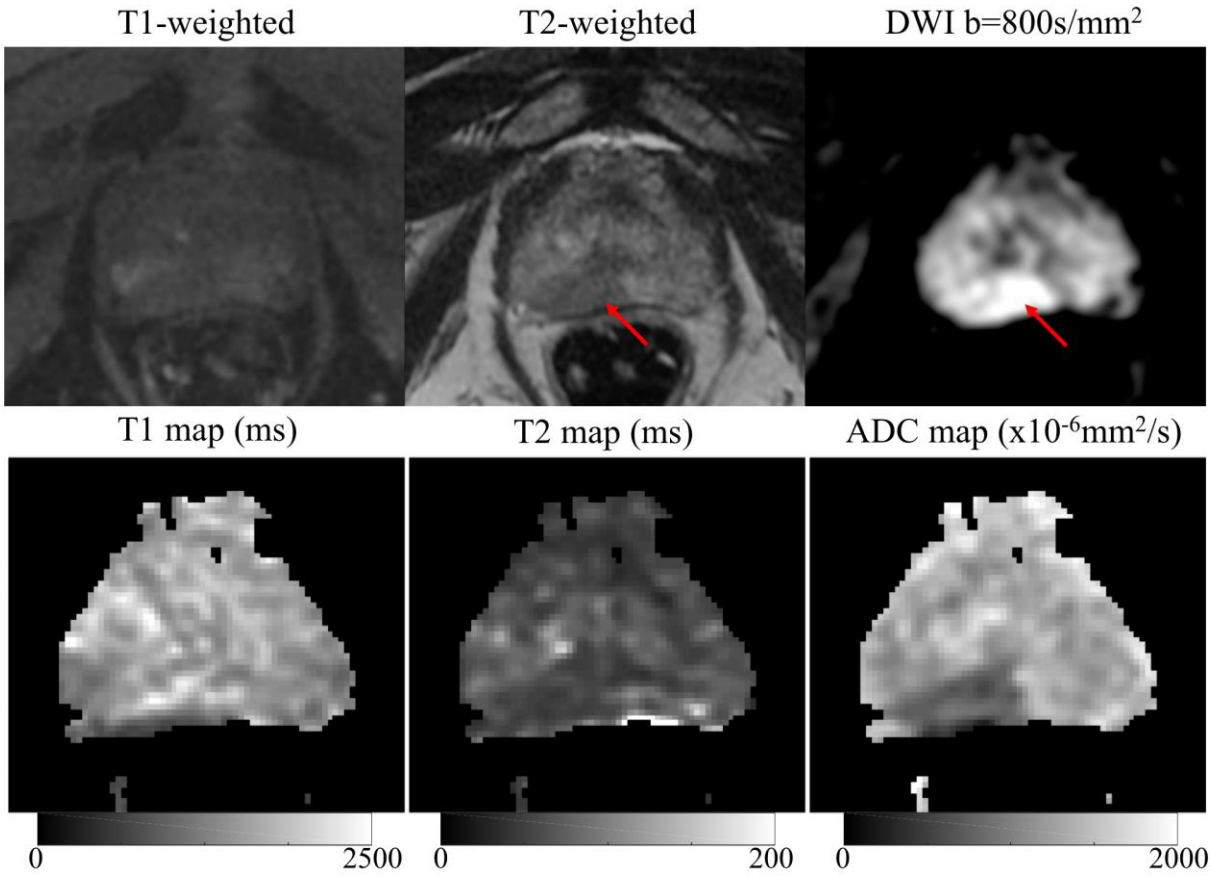

Figure 8. Patient example of rapid STEM acquisition in a 69-year-old patient.
The patient has a PI-RADS 5 cancer lesion in the right PZ (pointed by the red arrows). The estimated T1, T2 and ADC maps are shown in the bottom row.

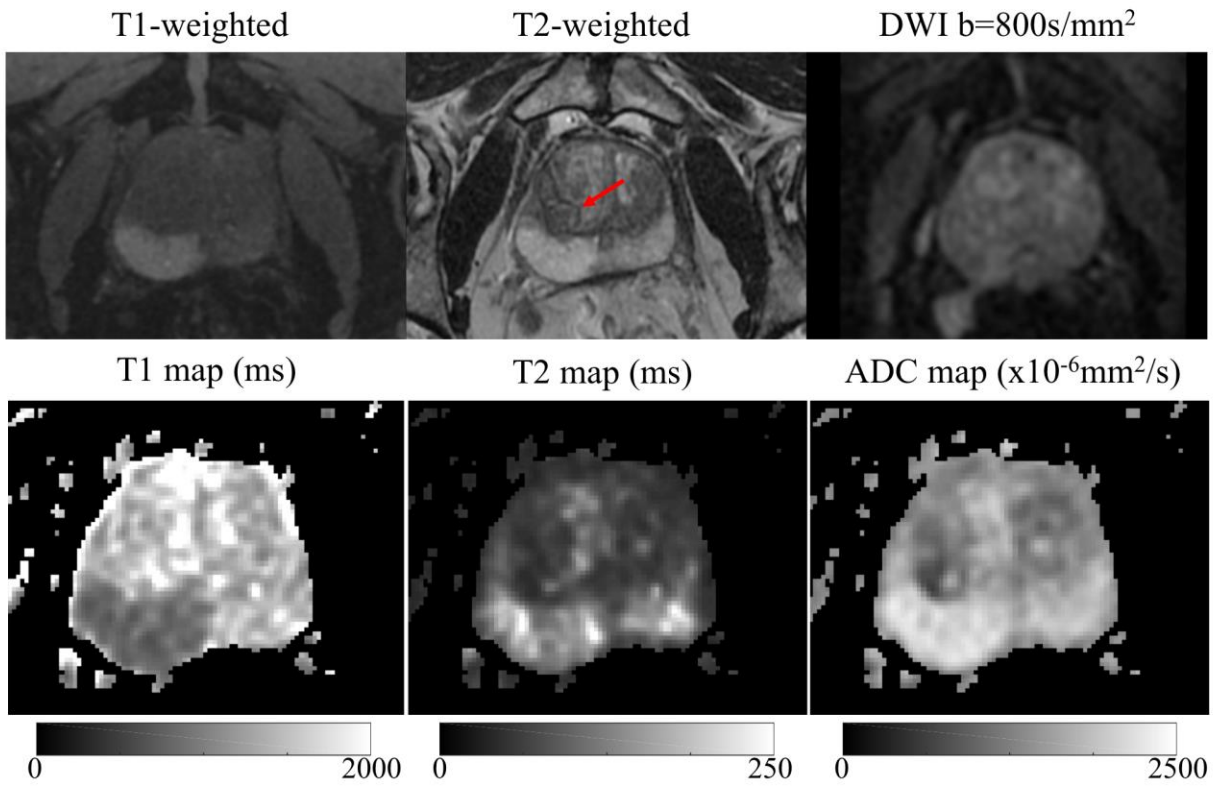

Figure 9. Patient example of rapid STEM acquisition in a 60-year-old patient with BPH. The patient has a BPH nodule in the right CG (pointed by the red arrows). The estimated T1, T2 and ADC maps are shown in the bottom row, which match the T1w, T2w and diffusion-weighted images. The lower T1 in the right PZ is likely due to the post-biopsy hemorrhage.

Table 3. *In-vivo* ROI Measurements in Healthy Volunteers.

Brain	White matter			Gray matter		
	STEM	Rapid STEM	Reference	STEM	Rapid STEM	Reference
T1 (ms)	780.8 ±47.5	805.8±52.1	788.5±49.3	1241.4±119.1	1253.3±106.6	1219.9±92.3
T2 (ms)	65.6±4.2	67.5±4.9	67.1±4.0	71.4±6.4	77.5±8.1	76.9±6.2
ADC ($\times 10^{-6}$ mm^2/s)	690.7 ±125.4	708.0±120.9	710.0±126.9	928.6 ± 103.8	918.5±81.2	918.8±86.4
Prostate	Peripheral zone (PZ)			Central gland (CG)		
	STEM	Rapid STEM	Reference	STEM	Rapid STEM	Reference
T1 (ms)	1344.1±63.5	1420.4±217.2	1349.8±149.2	1156.7±65.6	1216.6±113.5	1244.5±104.3
T2 (ms)	65.1±6.3	68.1±10.3	70.6 ± 5.5	53.2±6.7	58.1±13.2	57.4±4.6
ADC ($\times 10^{-6}$ mm^2/s)	1200.7±102.4	1151.5±141.4	1140.9 ±132.2	1038.0±88.8	1040.2±136.4	1038.1±97.2

2.4.4 Evaluation of B1 Imperfection

The measured flip angles over the six ROIs in the three acquisitions were 49.1°, 62.9°, 100.8°, 132.4°, 138.4° and 157.6°, respectively. Based on linear regression analysis, the coefficients (slopes) between T1 and flip angle, T2 and flip angle and ADC and flip angle are -1.23×10^{-2} (P=0.210), 3.90×10^{-3}(P=0.645) and 1.36×10^{-1}(P=0.181), respectively. With a 95% confidence level, quantitative T1, T2 and ADC measurements from STEM acquisitions are not affected by imperfect flip angle.

2.4.5 Dependence of T1, T2 and ADC Quantification on Acquisition Parameters

Box-plots from ROI measurements in the quantitative measurements for varying acquisition parameters are shown in **Figure 7**. The LME analysis results, including the slope and *P*-values, are shown in each box-plot. Though the number of volunteers is limited, some measurements are significantly dependent on acquisition parameters. For example, the measured T2 values show a significant decrease with increasing b-values for gray matter as well as for the prostate PZ and CG ($P<0.001$).

2.4.6 Patient Evaluation

Among 16 patients, seven patients of them have PCa in the peripheral zone (PZ), two of them have PCa in the central gland (CG) and nine of them have BPH. Example T1, T2 and ADC maps of two volunteers are shown in **Figure 8** and **Figure 9**. Average and standard deviation of ROI measurements are shown in **Figure 10** to compare the difference in T1, T2 and ADC values among healthy tissue, cancer and BPH. Both T2 and ADC values are lower in the PZ cancer compared to healthy PZ ($p<0.01$). The difference in T1 values between PZ cancer and healthy PZ is not significant ($p=0.22$) and varies among volunteers. In central gland, BPH and CG cancer have lower T2 and ADC measurements compared to healthy tissue.

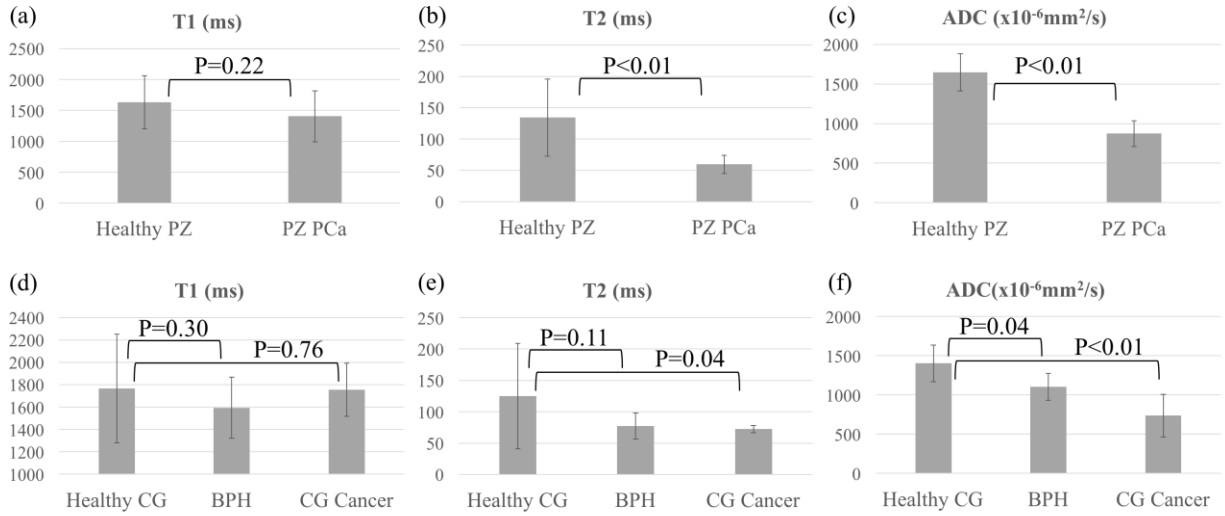

Figure 10. Comparison of ROI measurements from STEM in prostate patients. Comparison of ROI measurements from STEM. (a) to (c) compare the ROI measurements of T1, T2 and ADC respectively between healthy PZ and PCa. (d) to (f) compare the measurements of T1, T2 and ADC values of healthy CG, CG cancer and BPH.

2.5 Discussion

In this study, a Stimulated-Echo based Mapping (STEM) method has been proposed for simultaneous quantitative T1, T2 and ADC mapping. The overall T1, T2 and ADC measurements have been shown to be accurate in phantom experiments, brain and prostate imaging. Further, protocol optimization was performed to achieve accurate STEM quantification within 2 minutes. The proposed STEM method may enable rapid and co-registered multi-parametric imaging, with potential clinical applications in the brain, prostate, and breast, among others[14-14].

In brain mapping, the estimated T1 and T2 with densely-sampled STEM and rapid STEM acquisitions are in good agreement with measurements from previous studies[22–26,59]. The T1 histograms from STEM showed two peaks, representing white matter and gray matter respectively. This is in good agreement with previous T1 mapping studies performed with moderate spatial resolution[21]. However, the two peaks are not obvious in the reference T1 map. This may be due to the higher resolution in the reference T1 map, where the different T1 values from CSF and gray matter result in higher spread of T1. Further, measurements from CSF are not shown in this study because the measurements from our reference T1 and T2 mapping method failed in some volunteers likely due to the flow of CSF. However, STEM may suffer the same motion problem in the CSF. Also, the acquisitions in this study are not optimized for very high T1 and T2 measurements. The ADC values measured in this brain fall into the range of literature[24,59,63]; however, with only one diffusion direction measured in this study, ADC measurements in the white matter (where diffusion is highly anisotropic) are not comparable to the literature.

In healthy prostate mapping, the overall measurements are in generally good agreement with the literature[64–66]. However, the ADC values are slightly lower compared to previous spin echo-based ADC measurements in healthy prostate tissues[65–67]. This discrepancy may be due to

the restricted diffusion in the prostate[55], which makes ADC measurements dependent on specific acquisition parameters (eg: diffusion time). Also, previous measurements of T1, T2 and ADC have a broad variation across studies, and prostate ADC has been shown to increase with age[67]. In the prostate cancer case study, we observed a substantial decrease in the T2 and ADC values within the two lesions relative to healthy peripheral zone tissue, in agreement with the literature[17].

In this study, a simple signal model is used for jointly estimating T1, T2 and ADC values. However, in the presence of restricted diffusion, ADC will generally depend on the acquisition parameters, including choice of b-values and diffusion time. Therefore, more sophisticated diffusion models may be preferable. Also, partial volume effects may arise when multiple tissue components, epithelial and stromal components in the prostate for example, are contained in a voxel. These tissue components generally have different T1, T2 and diffusion properties, which may explain in part the slight underestimation in the *in-vivo* T2 measurements of both brain and prostate compared to the reference SE T2 mapping. These confounding factors, which present a challenge for naïve signal modeling approaches, may also present an opportunity for advanced multi-compartment tissue characterization[68,69] by exploiting the multiple signal dimensions (T1, T2, diffusion) probed by the STEM approach.

In this work, STEM scan times ranged from 1min13s with rapid acquisition to 22min56s with dense sampling of the TM-TE-b space. The acquisition time depends on multiple parameters, including the number of b-values and diffusion directions, and the choice of TM and TE combinations. In principle, a minimum of four images with different TM, TE and b-values are required for STEM. With protocol optimization, the maximum acquired TM and TE should be of the same order as the tissue T1 and T2, respectively. When T1 is very long (over 1000ms, as is the case in the prostate), a long TM (eg: 800-1200ms) would be needed to create enough T1 decay.

However, this will result in longer acquisitions with substantial 'dead time' during the mixing time. Future work may explore the possibility of increasing the duty cycle by exciting other slices or bands during the mixing time.

Although the proposed STEM approach is promising for accurate quantitative mapping, the current method has several limitations. STEM acquisitions are based on an EPI readout; therefore, they have the same geometric distortions as SE-DWI sequences in areas of B0 field inhomogeneity. More advanced acquisition techniques like reduced field-of-view (rFOV)[48–50] and multi-shot EPI (msEPI)[51–53] may enable reduced distortion in STEM. Also, due to the stimulated echo acquisition, the SNR of STE-DW images is only half the SNR of SE-DW images. Similar to other quantitative techniques, STEM is sensitive to motion during the acquisition. Although each individually acquired STEM image is highly robust to motion due to the single-shot EPI readout, motion between images may introduce artifacts in quantitative maps, particularly near tissue interfaces. For example, in the prostate maps, motion-induced mis-registration introduces inaccuracy in T2 and T1 maps. Particularly when using rapid STEM acquisitions, the estimation will be sensitive to artifacts and noise in the images. In clinical prostate imaging applications, antiperistaltic agents may be used to reduce small bowel motility, which may significantly reduce the artifacts in prostate measurements. For other organs, registration-based approaches may mitigate motion-related artifacts.

In the *in-vivo* healthy volunteer mapping experiment, the rapid acquisitions were performed retrospectively (i.e.: with a long temporal footprint), leading to increased motion artifacts in prostate mapping. Further, STE-DWI instead of SE-DWI was used as a reference for ADC in this study because ADC will be different for different diffusion time in the presence of

non-Gaussian diffusion. Extensions of this work may include more sophisticated models beyond simple ADC, in order to account for the presence of restricted diffusion.

Finally, the number of patients in this ongoing study is still small. Evaluation on a larger number of patients is needed to fully characterize the STEM-measured T1, T2 and ADC in PCa and BPH.

2.6 Conclusion

We have presented a stimulated-echo based approach termed STEM for simultaneous multi-parametric relaxometry and diffusion mapping. This method provides accurate quantitative maps of T1, T2, and ADC in phantom, brain, and prostate imaging. Further, the proposed approach may enable advanced multi-compartment tissue characterization in multiple parametric dimensions.

Chapter

3. Stimulated-Echo Diffusion Weighted Imaging with Moderate b-values for the Detection of Prostate Cancer[2]

3.1 Purpose

Conventional spin-echo (SE) DWI leads to a fundamental trade-off depending on the b-value: high b-value provides better lesion Contrast-to-Noise Ratio (CNR) by sacrificing Signal-to-Noise Ratio (SNR), image quality and quantitative reliability. Compared to standard SE DWI acquisitions, STE DWI[28] is able to achieve the same b-value with shorter TE than SE DWI by slightly increasing the mixing time (TM). Consequently, STE DWI enables reduced T2 shine-through effect, potentially leading to high CNR between PCa and normal PZ, while maintaining higher SNR and reliable ADC mapping compared to high b-value SE DWI. For these reasons, STE DWI may be able to overcome the limitations of SE DWI for prostate imaging, combining the advantages of low b-value and high b-value SE DWI acquisitions. Thus, the purpose of this study

[2] This work has been published in: Zhang Y, Wells SA, Triche BL, Kelcz F, Hernando D. Stimulated-echo diffusion-weighted imaging with moderate b values for the detection of prostate cancer. *European Radiology*. 2020; 1-9

is to propose and evaluate a STE DWI acquisition strategy for high-CNR imaging of prostate cancer while also enabling reliable ADC mapping.

3.2 Methods

3.2.1 Simulation

Simulations were performed with a digital prostate image consisting of a normal peripheral zone (PZ), normal transition zone (TZ), peripheral zone cancer (PZCa) and transition zone cancer (TZCa). The T2 values[70,71] of each component were 134ms for normal PZ tissue, 125ms for normal TZ tissue, 60ms for PZCa and 71ms for TZCa. The ADC values of each component were 1.6×10^{-3} mm^2/s for normal PZ tissue, 1.4×10^{-3} mm^2/s for normal TZ tissue, 0.8×10^{-3} mm^2/s for PZCa and TZCa.

Both diffusion weighted SE and STE images were simulated in Matlab (2016b, MathWorks). The parameters used to simulate the diffusion acquisition for each b-value were G_{max}=50mT/m, $SlewRate_{max}$ = 150T/m/s, T_{90}=5ms, T_{180}=5ms and readout-to-echo time=11ms. TM was fixed at 100ms for STE DWI sequence design. Various maximum b-values were simulated with TE minimized for each b-value. Random Rician noise was added to the simulated images[72]. The SNR of the normal PZ tissue and CNR between PZCa and normal PZ tissue were calculated for each simulated DWI signal.

3.2.2 Patient Recruitments

In this prospective, cross-sectional, single-site study, patients (N=27, 61±13-year-old) with suspected PCa were recruited after IRB approval and informed written consent. Further, 24 out of 27 patients had targeted (N=16) and/or systematic (N=19) biopsy either after or two to four weeks before their multiparametric prostate MRI. Among all patients, 11 patients had biopsy-confirmed PZCa and 4 patients had biopsy-confirmed TZCa. Details of patient recruitment are shown in **Figure 11.**

3.2.3 Image Acquisition

Images were acquired on one of two clinical 3T MR scanners (GE MR750 and GE MR750w, GE Healthcare). High-resolution T2-weighted images were obtained with FOV = 26cm×26cm, in-plane resolution=1.02mm×0.85mm, slice thickness = 2.4mm, TE=108.6ms and TR=3s. For each patient, two SE DWI series with b = [100, 800] s/mm^2 and b = [100,1500] s/mm^2, respectively, were acquired as reference DWI sequences. One STE DWI series was performed with TM = 100 ms and b = [100, 800] s/mm^2. All DWI series were acquired with FOV = 12cm×24cm, in-plane resolution = 2.0mm×2.0mm, 16 slices with slice thickness = 4.8mm, three orthogonal diffusion directions, parallel imaging acceleration factor = 2, 75% partial Fourier acquisition and bandwidth = ±62.5kHz. Other detailed imaging parameters and acquisition times for both scanners are shown in **Table 4**. ADC maps were calculated pixelwise as follows

$$\mathrm{ADC} = -\frac{\ln(S_{b_2}) - \ln(S_{b_1})}{\mathrm{b}_2 - \mathrm{b}_1} \tag{12}$$

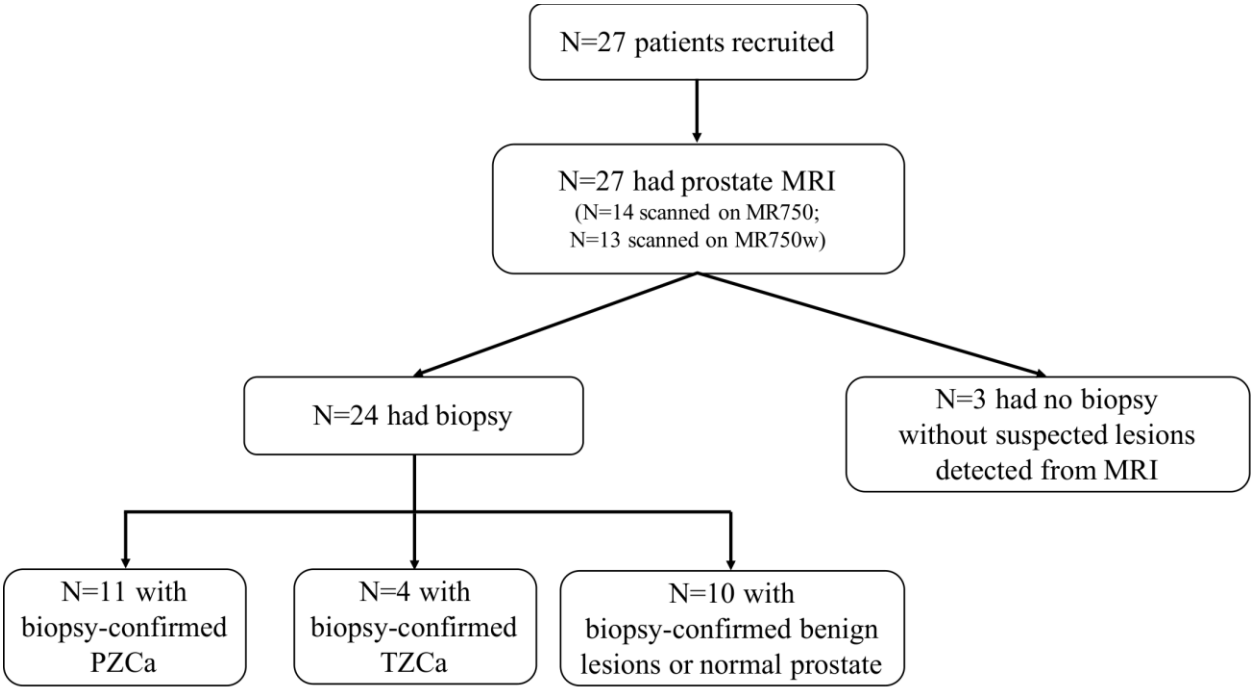

Figure 11. Patient Recruitment Design.
Overview of study design of patients with suspected prostate cancer. Among the patients with biopsy-confirmed PZCa and TZCa, one overlapping patient was diagnosed to have both PZ and TZ lesions.

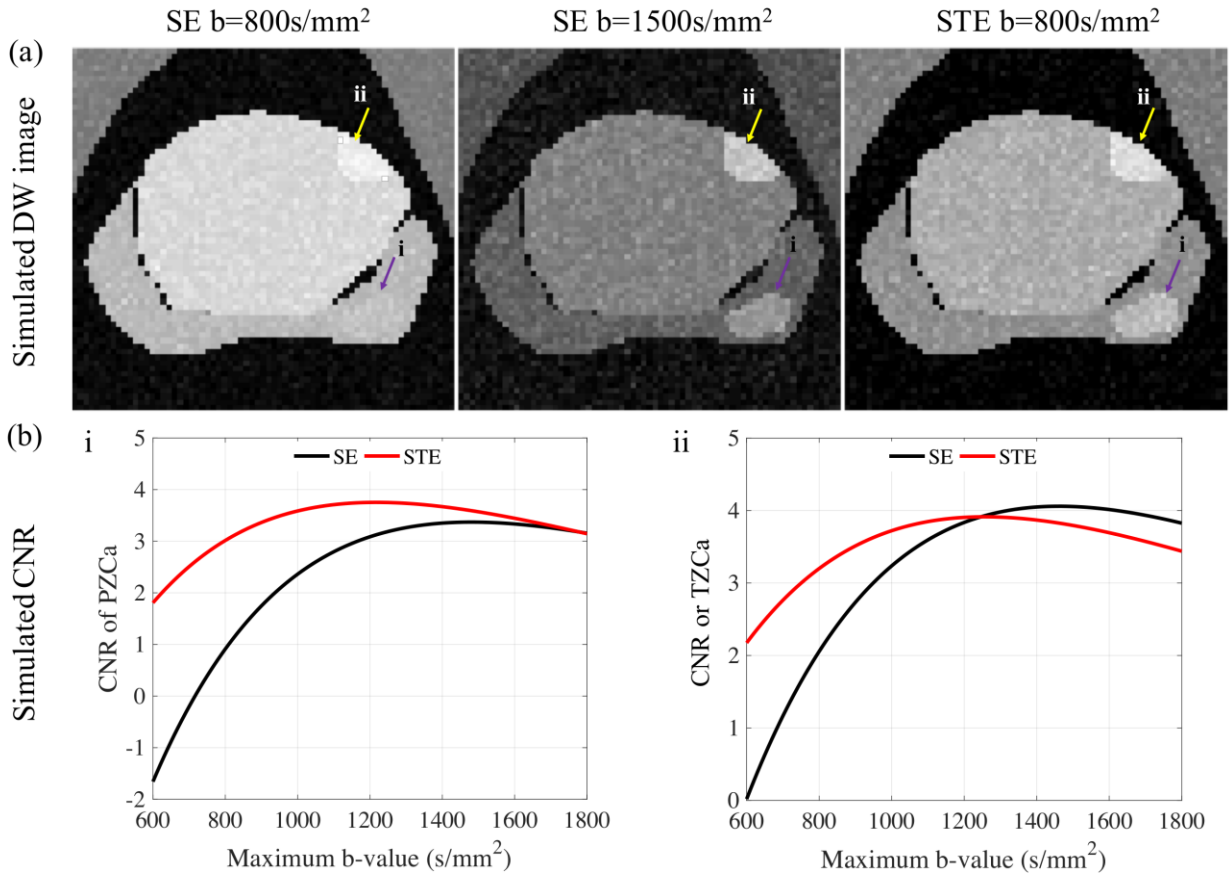

Figure 12. Numerical prostate phantom simulation to compare SE and STE DWI signal. Simulated prostate DW images from SE b=800 s/mm2, SE b=1500 s/mm2 and STE b=800s/mm2 are shown in (a). SE b=800 s/mm2 has minimal contrast between the simulated PCa lesions and normal prostate tissue, whereas both SE b=1500 s/mm2 and STE b=800s/mm2 have substantial contrast between PCa and normal tissue. The corresponding CNR as a function of b-value is shown in plot (b) for a PCa lesion in the peripheral zone (i) and transition zone (ii). STE DWI at a moderate b-value is able to provide similar or higher CNR compared to SE DWI with a high b-value, especially in the peripheral zone.

Table 4. Acquisition Protocol of Prostate Patients.

Scanner	Coil	Sequence	b-values (#Averages)	TE (ms)	TR (s)	Acquisition time
GE 750 **G_{max}=50mT/m** **SR_{max}=200mT/m/s**	32-channel torso array	SE DWI	100(6), 800(12)	55.5	4.5	~4-5min
		SE DWI	100(6), 1500(15)	64.1		~5-7min
		STE DWI	100(6), 800(15)	34.7		4min16s
GE 750w **G_{max}=33mT/m** **SR_{max}=120mT/m/s**	30-channel cardiac array	SE DWI	100(6), 800(12)	64.3	4~6	~4-5min
		SE DWI	100(6), 1500(15)	74.5	4~6	~5-7min
		STE DWI	100(6), 800(15)	45.6	4	4min16s

3.2.4 Quantitative Assessment

Region-of-interest (ROI) measurements were obtained in normal PZ tissue, normal TZ tissue and biopsy-confirmed PCa lesions from the ADC maps of the three DWI sequences. For each acquisition, SNR maps and CNR were calculated as follows:

$$SNR = \frac{\hat{S}}{\hat{\sigma}} \tag{13}$$

and

$$CNR = \frac{\hat{S}_{PCa} - \hat{S}_{normal}}{\hat{\sigma}_{normal}}, \tag{14}$$

where $\hat{S}$ is the estimated signal amplitude and $\hat{\sigma}$ is the estimate of noise standard deviation. The signal amplitude and noise standard deviation maps were estimated using an iterative Rician expectation-maximization estimator, with spatially varying noise considered[73]. The same co-localized ROIs were used to measure the SNR and CNR in normal tissue and biopsy-confirmed PCa lesions.

3.2.5 Qualitative Image Assessment

The three acquired DWI series (SE b=800s/mm^2, SE b=1500 s/mm^2, STE b=800 s/mm^2) were de-identified and reviewed independently by 3 abdominal radiologists with 18, 9 and 1 years of experience interpreting prostate MRI (FK, SAW, BT). In addition, the acquired T2-weighted images (oblique axial and coronal), as well as the ADC map calculated from one of the DWI series (STE) were provided to the radiologists to provide further aid in the DWI image quality assessment. The order of the DWI series was randomized for each patient. The radiologists, blinded to clinical and pathologic data, interpreted the prostate MRI examinations using PI-RADS version 2.1 lexicon

(REF). The locations of PI-RADS 3, 4 and 5 lesions were documented. The DWI series were evaluated qualitatively and ranked in terms of the following criteria: 1) SNR of the prostate, 2) CNR between lesion and normal prostate and 3) overall image quality / diagnostic confidence. For each criterion, the radiologists ranked the three DWI series from best to worst on a 3-point Likert scale (1-best, 3-worst). Additionally, any inconsistencies regarding lesion detectability among the three DWI series (i.e., if a lesion can be detected in some series but not in others) were reported by each of the readers.

3.2.6 Statistical Analysis

The ratio t-test was used for pair-wise comparison of quantitative SNR and CNR measurements between STE b=800 s/mm^2 and SE b=800 s/mm^2 DW images, as well as between STE b=800 s/mm^2 and SE b=1500 s/mm^2 DW images. The two-sample t-test was conducted to compare ADC measurements between PCa and normal prostate tissue. This test was performed separately for PZ and TZ, as well as for each of the three sequences. To compare the ADC contrast (i.e., ADC difference between PCa and adjacent normal tissue) across sequences, a paired t-test was used between each pair of sequences.

The pair-wise differences of readers' qualitative preference in terms of SNR, CNR and overall image quality / diagnostic confidence were analyzed using the Wilcoxon Signed rank test. The comparison performed was between STE b=800 s/mm^2 and SE b=800 s/mm^2 DW images, as well as between STE b=800 s/mm^2 and SE b=1500 s/mm^2 DW images. The preference rankings of DWI sequences for PCa lesions in the PZ and in the TZ were analyzed separately.

3.3 Results

3.3.1 Simulation

The simulated prostate DW images and CNR between PCa and normal prostate tissue at different b-values are presented in **Figure 12**. As shown in Figure 12(a), both SE b=1500 s/mm^2 and STE b=800 s/mm^2 images are able to show the PCa lesion in the PZ (i) and TZ (ii) with high CNR. However, the simulated PCa lesions are not easily detectable on SE b=800 s/mm^2 due to T2 shine-through effect. As shown in Figure 12(b), STE DWI at moderate b-values (i.e. from around 800 to 1200 s/mm^2) may enable improved CNR compared to SE DWI acquired even at high b-values.

3.3.2 Quantitative Assessment of Patient Results

The ROI measurements of SNR and CNR for the three DWI sequences are shown in **Table 5**, where the p-values of pair-wise ratio t-test are also presented. Significant improvement ($p<0.0001$) of SNR can be found in the quantitative measurements of STE b = 800 s/mm^2 compared to SE b = 1500 s/mm^2 in both PZ and TZ. Improvement of CNR from STE b = 800 s/mm^2 can also be seen in the PZ compared to both SE b=800 s/mm^2 ($p<0.01$). The CNR of STE b = 800 s/mm^2 is comparable to the high b-value SE b = 1500 s/mm^2 images with no significant differences shown.

Table 6 compares the ADC values between normal tissue in all patients (N=27) and malignant lesions in the PZ (N=11) and TZ (N=4) for the three DWI sequences, respectively. The Box and Whisker plots comparing the ADC of PCa (a) and the ADC of normal tissue (b) in patients

with biopsy-confirmed lesions across the three DWI sequences are also shown in **Figure 13**. Significant difference ($p<0.0001$) between ADC of normal tissue and PCa can be seen in all the three sequences. However, as shown in Figure 13c, SE b=800 s/mm^2 and STE b=800 s/mm^2 have higher ADC contrast (between PCa and normal tissue) compared to SE b=1500 s/mm^2 ($p<0.05$). Further, no significant difference in ADC measurements was observed between SE b = 800 s/mm^2 and STE b = 800 s/mm^2, whereas a significant ADC underestimation was observed in SE b = 1500 s/mm^2 compared to either of the b = 800 s/mm^2 acquisitions.

Table 5. Quantitative measurements of SNR and CNR in patients.

Metrics		**SE**		**STE b=800s/mm^2**	**p-value**
SNR	PZ	b=800 s/mm^2	16.1±4.0	16.2±3.4	0.80
		b=1500 s/mm^2	13.3±2.9		<0.0001
	TZ	b=800 s/mm^2	18.7±3.2	17.8±3.3	0.22
		b=1500 s/mm^2	12.8±2.3		<0.0001
CNR	PZ PCa	b=800 s/mm^2	3.3±1.7	5.3±2.1	<0.01
		b=1500 s/mm^2	5.4±2.8		0.89
	TZ PCa	b=800 s/mm^2	6.7±3.5	5.2±2.1	0.34
		b=1500 s/mm^2	6.0±2.5		0.54

Table 6. Quantitative measurements of ADC in patients.

ADC ($\times 10^{-3}$mm^2/s)	**PZ**			**TZ**		
	Normal tissue (N=27)	Malignant lesion (N=11)	p-value	Normal tissue (N=27)	Malignant lesion (N=4)	p-value
SE b=800 s/mm^2	1.62±0.32	0.89±0.20	<0.0001	1.34±0.16	0.75±0.17	<0.0001
SE b=1500 s/mm^2	1.31±0.25	0.74±0.19	<0.0001	1.11±0.14	0.68±0.13	<0.0001
STE b=800 s/mm^2	1.52±0.26	0.86±0.23	<0.0001	1.30±0.16	0.76±0.07	<0.0001

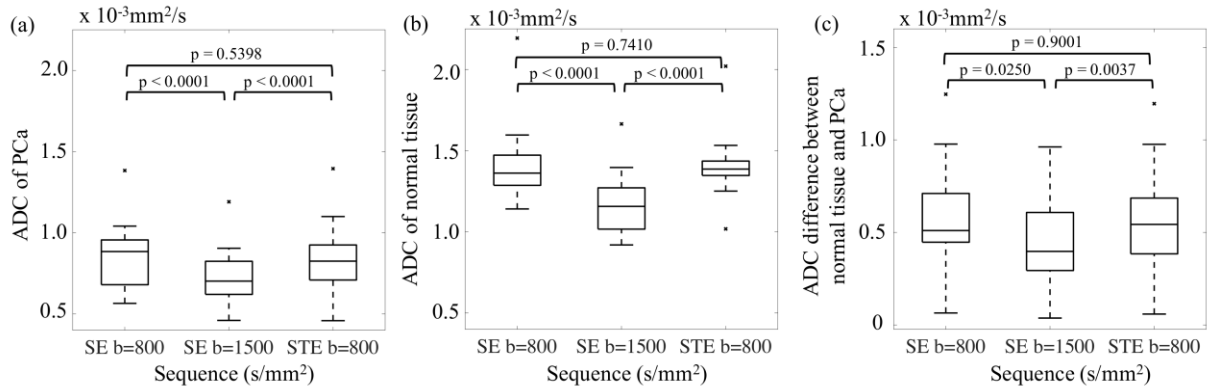

Figure 13. Comparison of ADC measurements of PCa and normal tissue in patients. Box and Whisker plots to compare the ADC of PCa, the ADC of normal tissue and the ADC difference between PCa and normal prostate tissue in patients with PCa lesions across the three DWI sequences. Both PCa lesions in PZ and TZ are included in these plots. The p-values from pairwise t-tests are labeled in the plots. ADC measurements are similar between SE b=800 s/mm^2 and STE b=800 s/mm^2. However, both ADC (a-b) and ADC difference (c) are lower in SE b=1500 s/mm^2.

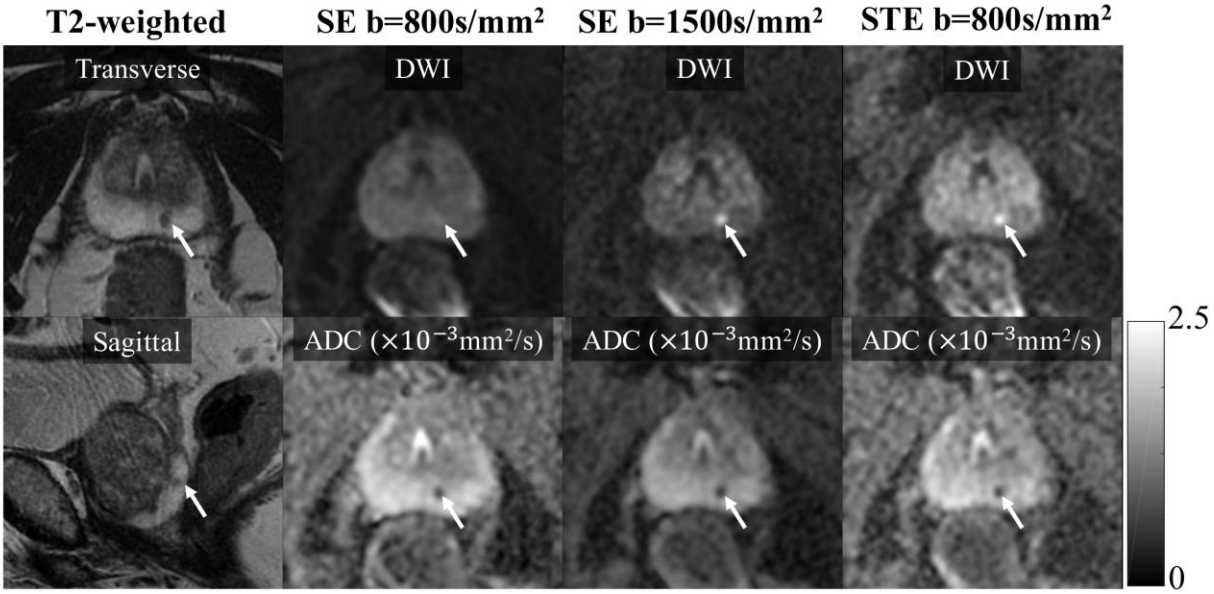

Figure 14. Representative images from a patient with PCa in Peripheral Zone. Representative images from a 67-year-old patient with PI-RADS 4 and Gleason score 3+3 cancer in the left PZ (white arrows). Significant T2-shinethrough effect between normal PZ tissue and PCa can be observed in the SE b=800s/mm^2 DW image. Both SE b=1500s/mm^2 and STE b=800s/mm^2 DWI

provide improved contrast, clearly showing the lesion. All ADC maps are able to clearly depict the lesion.

3.3.3 Qualitative Assessment of DW Images

The results from the qualitative reader study are shown in **Table 7**. For each ranking metric (SNR, CNR and overall image quality / diagnostic confidence), the frequency and p-value of when STE b=800 s/mm^2 is superior to SE b=800 s/mm^2 and when STE b=800 s/mm^2 is superior to SE b=1500 s/mm^2 are shown for the three readers, respectively.

The ranking of SNR of STE b=800 s/mm^2 is higher ($p<0.0001$) than SE b=1500 s/mm^2 for all the three readers. Reader 2 and reader 3 prefer the CNR performance in the PZ of STE b=800 s/mm^2 over SE b=800 s/mm^2 with $p<0.05$; Reader 1 prefers to the CNR of PZ lesions in SE b = 1500 s/mm^2 over STE b = 800 s/mm^2 ($p<0.01$). For TZ lesions, the CNR of STE b=800 s/mm^2 is better than SE b=800 s/mm^2 in all TZ PCa cases, but is inferior to SE b=1500 s/mm^2, for the three readers. For the overall image quality or diagnostic confidence, STE b=800 s/mm^2 surpasses SE b=800 s/mm^2 for reader 2 ($p<0.01$) and reader 3 ($p<0.0001$); SE b=1500 s/mm^2 is significantly preferred by reader 3 while the other two readers indicate no significant preference between STE b = 800 s/mm^2 and SE b = 1500 s/mm^2.

Table 7 (d) presents results of lesion detectability across all patients with malignant lesions identified by the readers. Among the three sequences, both SE b=1500 s/mm^2 and STE b=800 s/mm^2 enable the detection of all the lesions for all the three readers, which demonstrates the comparable lesion detectability of the two sequences. However, SE b=800 s/mm^2 results in more

than three missed lesions for each reader, indicating the negative impact of T2-shinethrough effect on lesion detectability.

3.3.4 Patient Examples

Representative images for three patients are shown in **Figure 14-16**. **Figure 14** presents the high-resolution T2-weighted images, three DW images and their corresponding ADC maps from a 67-year-old patient diagnosed with a PI-RADS 4 and Gleason score 3+3 cancer in the left PZ (arrows). Significant T2-shinethrough effect between normal PZ tissue and PCa can be seen in the SE b=800s/mm^2 DW image. Both SE b=1500s/mm^2 and STE b=800s/mm^2 DWI provide improved contrast, clearly showing the lesion. **Figure 15** is a case with two prostate adenocarcinomas, one in the right PZ (PI-RADS 5, Gleason 4+4, arrowheads) and one in the left TZ (PI-RADS 4, Gleason 3+3, arrows). T2-shinethrough effect can be particularly seen between normal TZ tissue and the TZ PCa lesion in the SE b=800s/mm^2 DW image. In these two patients, ADC maps from all three acquisitions enable clear depiction of these lesions.

Figure 16 shows results from a 64-year-old patient with PI-RADS 3 and Gleason score 4+3 adenocarcinoma in the TZ. The T2-weighted signal is only slightly hypointense than the surrounding normal tissue, thus T2-shinethrough effect is minimal. In this case, lesions are visible in all three DWI series and SE b=1500 s/mm^2 appears to have the highest contrast because of the high b-value and low T2-shinethrough effect.

Table 7. Reader study: qualitative assessment of patients with suspected prostate cancer.

a) SNR of prostate tissue	**STE b=800 superior to SE b=800**		**STE b=800 superior to SE b=1500**	
	n (%)	p-value	n (%)	p-value
Reader 1	7 (25.9%)	<0.05	25 (92.6%)	<0.0001
Reader 2	20 (80.0%)	<0.05	25 (92.6%)	<0.0001
Reader 3	8 (29.6%)	<0.05	27 (100%)	<0.0001

b) CNR of malignant lesions	**PZ PCa**				**TZ PCa**			
	STE b=800 superior to SE b=800		STE b=800 superior to SE b=1500		STE b=800 superior to SE b=800		STE b=800 superior to SE b=1500	
	n (%)	p-value	n (%)	p-value	n (%)	p-value	n (%)	p-value
Reader 1	7 (87.5%)	0.070	0 (0.0%)	<0.01	3 (100%)	N/A	0 (0.0%)	N/A
Reader 2	8 (88.9%)	<0.05	2 (22.2%)	0.31	3 (100%)	N/A	0 (0.0%)	N/A
Reader 3	9 (100%)	<0.01	3 (33.3%)	0.51	3 (100%)	N/A	0 (0.0%)	N/A

c) Overall image quality/Diagnostic confidence	**STE b=800 superior to SE b=800**		**STE b=800 superior to SE b=1500**	
	n (%)	p-value	n (%)	p-value
Reader 1	18 (66.7%)	0.068	9 (33.3%)	0.17
Reader 2	21 (80.8%)	<0.01	12 (46.2%)	1.0
Reader 3	24 (88.9%)	<0.0001	8 (29.6%)	<0.05

(d) Lesion detectability	**#Total patients with malignant lesions detected**	**# Patients with malignant lesions undetectable**		
		SE b=800	SE b=1500	STE b=800
Reader 1	11	3 (27.3%)	0	0
Reader 2	11	6 (54.6%)	0	0
Reader 3	11	7 (63.6%)	0	0

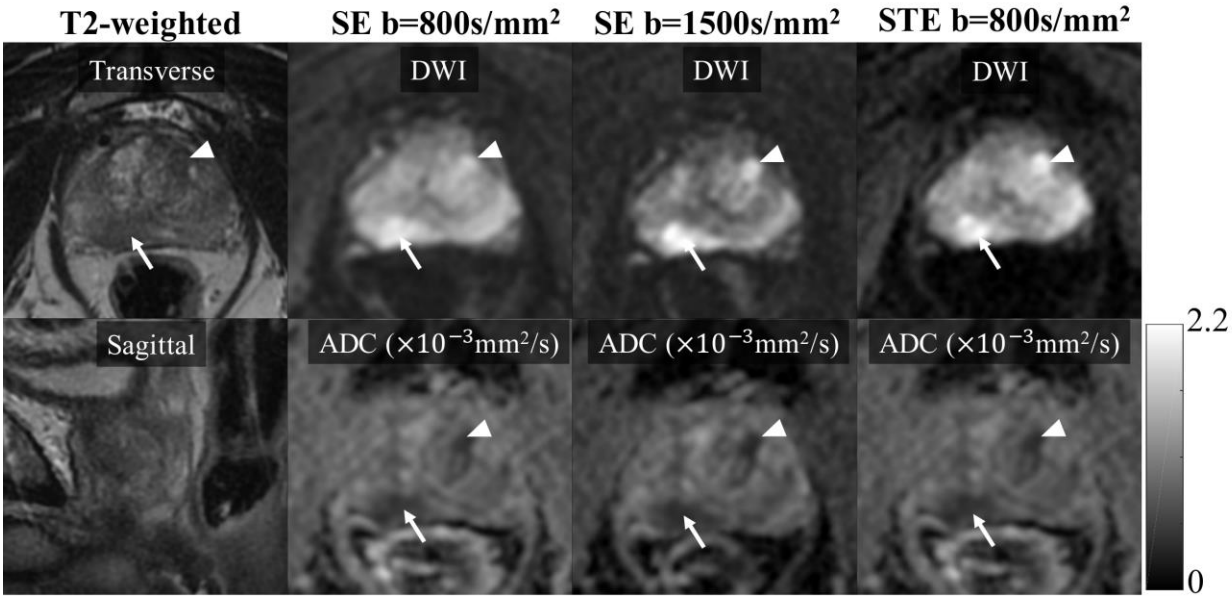

Figure 15. Representative images from a patient with PCa in Peripheral Zone and Central Gland. A 69-year-old patient with PI-RADS 5 and Gleason score 4+4 adenocarcinoma in the right PZ (white arrows), as well as a PI-RADS 4 and Gleason score 3+3 adenocarcinoma in the left TZ (white arrowheads), was acquired. T2-shinethrough effect is particularly shown between normal TZ tissue and the TZ PCa lesion in the SE b=800 s/mm^2 DW image. Both SE b=1500s/mm^2 and STE b=800s/mm^2 DWI provide improved contrast. All ADC maps are able to clearly show the lesions.

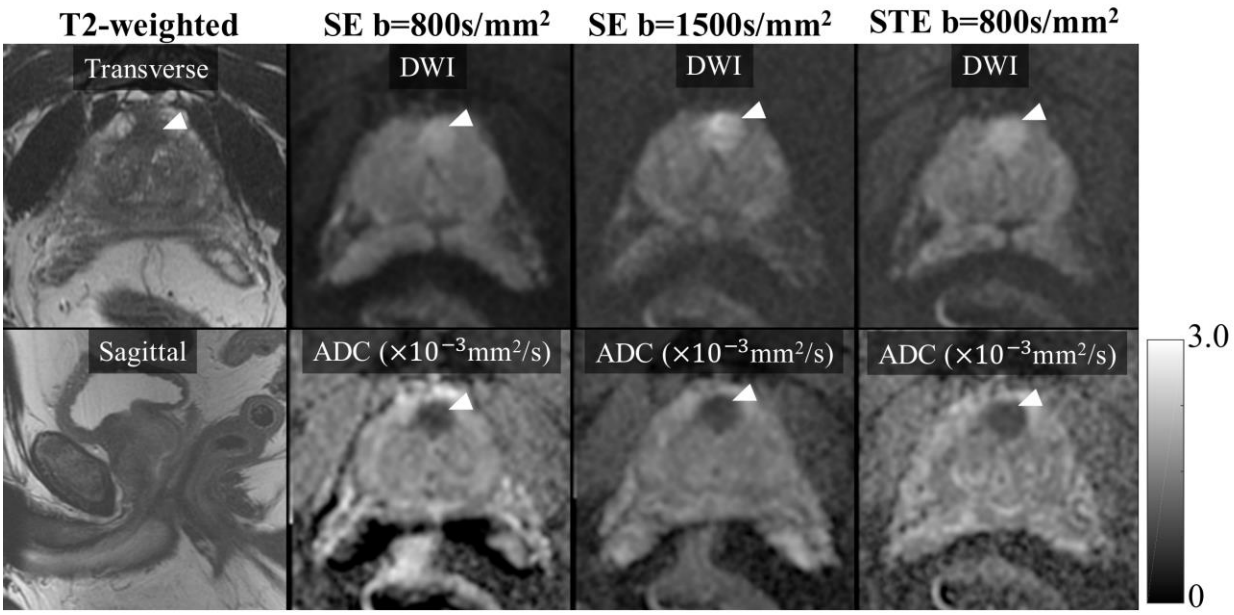

Figure 16. Representative images from a patient with PCa in Peripheral Zone. A 64-year-old patient with PI-RADS 3 and Gleason score 4+3 adenocarcinoma in the TZ (arrowheads). The T2-weighted signal is only slightly hypointense than the surrounding normal tissue, thus T2-shinethrough effect is minimal. In this case, lesions are visible in all three DWI series and SE b=1500 s/mm2 appears to have the highest contrast because of the high b-value and low T2-shinethrough effect.

3.4 Discussion

In this study, we have assessed the ability of STE DWI of the prostate to overcome the inherent tradeoffs with SE DWI, in order to obtain high CNR and reliable ADC maps in a single acquisition. Based on quantitative evaluation, STE DWI at moderate b-value has significant advantage in SNR over high b-value SE DWI and comparable CNR performance to high b-value SE DWI. From qualitative assessment from the reader study, all readers have shown preference to STE b=800 s/mm^2 DWI over SE b=1500s/mm^2 in terms of SNR. Most readers prefer the CNR of SE b = 1500 s/mm^2 and the overall diagnostic confidence of SE b = 1500 s/mm^2 and STE b = 800 s/mm^2 is shown to be comparable. However, the number of identified lesions from SE b = 1500 s/mm^2 and STE b = 800 s/mm^2 indicates that both sequences have clinically reliable lesion detectability compared to SE b = 800 s/mm^2.

In the qualitative assessment, it is noticeable that most readers prefer the CNR performance of SE b = 1500 s/mm^2 even though the quantitative measurements of CNR were similar between SE b = 1500 s/mm^2 and STE b = 800 s/mm^2. This may suggest that the radiologists' familiarity with the SE DWI contrast was important in their assessment. The fact that STE b = 800 s/mm^2 has less T2-shinethrough effect results in the smooth appearance of its images in normal prostate tissues, which raised concerns among radiologists. However, based on the lesion detectability, STE b = 800 s/mm^2 is promising in terms of achieving high SNR and high CNR performance in a single acquisition. Further, these results also serve as motivation for further optimization of the STE DWI acquisitions.

The choice of b-values for prostate DWI has been widely discussed in the literature. A number of studies have compared the image quality and diagnostic sensitivity/specificity of moderate b-value (around 1000 s/mm^2) DWI and high b-value (≥1500 s/mm^2) DWI[37–40,74–77]. The

use of ultra-high b-value is still controversial due to its trade-off between lesion conspicuity and image quality. To balance this trade-off, different strategies have been investigated especially in the peripheral zone to avoid ultra-high b-values. For example, the PI-RADS 2.1[31] guidelines proposed the use of a moderate b-value (800-1000 s/mm^2) and also a high b-value (>1400 s/mm^2) with calculated ADC maps to facilitate diagnosis. Methods that use synthetic DWI with different post-processing approaches[78–82] have also been proposed to reduce the T2 shine-through effect of SE DWI and to obtain DW images with high lesion contrast. However, the effect of synthetic DWI is still not fully understood[81,82] in terms of image quality and accuracy compared to directly acquired images. Consequently, two different series with different b-values (one moderate b-value and one high b-value) are often used in the clinic (e.g., at our site). The results of this study suggest that a single STE DWI acquisition at moderate b-value may provide sufficient image quality and quantitative reliability within a short scan time. The ADC measurements in this manuscript also agree with previous studies[27,33,39,83,84]. We found that STE DWI with moderate mixing time (~100s/mm^2) can produce reliable ADC maps that are consistent with SE DWI b=800s/mm^2 acquisitions. In comparison, ADC maps calculated from high b-value DWI have smaller difference between normal tissue and PCa likely due to restricted diffusion and noise-floor effects[36]. Consequently, STE DWI has the potential to provide both high quality DW images and reliable ADC maps within a single sequence. Furthermore, STE DWI can be extended to investigate restricted diffusion by varying the diffusion time without changing b-values[57,85–87] and perform multi-parametric mapping (i.e. T1, T2 and quantitative diffusion maps)[70].

This study also has some limitations. First, this is a preliminary study conducted with a small number of patients. Larger patient studies are needed to further evaluate the clinical feasibility of STE DWI in the assessment of prostate cancer. In addition, whole mount histology

is not routinely used at our institution. Therefore, the correlation between biopsy results and MRI is performed cognitively by radiologists. Further, the reader study was performed with DW images of the three sequences evaluated simultaneously. Future evaluation will also include independent, blinded comparison of STE and SE DWI for lesion detection. In addition, to compare between STE DWI and the clinical SE DWI sequences in a controlled manner, the STE DWI b value was set at 800 s/mm2 (the same as the low b value SE DWI acquisition). However, improved CNR performance for STE DWI may be achievable with slightly higher b values (e.g. 1000 s/mm^2). Further, only a single choice of TM (100 ms) within STE DWI was evaluated due to scan time limitations. At TM = 100 ms, the TE can be substantially reduced compared to SE DWI and the T1-decay during the mixing time is negligible. However, further optimization of TM may be possible. Finally, this study included only scans at 3T using surface coils. Although the fundamental behavior of STE DWI compared to SE DWI is expected to remain similar, the specific performance comparison may vary with field strength (e.g. at 1.5T) or choice of coil (e.g. endorectal coil).

3.5 Conclusion

In conclusion, this work demonstrated that STE DWI has the potential to overcome the limitations of conventional SE DWI, in order to provide high-SNR, high-CNR imaging of prostate cancer while also enabling reliable ADC mapping.

Chapter

4. Motion-Robust and Blood-Suppressed M1-Optimized Diffusion Imaging (MODI) in the Liver[3]

4.1 Purpose

As discussed in **Section 1.2.3**, Liver DWI is challenging because of the relatively short T2 relaxation time of liver tissue, which often results in low SNR at moderate and high b-values, as well as the motion sensitivity of diffusion encoding sequences. Non-rigid bulk tissue motion (e.g. non-rigid motion of a voxel imparted by the motion of the heart) introduces extra phase dispersion in liver DWI signal, particularly in the left lobe[43,44]. This motion-induced phase dispersion results in signal voids in the DW images and bias in subsequent quantitative diffusion measurements, including overestimation of ADC values.

---

[3] This work has been published in: Zhang Y, Peña-Nogales Ó, Holmes JH, Hernando D. Motion-robust and blood-suppressed M1-optimized diffusion imaging of the liver. *Magn Reson Med.* 2019;82(1):302-311.

Recently, advanced DW gradient waveform design techniques have been proposed to provide first-moment (M1) and/or second-moment (M2) motion-nulled DWI by solving an optimization algorithm to obtain the shortest achievable echo time (TE) for a given b-value[45,46]. These techniques enable motion-robust DW images with optimized SNR. However, the motion-robust gradient waveforms also compensate the signal from moving blood, which is nulled in traditional liver DWI. This lack of blood signal nulling will result in bright spots from blood vessels (i.e., "unsuppressed'" blood) even at relatively high b-value DW images. Consequently, the unsuppressed blood signal will have high ADC estimation and introduce overall bias in ADC maps. Importantly, unsuppressed blood signal can mimic focal liver lesions and may confound the assessment and detection of true focal lesions in both DWI and ADC mapping.

Several strategies have been proposed to obtain DW images and ADC maps without contamination from blood signals. In recent work, Moulin et al.[88] acquired liver DWI with various M1 values, and used a generalization of the intra-voxel incoherent motion (IVIM) signal model to include velocity encoding of the blood signal into the parameter estimation process. Unfortunately, this approach requires lengthy acquisitions and may not directly provide blood-suppressed DW images. Additionally, Van et al.[89] applied partial velocity compensation by combining velocity compensation in the frequency and slice encoding axes and traditional diffusion encoding in the phase encoding axis to achieve motion compensation while eliminating the blood signal. However, this approach did not include optimized diffusion weighting gradient waveforms, resulting in potentially lengthened TEs, and only applied partial velocity encoding in the A/P direction, which may not be optimal when images are acquired at different stages of the cardiac cycle (**Figure 17**). For these reasons, there is an unmet need for a robust and optimized technique for motion-robust DWI with reduced residual blood signal.

Therefore, the purpose of this work is to develop and evaluate a M1-Optimized Diffusion Imaging (MODI) technique for motion-robust and blood-suppressed liver DWI with optimized diffusion gradient waveforms.

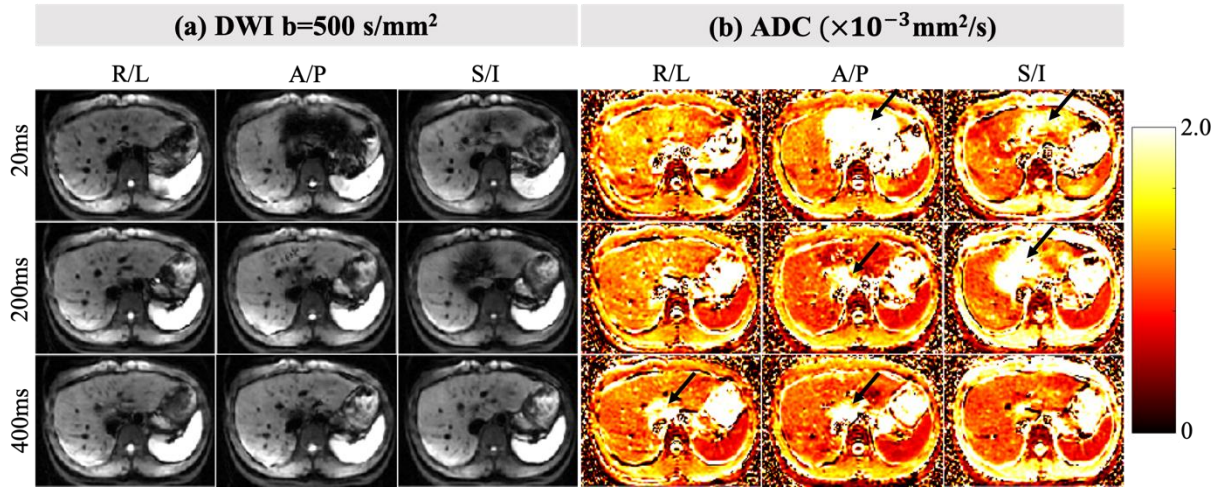

Figure 17. Directional signal void and ADC bias in liver DW-MRI. Single slice diffusion weighted images from monopolar gradient acquisitions were obtained with different cardiac trigger delays within a single breath-hold. Three orthogonal diffusion encoding directions (R/L, A/P and S/I) were obtained separately. DW images with b=500s/mm^2 and the corresponding ADC maps are shown in this figure. Black arrows indicate the location of motion-induced ADC bias (eg: resulting from cardiac motion). Importantly, the presence of motion-induced signal voids is highly spatially variable, and depends on the diffusion direction as well as the time within the cardiac cycle.

4.2 Theory

4.2.1 First-Moment (M1) Motion Sensitivity

The first-moment motion sensitivity of a diffusion encoding waveform, G(t), can be described as follows:

$$M1 = \gamma \int_0^{T_{diff}} G(t) t dt \tag{15}$$

where γ = 42.58 MHz/T for ^{1}H and T_{diff} is the diffusion encoding period. Note that M1 and G(t) are generally vectors. However, in this study we formulate the waveform optimization for a given diffusion direction, and therefore use scalars to describe M1 and G(t), for simplicity of notation.

For a conventional Spin echo Stejskal-Tanner diffusion sequence with monopolar diffusion weighting[3], the absolute value of M1 will increase with increased b-value. It is well known that, at commonly used high b-values (e.g. b = 500 s/mm^2), monopolar diffusion weighting results in high M1 values and is affected by motion-induced signal voids.

In motion-compensated methods[45,46], M1 is usually set to zero to null the phase dispersion from bulk tissue motion, therefore mitigating bulk motion induced signal loss. However, M1-nulled acquisitions may also lead to bright signals from blood even at relatively high b-values. This is highly undesirable for liver DWI, as bright blood signals may confound the interpretation of DW images and introduce bias in ADC measurements, which will hinder the diagnosis and characterization of lesions.

However, at moderate b-values (e.g. b = 50-100 s/mm^2), monopolar diffusion weighting results in moderate M1 values ranging from 0.1 to 0.27 s/mm that enable blood suppression[90] while avoiding substantial motion-induced signal voids. Based on these observations, in this work we seek to develop optimized diffusion weighting waveforms that provide a constant, moderate M1 with increasing b-value. The desired value of M1 (on the order of the M1 typically obtained with monopolar gradients for b-values between 50-100 s/mm^2) enables blood suppression but avoids substantial motion-induced signal voids. The approach for obtaining such optimized diffusion weighting gradients is described in detail next.

In the proposed method, we apply a modified version of the optimized diffusion gradient design (ODGD) motion-compensated formulation proposed in Pena et al.[46], but enforcing a small non-zero M1 value in the optimization formulation, in order to enable blood signal suppression while maintaining high motion robustness.

4.2.2 Design of the Highest Desired b-value

A desired high b-value b_h is achieved by modifying the ODGD formulation to include a pre-specified, non-zero M1 = α s/mm. The cost function and remaining pulse sequence and hardware constraints are the same as the original ODGD formulation, modified to include a non-nulled M1 constraint.

In this formulation, TE is minimized for a given b-value, by evaluating different TEs iteratively. At each iteration, the proposed algorithm maximizes the achievable b-value for the given TE. The MODI formulation for the highest b-value is the following optimization problem:

$$\mathrm{G}(t) = \underset{G}{\operatorname{argmax}}\, b(G) \tag{16}$$

where

$$\mathrm{b} = \gamma^2 \int_0^{T_{diff}} \left(\int_0^t G(\tau)d\tau\right)^2 dt, \tag{17}$$

with the constraints described below.

1) Moment constraints

To refocus the static spins, M0 is designed to be nulled in diffusion encoding waveforms:

$$M0 = \gamma \int_0^{T_{diff}} G(t)dt. \tag{18}$$

To reduce the non-rigid bulk motion-induced signal loss but diphase the blood signal, a moderate M1 value is used in the MODI formulation as follow:

$$M1 = \gamma \int_0^{T_{diff}} G(t)tdt = \alpha. \quad (19)$$

2) Concomitant gradient constraint

The first-order concomitant gradient effect can be nulled by incorporating the following nonlinear constraint for each diffusion encoding direction[46]:

$$\gamma \int_0^{TE/2} G(t)^2 dt - \gamma \int_{\frac{TE}{2}}^{T_{diff}} G(t)^2 dt = 0 \quad (20)$$

3) Other constraints

Other constraints are used to satisfy the gradient strength, slew rate and timing of a Spin-Echo DWI sequence.

$$G(T_{RF90}) = 0 \quad (21)$$

$$G(T_{RF180}) = 0 \quad (22)$$

$$G(T_{EPI}) = 0 \quad (23)$$

$$|G(t)| \leq G_{max} \quad (24)$$

$$|\frac{dG(t)}{dt}| \leq SR_{max} \quad (25)$$

where T_{RF90} is the duration of 90° excitation pulse, $T_{RF180}$is the duration of the 180° inversion pulse and T_{EPI} is the time between the start of readout to the TE. G_{max} and SR_{max} are the maximum gradient strength and maximum slew rate, respectively, along the desired diffusion direction. When designing for multiple diffusion directions, the most restrictive constraints among all acquired directions are used to obtain the same TE for all diffusion directions.

Specific values of M1 implemented in this work are described below in Methods. Once the optimized high b-value waveform, $G_h(t)$, has been designed, the remaining lower b-value waveforms are designed as described next.

4.2.3 Design of Remaining Lower b-values

In this paper, the waveforms of the remaining lower b-values are constructed to mimic a derated version of the high b-value waveform, as well as to maintain the M1 and TE of the high b-value waveform. The procedure for obtaining the optimized waveform for each of the lower b-values is illustrated in **Figure 18**. Because of the linearity of M1 as a function of the gradient waveform (**Equation 15**), the high b-value waveform $G_h(t)$, optimized with the formulation described above, can be decomposed into two waveforms to facilitate the design of lower b-value waveforms as follows:

$$G_h(t) = G_{M1n}(t) + G_{M1}(t) \tag{26}$$

where $G_{M1n}(t)$ is a M1-nulled component and $G_{M1}(t)$ is the monopolar component of the MODI waveform with M1=αs/mm. Both $G_{M1n}(t)$ and $G_{M1}(t)$have the same TE as $G_h(t)$.

In the last step, a scaled version of the M1-nulled waveform $G_{M1n}(t)$ (i.e., $c \cdot G_{M1n}(t)$) will be recombined with $G_{M1}(t)$ (unaltered) to achieve the desired low b-value b_l while maintaining the M1 value, as follows:

$$G_l(t) = c \cdot G_{M1n}(t) + G_{M1}(t) \tag{27}$$

where the scaling parameter c is determined through an iterative search (using a binary search algorithm) to match the desired lower b-value using the combined waveform.

Note that in this study, $G_{M1}(t)$ is kept constant over multiple b-values to maintain a constant M1 value. In this way, multiple non-zero b-values b_l with the same first moment M1 can be constructed within certain b-value limits determined by the b-value of the monopolar component and the constraints on slew rate and gradient strength. The proposed waveforms can

also be designed in arbitrary directions with proper weighting of the three orthogonal diffusion directions considering the directionally dependent maximum slew rate SR_{max} and maximum

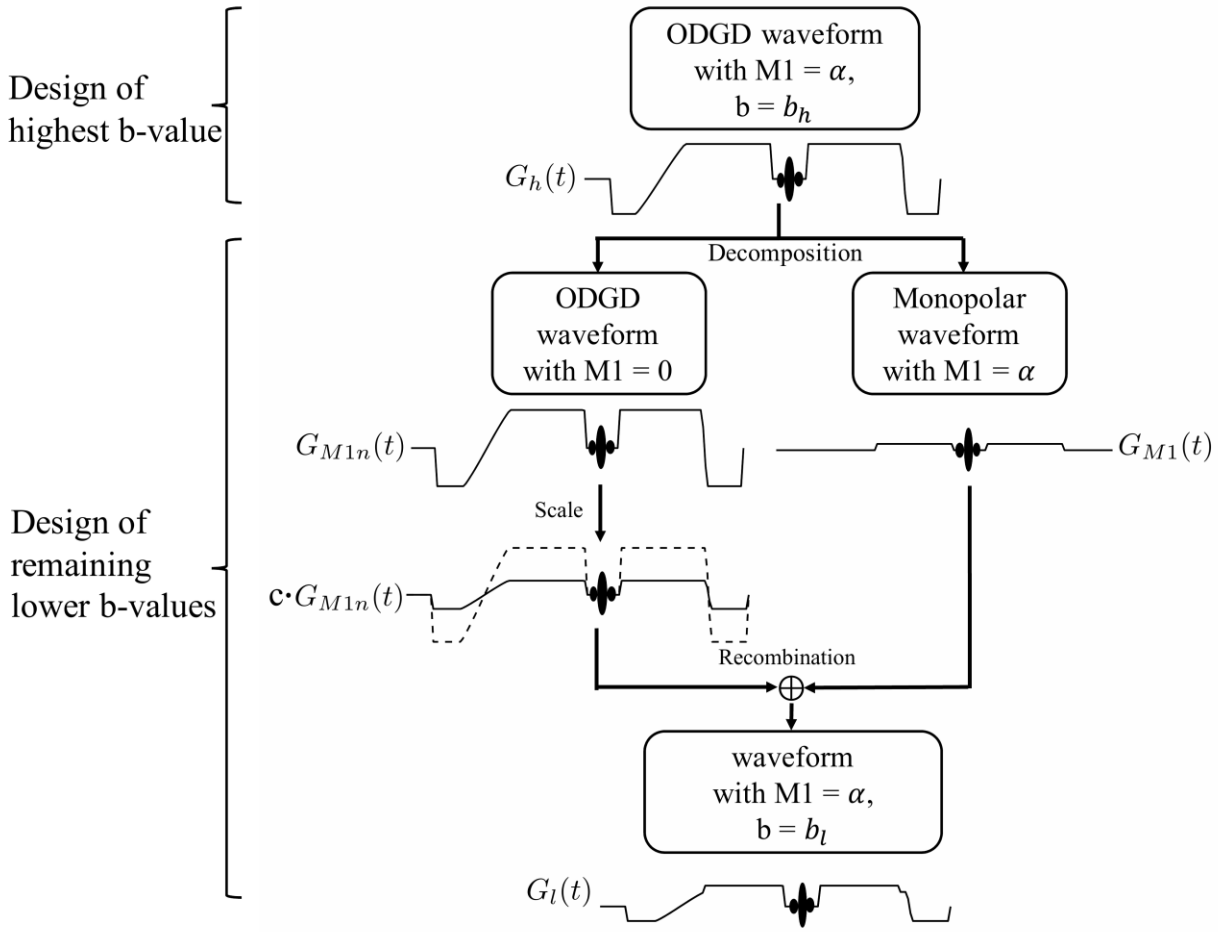

Figure 18. Procedure of MODI waveform design. The design includes two steps: design of the highest b-value and design of the remaining lower b-values. Note that $G_{M1n}(t)$ is different from $G_h(t)$ because of the fully nulled M1 in $G_{M1n}(t)$, even though the difference is visually subtle. $G_{M1}(t)$ is the monopolar component of $G_h(t)$, which is kept constant for the design of the remaining lower b-values.

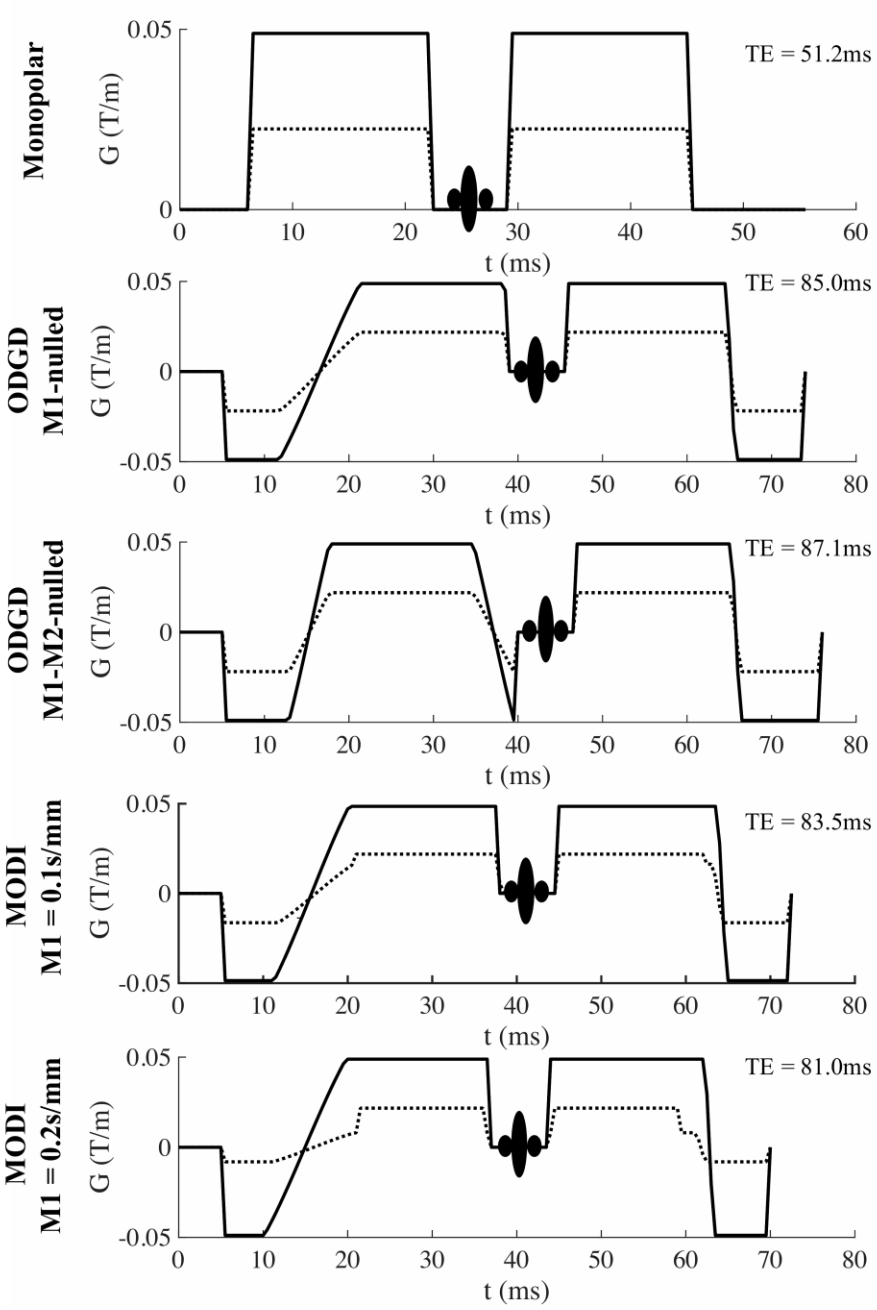

Figure 19. Diffusion encoding waveforms applied in the *in-vivo* experiments. Solid lines represent the waveforms for b_h = 500s/mm^2; dashed lines represent the waveforms for b_l = 100s/mm^2. The achievable TE for each waveform is labeled on each plot.

gradient strength G_{max} .When multiple diffusion directions are acquired, the most restrictive constraints across all desired directions will be used in the gradient waveform design, to maintain the same TE for each diffusion direction.

4.3 Methods

4.3.1 Diffusion Encoding Waveform Design

In this study, the specific constraints used in the ODGD optimization formulation are T_{EPI} = 10.5ms, T_{RF90} = 5.5 ms, T_{RF180} = 6 ms, G_{max} = 50 mT/m and SR_{max} = 150 T/m/s. A sequential quadratic programming (SQP) algorithm was used to solve the optimization formulation subject to upper and lower bounds, linear equality constraints, linear inequality constraints and a quadratic equality constraint, with detailed constraints shown in the **Section 4.2.2**. The optimization was run with a time step of 500μs in Matlab2015a (3.5GHz Intel Core i5).

As shown in **Figure 19**, four optimized waveforms were constructed and compared to the conventional monopolar diffusion encoding waveform. The four waveforms included ODGD waveforms with M1-nulled and M1-M2-nulled, as well as two MODI waveforms. MODI waveforms were constructed with M1 = 0.1 s/mm and M1 = 0.2 s/mm, corresponding to the M1 value of the conventional Stejskal-Tanner monopolar diffusion gradients with b-values between b = 50 s/mm^2 and b = 100 s/mm^2, respectively. All the constructed waveforms were optimized with concomitant gradient nulling to avoid ADC bias[46].

The solid lines in **Figure 19** represent the diffusion encoding waveforms for b = 500 s/mm^2 and the dashed lines represent waveforms for b = 100 s/mm^2. The design of b_h = 500 s/mm^2 and

b_l = 100 s/mm^2 for the MODI waveforms was performed following the description in the **Section 4.2.3**.

4.3.2 Image Acquisitions

All acquisitions in this study were performed in a HIPAA compliant manner after IRB approval and informed written consent.

Eight healthy volunteers were recruited for the *in-vivo* evaluation of MODI waveforms. Diffusion weighted images were acquired on a 3T scanner (GE MR750 Waukesha, WI) with a 32-channel torso coil (Neocoil, Pewaukee, WI). All five waveforms shown in **Figure 19** were acquired with b (average)=[100(4), 500(8)]s/mm^2, where b=100s/mm^2 is applied to avoid IVIM effects[90]. For each acquisition, respiratory triggering was applied with effective TR of approximately 10 seconds. The acquisition time for each waveform was between eight to ten minutes, depending on the respiratory rate of specific volunteers. Multiple slices were acquired to cover the entire liver. Acquisitions were performed with interleaved slices within one effective TR; different repetitions of a single b-value, different diffusion directions as well as different b-values were obtained in different TRs. Other acquisition parameters include: FOV = 32cmx32cm, in-plane resolution = 2.5mmx2.5mm, slice thickness = 6mm, bandwidth = $\pm$250kHz, parallel imaging acceleration factor R=2, 75% partial Fourier acquisition and diffusion encoding direction = three orthogonal directions.

Stimulated Echo Acquisition Mode (STEAM) multi-TE single-voxel spectroscopy[91] was applied to the right lobe of the liver of each volunteer within a breath-hold, to record the T2 values of the liver.

Five patients with suspected hepatic lesions were scanned with the same setup as the healthy volunteer study. DW images using conventional monopolar diffusion waveform, ODGD waveform with M1-nulling, and MODI waveform with M1 = 0.2 s/mm were acquired under respiratory triggering, with the same parameters as in the healthy volunteer.

4.3.3 Image Analysis

In the healthy volunteer experiment, averaged ADC maps of three diffusion directions were calculated for each diffusion encoding waveform. Co-localized regions of interest (ROIs) were drawn in each of the nine Couinaud liver segments for each diffusion waveform acquisition. ROIs were drawn in the same regions for all volunteers, and the averaged ADC measurements as well as the standard deviation across volunteers were calculated.

To evaluate the possible association of ADC measurements with liver segment (as would be expected in the presence of spatially-varying motion-induced artifacts) for each diffusion encoding waveform, a linear mixed-effect (LME) fitting model was applied with both liver segments and volunteers as random effects. The standard deviation of ADC measurements across liver segments and its corresponding confidence interval were calculated to evaluate the consistency over segments.

Bland-Altman analysis was also performed to study the possible bias in ADC obtained in the right (segments 5, 6, 7 and 8) and left (segments 1, 2, 3, 4a and 4b) liver lobes from each diffusion waveform. The ADC measurements from monopolar waveforms are accurate in the right lobe because the right lobe suffers less from cardiac-related motion; therefore, monopolar waveform in the right lobe is used as our reference in this study. Two different measures of agreement of each waveform in the right and left lobe with the reference were performed: (i) the

averaged bias across all subjects ($p<0.05$ was considered significant); (ii) the 95% limits of agreement (LOA) between individual measurements were also calculated. For each acquisition, the ADC measurements of right lobe and left lobe were calculated by averaging the measurements from the corresponding liver segments.

In the patient experiment, averaged ADC maps from the three diffusion directions were calculated for each diffusion encoding waveform. Images were analyzed for motion-related artifacts and residual blood signal. ADC measurements were performed in the observed lesions, as well as in healthy tissues in the right and left liver lobe.

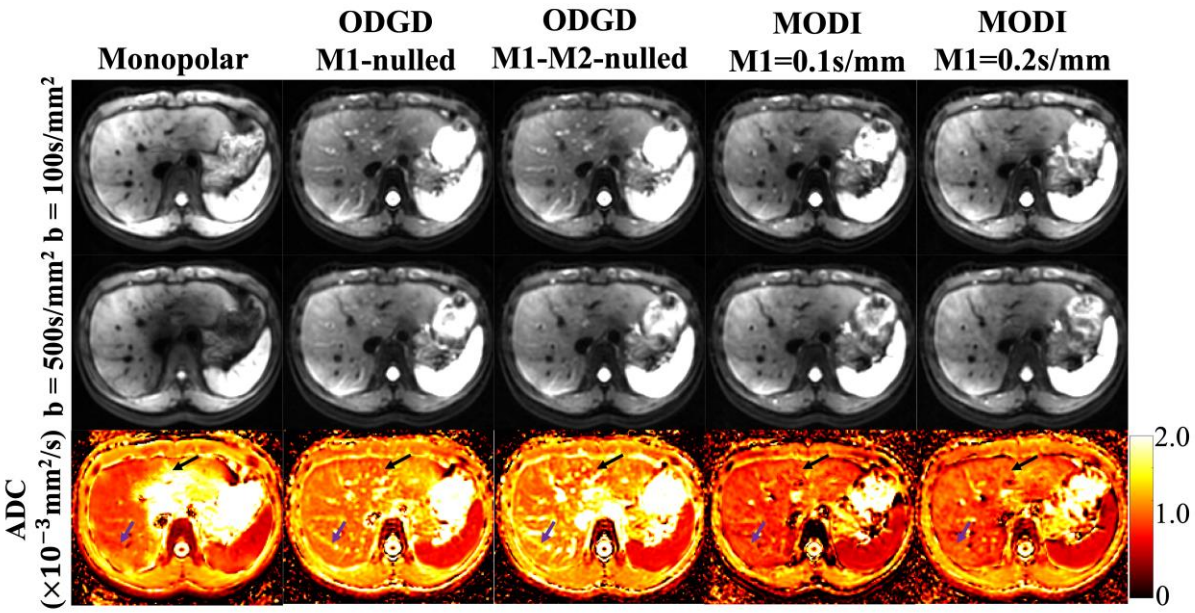

Figure 20. Example liver DW images and ADC maps from one healthy volunteer. ADC bias can be found in the left liver lobe (black arrows) from the monopolar waveform acquisition, which is mitigated by the other waveforms. In the ADC maps from ODGD M1-nulled and ODGD M1-M2-nulled, even though there is reduced ADC bias, there is substantial unsuppressed signal from blood vessels. In contrast, MODI-based liver DWI demonstrates high robustness to motion as well as substantial blood signal suppression (purple arrows).

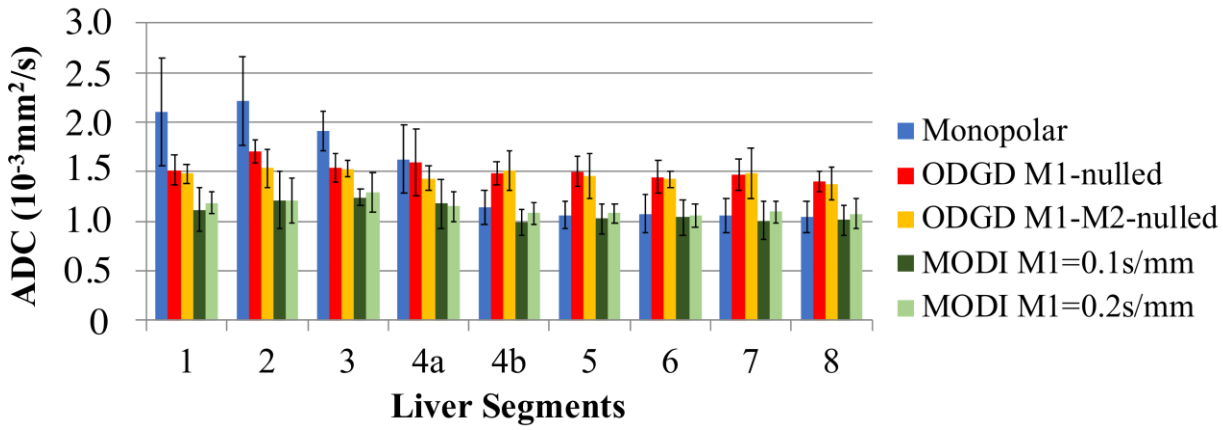

Figure 21. Plot of ADC measurements over the nine liver segments in healthy volunteers. Each bar shows the average ADC across all volunteers for the corresponding liver segment, and each error bar shows the standard deviation of ADC across all volunteers. Using the monopolar ADC measurements in the right liver lobe (including segments 5, 6, 7 and 8) as the reference, substantial ADC bias can be observed in monopolar ADC measurements in segments 1, 2, 3 and 4a. Motion moment-nulled (ODGD M1-nulled and M1-M2-nulled) acquisitions result in ADC bias throughout the entire liver compared to the conventional monopolar ADC measurements in the right lobe, likely due to the unsuppressed blood signals. In contrast, MODI waveforms are able to provide lower bias and more consistent ADC measurements throughout all segments, which is also shown quantitatively in **Table 9**.

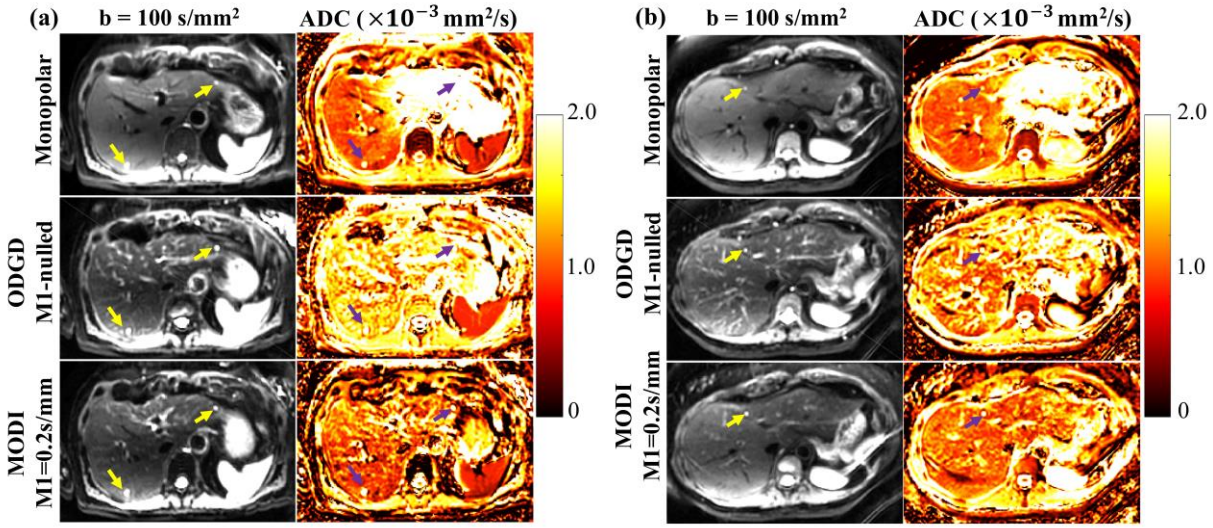

Figure 22. Representative DW images and ADC maps from two patients. (a) a patient with one cyst in the left lobe (LL) and one cyst in the right lobe (RL) and (b) a patient with one cyst in the LL. The yellow and purple arrows point to the lesions for each patient in the DW images and ADC maps, respectively. The proposed MODI acquisition provides high motion robustness (avoiding the large bias present in the left lobe with monopolar acquisitions), as well as substantial blood signal suppression (avoiding the bright blood signals that are present in previously proposed motion moment-nulled acquisitions). This suggests the proposed MODI may enable improved visualization and quantitative assessment of lesions throughout the entire liver.

4.4 Results

The MODI waveform with a pre-specified M1=α were optimized within 135 seconds. The healthy volunteers had an average T2 relaxation time of 26.3 ± 4.0ms. Example DW images (b = 100 s/mm^2 and b = 500 s/mm^2) as well as ADC maps from one healthy volunteer are shown in **Figure 20**. **Figure 21** presents the ROI measurements of ADC in different liver segments.

Results of the LME analysis are shown in **Table 8**. The standard deviation of ADC across different liver segments for each diffusion waveform and its 95% confidence interval are listed. The variability, shown as the standard deviation, of the ADC measurements from the monopolar waveform across liver segments is much larger than the other waveforms. ADC measurements from the ODGD M1-M2-nulled waveform show negligible variation among liver segments. MODI waveforms have similar standard deviation compared to ODGD M1-nulled, which are all about ten times smaller than the monopolar waveform.

The Bland-Altman analysis of the ADC measurements from the two ODGD waveforms and the two MODI waveforms compared to the reference ADC of the right lobe from the monopolar waveform is presented in **Table 9** and **Figure 23**. The ADC measurements from ODGD waveforms (M1-nulled and M1-M2-nulled) have significant bias compared to the reference ADC measured in the right lobe from the monopolar waveform. In comparison, no significant difference has been observed for measurements from the MODI waveforms arising from either the right or the left lobe of the liver.

The acquisitions were successful in all patient volunteers. The acquired images were evaluated by a radiologist who is experienced in abdominal MRI. In this manuscript, two representative patient imaging examples are shown in **Figure 22**. **Figure 22** (a) shows two cysts within the liver, one in the left lobe and one in the right lobe. The two lesions can be observed

from the DW images of all three waveforms; but only the ADC maps of ODGD M1-nulled and MODI M1=0.2s/mm can show the lesions clearly. Compared to the MODI waveform, the detection of lesion of ODGD M1-nulled can be confounded by the bright signal from blood vessels. Another representative example from a different patient is shown in **Figure 22** (b), in which case a cyst is present in the left lobe. In both cases, quantitative characterization of lesions based on ADC is affected by the large bias present in left lobe measurements from monopolar acquisitions due to cardiac-induced bulk motion. Similarly, the presence of artifactually high ADC may confound the detection and quantification of lesions in M1-nulled and M1-M2-nulled acquisitions. In contrast, MODI enables visualization of lesions with substantial suppression of blood signals and robustness to motion throughout both liver lobes in both patient volunteers. Similar results were consistently observed in all patient volunteers in this preliminary study.

Table 8. Random effects analysis of ADC measurements (x10^{-3} mm^2/s) over different liver segments.

Waveform	Standard deviation	Confidence interval (95%)
Monopolar	0.45	[0.28, 0.74]
ODGD *M*1-nulled	0.06	[0.02, 0.16]
ODGD *M*1–*M*2-nulled	3.1×10^{-8}	N/A*
MODI *M*1 = 0.1 s/mm	0.07	[0.03, 0.16]
MODI *M*1 = 0.2 s/mm	0.06	[0.03, 0.13]

*N/A: confidence interval could not be calculated because of near-zero standard deviation.

Table 9. Bland-Altman analysis of ADC measurements (x10^{-3} mm^2/s), compared to the ADC in the right lobe of monopolar waveform.

Waveform	Liver area	Bias	*p*-value	LOA (95%)
Monopolar	Left lobe	0.72	<.01	[0.43, 1.00]
ODGD *M*1-nulled	Left lobe	0.51	<.01	[0.21, 0.81]
	Right lobe	0.39	<.01	[0.00, 0.79]
ODGD *M*1–*M*2-nulled	Left lobe	0.44	<.01	[0.13, 0.75]
	Right lobe	0.37	<.01	[−0.12, 0.86]
MODI *M*1 = 0.1 s/mm	Left lobe	0.09	.23	[−0.29, 0.47]
	Right lobe	−0.04	.47	[−0.30, 0.23]
MODI *M*1 = 0.2 s/mm	Left lobe	0.10	.09	[−0.17, 0.36]
	Right lobe	0.00	.84	[−0.2, 0.22]

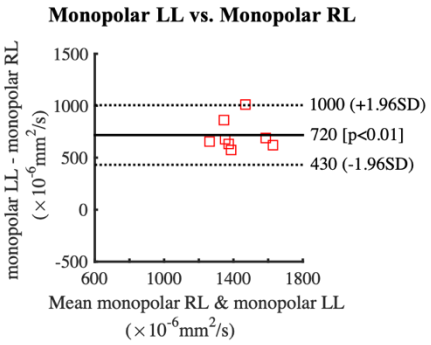
Monopolar LL vs. Monopolar RL
monopolar LL - monopolar RL
(×10^-6 mm^2/s)
1500
1000
500
0
-500
600
1000
1400
1800
1000 (+1.96SD)
720 [p<0.01]
430 (-1.96SD)
Mean monopolar RL & monopolar LL
(×10^-6 mm^2/s)

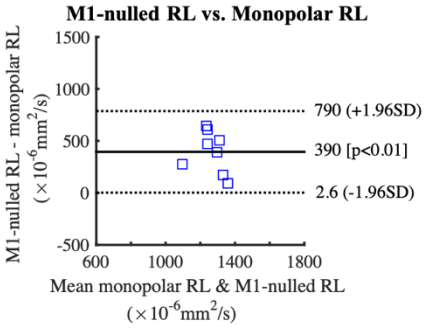
M1-nulled RL vs. Monopolar RL
M1-nulled RL - monopolar RL
(×10^-6 mm^2/s)
1500
1000
500
0
-500
600
1000
1400
1800
790 (+1.96SD)
390 [p<0.01]
2.6 (-1.96SD)
Mean monopolar RL & M1-nulled RL
(×10^-6 mm^2/s)

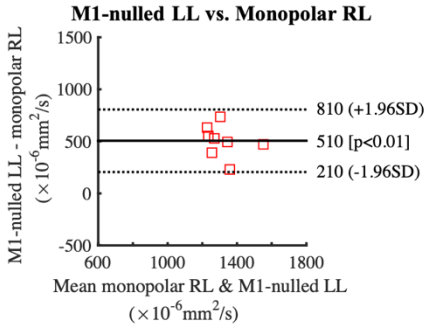
M1-nulled LL vs. Monopolar RL
M1-nulled LL - monopolar RL
(×10^-6 mm^2/s)
1500
1000
500
0
-500
600
1000
1400
1800
810 (+1.96SD)
510 [p<0.01]
210 (-1.96SD)
Mean monopolar RL & M1-nulled LL
(×10^-6 mm^2/s)

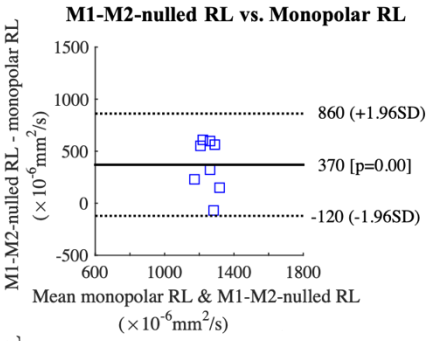
M1-M2-nulled RL vs. Monopolar RL
M1-M2-nulled RL - monopolar RL
(×10^-6 mm^2/s)
1500
1000
500
0
-500
600
1000
1400
1800
860 (+1.96SD)
370 [p=0.00]
-120 (-1.96SD)
Mean monopolar RL & M1-M2-nulled RL
(×10^-6 mm^2/s)

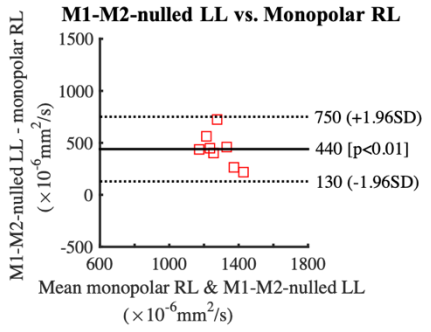
M1-M2-nulled LL vs. Monopolar RL
M1-M2-nulled LL - monopolar RL
(×10^-6 mm^2/s)
1500
1000
500
0
-500
600
1000
1400
1800
750 (+1.96SD)
440 [p<0.01]
130 (-1.96SD)
Mean monopolar RL & M1-M2-nulled LL
(×10^-6 mm^2/s)

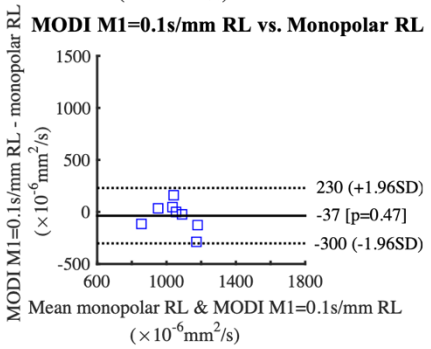
MODI M1=0.1s/mm RL vs. Monopolar RL
MODI M1=0.1s/mm RL - monopolar RL
(×10^-6 mm^2/s)
1500
1000
500
0
-500
600
1000
1400
1800
230 (+1.96SD)
-37 [p=0.47]
-300 (-1.96SD)
Mean monopolar RL & MODI M1=0.1s/mm RL
(×10^-6 mm^2/s)

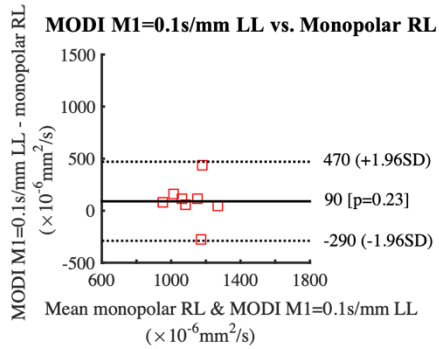
MODI M1=0.1s/mm LL vs. Monopolar RL
MODI M1=0.1s/mm LL - monopolar RL
(×10^-6 mm^2/s)
1500
1000
500
0
-500
600
1000
1400
1800
470 (+1.96SD)
90 [p=0.23]
-290 (-1.96SD)
Mean monopolar RL & MODI M1=0.1s/mm LL
(×10^-6 mm^2/s)

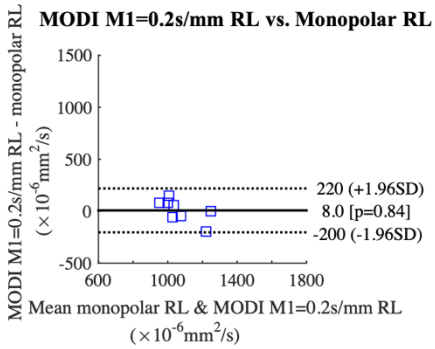
MODI M1=0.2s/mm RL vs. Monopolar RL
MODI M1=0.2s/mm RL - monopolar RL
(×10^-6 mm^2/s)
1500
1000
500
0
-500
600
1000
1400
1800
220 (+1.96SD)
8.0 [p=0.84]
-200 (-1.96SD)
Mean monopolar RL & MODI M1=0.2s/mm RL
(×10^-6 mm^2/s)

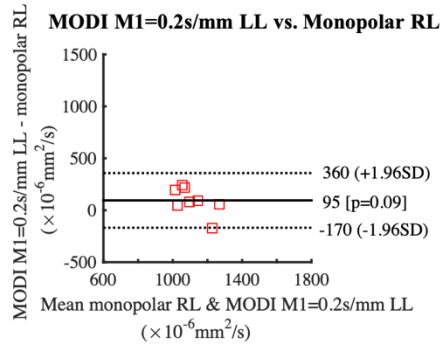
MODI M1=0.2s/mm LL vs. Monopolar RL
MODI M1=0.2s/mm LL - monopolar RL
(×10^-6 mm^2/s)
1500
1000
500
0
-500
600
1000
1400
1800
360 (+1.96SD)
95 [p=0.09]
-170 (-1.96SD)
Mean monopolar RL & MODI M1=0.2s/mm LL
(×10^-6 mm^2/s)

Figure 23. Bland-Altman plots in healthy volunteers. In these plots, individual ADC measurements for each healthy subject and liver lobe are compared to the monopolar ADC measurement in the right lobe (which is largely free from cardiac motion induced bias). Plots with blue markers in the first column show measurements in the right lobe; plots with red markers in the second columns show measurements in the left lobe. Monopolar acquisitions (row 1) lead to bias in the left lobe, whereas moment-nulled acquisitions (rows 2-3) lead to ADC bias in both right and left lobes due to the unsuppressed blood signal. In contrast, MODI acquisitions (rows 4-5) lead to low bias in both right and left liver lobes.

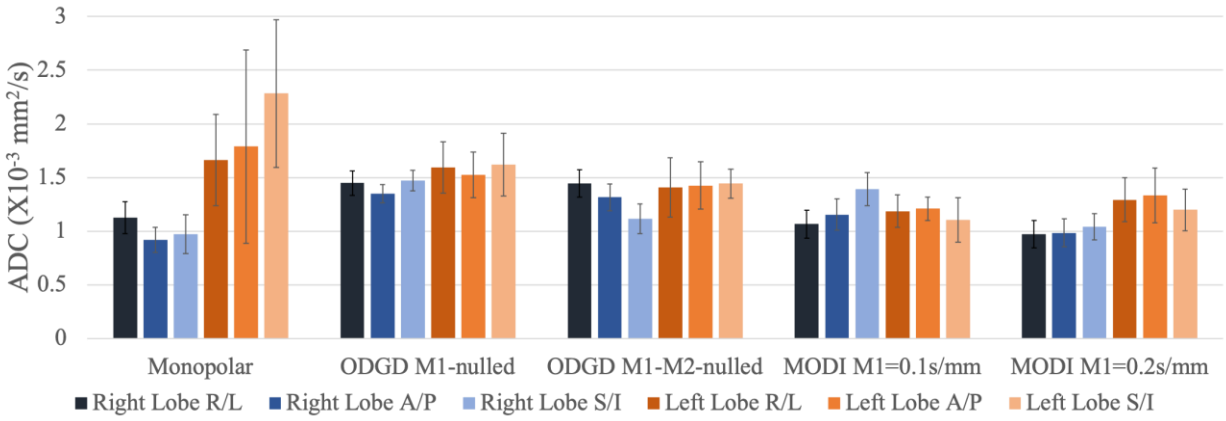

Figure 24. Directional ADC measurements in healthy volunteers. ROI measurements of ADC values in the right and left liver lobes, from acquisitions with various diffusion waveforms applied along different diffusion directions (S/I, R/L, and A/P). Averaged ADC measurements and their standard deviation across the eight volunteers are shown in this bar plots. Acquisitions with monopolar diffusion gradients lead to substantial bias between left and right lobe and variability in the left liver lobe for each of the three diffusion directions, demonstrating that none of these directions is free from the presence of motion-related signal voids. The proposed method is able to produce qualitatively more consistent ADC measurements in the left liver lobe for any diffusion direction compared to the monopolar waveform.

4.5 Discussion

In this study, a M1-Optimized Diffusion Imaging (MODI) method was proposed to acquire motion-robust, blood-suppressed liver DWI with optimized diffusion encoding waveforms. Healthy volunteer experiments and a feasibility evaluation in patients have been performed to investigate the bias of the proposed MODI method.

Compared to the conventional monopolar DWI, MODI is able to provide ADC measurements with reduced bias, particularly in the left lobe of the liver. In contrast to the moment-nulling waveforms[45,46], MODI can dephase most of the blood signal throughout the liver and generate more reliable ADC maps. Overall, the proposed MODI method is promising for obtaining reliable DW images and quantitative ADC measurements over the entire liver.

Another advantage of MODI is its ability to be applied in arbitrary diffusion directions, whereas a recently proposed partial velocity encoding method[89] is only performed in A/P direction. Importantly, even though some studies have concluded that cardiac motion-induced signal voids are minimized by applying DW gradients in the A/P direction[44], our preliminary results suggest that substantial motion-induced signal voids are present even with diffusion encoding along the A/P direction. Further, these signal voids appear highly dependent on the stage of the cardiac cycle, which is difficult to control in practice due to scan time constraints. **Figure 24** shows an example of ADC bias induced by cardiac motion in three orthogonal diffusion directions for each waveform, which demonstrates the effectiveness of MODI waveform in different diffusion directions. Because of this ability of MODI, other commonly used diffusion directions like tetrahedral gradients[92] can also be applied in the future.

ADC measurements of the liver from the literature have a large variation across studies, because of the different choices of b-values, diffusion times and ROI selection[93–96]. In our healthy volunteer experiments, the averaged ADC measurements in the right lobe of the monopolar waveform are similar to the results from previous literature when performed with a similar b-value choice[96]. Our measurements also agree with previous measurements of true diffusion coefficient from the IVIM model[97,98]. Our measured ADC values from motion moment-nulled ODGD waveforms showed similar values compared to previous motion moment-nulled liver DWI[45,46,92].

The proposed method for optimizing diffusion encoding waveforms is promising for the reliable clinical application of liver DWI. However, the current implementation still has some limitations. The moderate M1 values implemented in this study were 0.1 s/mm and 0.2 s/mm, which correspond to the approximate M1 value of a typical monopolar acquisition with b-values between 50 s/mm^2 and 100 s/mm^2. Although this work has demonstrated the potential of the proposed moderate M1 approach, the specific choice of M1 value should be optimized in future work. In MODI, the M2 value is not explicitly controlled. The necessity of M2-nulling for liver diffusion imaging is still unknown due to the important trade-off caused by substantially longer TE, which is problematic given the relatively short T2 of liver tissue. However, because the general shape of the optimized M1-optimized waveforms inherently includes partial M2 rephasing, the M2 value of the MODI waveform is already about 50% lower than the monopolar waveform at b=500s/mm^2. MODI also needs to be evaluated in a large number of patients to investigate its performance for lesion detection and characterization throughout the entire liver, compared to alternative waveforms.

In this study, the waveform for the highest b-value is designed via an optimization problem constrained by the desired M1. Even though the global optimum is not guaranteed because of the

non-convex formulation , the TE optimized under the current implementation has been proved to be shorter than existing methods[46]. Subsequently, the highest b-value waveform is decomposed into an M1-nulled and a monopolar component (with the desired M1). Next, waveforms for lower b-values are designed by combining a scaled version of the M1-nulled component and the (unaltered) monopolar component, in order to maintain a constant M1 value and TE throughout all b-values. The advantage of this strategy is the ability to mimic a derated version of the high b-value waveform, analogously to conventional multi-b-value acquisitions with other waveforms. Also, instead of using multiple optimization steps to obtain optimized waveforms for each b-value, this decomposition strategy is computationally faster. However, the limitation of this approach is that the achievable b-value of the lower b-value waveforms will have upper and lower limits due to the maximum gradient strength and the b-value of monopolar component.

In addition, liver DW images (including MODI) sometimes contain residual artifacts from the failure of fat suppression in the presence of B0 field inhomogeneity. More robust fat suppression methods like STIR[99] are fully compatible with the proposed method. Also, the TE of MODI DW images is longer than the conventional monopolar sequence (although MODI provides shorter TE than the M1-nulled ODGD sequence). This longer TE leads to an SNR loss, particularly in patients with short T2 relaxation times in the liver, as occurs in the presence of iron overload. Nevertheless, the improved reliability of liver DW images and ADC maps obtained with MODI likely present a worthwhile trade-off in a variety clinical and research applications, particularly those performed in modern MR scanners with high-SNR and powerful gradient systems.

4.6 Conclusion

In conclusion, this study has developed and demonstrated the feasibility of a M1-Optimized Diffusion Imaging (MODI) method for the acquisition of motion-robust, blood-suppressed liver DWI. This novel method for diffusion gradient waveform design enables DWI of the liver with high robustness to motion and suppression of blood signals, overcoming the limitations of conventional monopolar waveforms and moment-nulled waveforms, respectively.

Chapter

5. Quantitative Diffusion MRI using Reduced Field-of-View (rFOV) and Multi-Shot Acquisition Techniques[4]

5.1 Introduction

Prostate DWI is typically performed with single-shot echo planar imaging (ssEPI) techniques, due to their reliability and robustness to motion. Importantly, ssEPI based DWI has been demonstrated to show significant contrast between malignant and benign peripheral zone tissues[66,100]. However, ssEPI of the prostate often suffers from severe image distortion due to the presence of susceptibility-related field inhomogeneity[3]. The prostate is located directly under the bladder and in front of the rectum. This complicated anatomic environment including abrupt

[4] Part of this work has been published in: Zhang Y, Holmes J, Rabanillo I, Guidon A, Wells SA, Hernando D. Quantitative Diffsion MRI using Reduced Field-of-View and Mlti-Shot Acquisition Techniques. *J Magn Reson Imaging.* 2019. doi:10.1002/jmri.26849.

susceptibility differences between prostate tissue and the air in the rectum will result in severe field inhomogeneity. This field inhomogeneity introduces significant distortion in ssEPI images, which are obtained over a long readout time. This distortion in ssEPI-DWI results in reduced image quality and poor co-localization with other imaging sequences, and may complicate the accurate measurement of quantitative diffusion parameters within and around the prostate.

Novel pulse sequences based on reduced field-of-view (rFOV)[49,50] and multi-shot EPI (msEPI)[51,52] acquisitions have been proposed to reduce these image distortions by enabling shorter readout times. Specifically, rFOV enables a shorter EPI echo-train length by applying a spatially-selective RF pulse to excite a limited FOV in the phase encoding direction. Alternatively, msEPI acquires multiple shots (where each shot requires a shorter echo train with reduced readout time) in the phase-encoding direction to reduce distortion artifacts. Importantly, both rFOV and msEPI enable DWI imaging with higher resolution and higher overall image quality including greater resolvable spatial resolution and reduced distortions[50,51]. In recent studies, both rFOV and msEPI have been shown to provide improved diffusion-weighted image quality for prostate cancer detection compared to conventional ssEPI[101–106].

Quantitative diffusion measurements (such as ADC) have tremendous potential to enable improved detection and staging of prostate cancer and assessment of response to treatment[66,107–109]. Based on these quantitative measurements, thresholds have been obtained that enable staging of lesions[110] as well as early assessment of response to treatment[111,112] of prostate cancer and its metastases. However, the quantitative reproducibility of rFOV and msEPI relative to ssEPI has not been demonstrated. Consequently, establishing this reproducibility is essential to determine whether previously derived thresholds (obtained from ssEPI studies) can be used with rFOV or msEPI, as well as to ensure data harmonization in multi-site clinical trials (where different sites

may use different diffusion pulse sequences). Although preliminary studies suggest that rFOV and msEPI are able to produce accurate ADC measurements in quantitative diffusion phantoms[113], the reproducibility of quantitative diffusion measurements obtained from these novel diffusion MRI sequences has not been demonstrated.

Furthermore, in-vivo tissue often has restricted diffusion, which induces bias in ADC measurements with different b-value combinations[114,115]. Diffusion kurtosis model has been introduced to measure restricted diffusion[54] independently from b-value choices. Previous studies have examined kurtosis imaging in the prostate[101,109,115]. But similarly, the reproducibility of quantitative diffusion measurements with different b-value combinations and with kurtosis model also need to be evaluated with novel imaging acquisition strategies like rFOV and msEPI.

Therefore, the overall purpose of this study was to evaluate the reproducibility of quantitative diffusion measurements obtained with rFOV and msEPI acquisitions, using ssEPI as a reference. Additionally, the reproducibility across the choice of b-value combination and other acquisition parameters were also evaluated. This paper is aimed to constitute an early-stage technical validation towards further clinical evaluation.

5.2 Methods

To investigate the reproducibility of quantitative diffusion measurements from rFOV and msEPI acquisitions relative to ssEPI, diffusion phantom experiments, prostate imaging in healthy volunteers and prostate imaging in clinical patients were conducted. In addition, different acquisition parameters and quantitative diffusion models were used for further evaluation of reproducibility across these confounding factors. Experimental details are described in the following sections.

5.2.1 Diffusion Phantom Experiments

A National Institute of Standards and Technology (NIST) and RSNA-QIBA diffusion phantom[116], containing multiple vials with different ADC, was used to evaluate three different diffusion sequences across acquisition parameters. The diffusion phantom was scanned using a 3T 60cm bore scanner (MR 750, GE Healthcare, Waukesha, WI). To reduce thermal changes in ADC, the temperature of the phantom was controlled at 0°C using an ice-water bath. The phantom was placed into an eight-channel head coil, with the vials aligned parallel to the magnetic field. Axial ssEPI DW images were acquired with parallel imaging factor = 2 as the reference. rFOV and four-shot msEPI sequences were acquired several times with different imaging parameters. Resolution for different sequence was slightly different based on their image quality. Detailed imaging parameters are provided in **Table 10**.

The acquired diffusion-weighted images were reconstructed for each acquisition (note that multi-shot acquisitions in msEPI were reconstructed using a generalized parallel imaging reconstruction method[51]). ADC maps were then calculated for each acquisition, by fitting a mono-exponential diffusion model to the voxel-wise signal using non-linear least-squares fitting. For each protocol, averaged ADC measurements were performed within an approximately $1cm^2$ region-of-interest (ROI) within each vial. ANCOVA analysis was conducted across different diffusion imaging sequences, using the different phantom vials as the covariate.

5.2.2 Healthy Volunteer Study in the Prostate

Ten healthy volunteers (29±7 years of age) were scanned with a 32-channel receive only Torso coil (GE healthcare, Waukesha, WI) on a 60cm bore 3T scanner (GE healthcare, Waukesha,

WI) to evaluate the image quality, quantitative diffusion reproducibility among the three sequences. The three diffusion imaging sequences were performed as described in **Table 11**. All three diffusion directions are acquired for each sequence. Specifically, ssEPI was conducted with a parallel imaging acceleration factor of two; while msEPI images were acquired with four shots and reconstructed with a generalized parallel imaging technique[51]. Reduction factor of rFOV in the phase encoding direction (R/L) was 40%. Due to the longer acquisition time of multiple shots, msEPI acquisitions were performed with higher spatial resolution than ssEPI and rFOV to achieve similar SNR.

To further evaluate the quantitative measurements across different b-value combinations under restricted diffusion of prostate tissue, two b-value groups, each with seven b-values (**Table 11**), were acquired under the same acquisition parameters. In the high b-value group, b values are from 10 s/mm^2 up to 1500 s/mm^2; whereas the low b-value group has b-value up to 800 s/mm^2. The maximum b-value in each group was chosen based on the clinical protocol for prostate DWI, but more b-values were acquired to obtain more accurate quantitative fitting. Quantitative diffusion maps were calculated using the following two different diffusion models:

1. Mono-exponential diffusion model in **Equation 12**;

2. Kurtosis model:

$$\mathrm{S(b)} = S_0 e^{-bD_k + \frac{1}{6}b^2 {D_k}^2 k}; \tag{28}$$

where S(b) is the signal intensity for a specific b-value, S_0 is the signal intensity at b=0 s/mm^2. ADC and D_k are the diffusion coefficients for the two models, respectively; k is kurtosis.

In addition to the diffusion imaging sequences, a T2-weighted 2D multi-slice Fast Spin Echo (FSE) acquisition with axial slices co-localized with the diffusion imaging slices was acquired. Specific imaging parameters included: FOV=28cmx28cm, slice thickness=5mm, in-

plane spatial resolution=0.875mmx0.786mm, TE=98.4ms, TR=3.4s, echo train length=23, readout bandwidth= 50kHz, acquisition time=3min14s and flip angle=111°. This non-EPI T2-weighted acquisition was used as a reference to assess the geometric distortions present in each of the diffusion imaging sequences. In order to evaluate geometric distortions, the diameter of the prostate in the A/P and R/L directions was measured from axial diffusion-weighted images (ssEPI, rFOV and msEPI). These measurements were compared to those from the non-EPI T2-weighted acquisition, which was used as reference[105]. The distortion present in ssEPI, rFOV and msEPI was compared by analyzing the averaged diameter differences using a one-tail t-test.

To assess the reproducibility of the diffusion measurements for each of the two signal models, pair-wise Bland-Altman analysis[117] was performed across different pulse sequences (rFOV vs. ssEPI and msEPI vs. ssEPI) and different b-value groups (high b-value group vs. low b-value group). Averaged diffusion measurements (ADC and D_k) within an approximately 0.6cm^2 central gland (CG) ROI and an approximately 0.8cm^2 peripheral zone (PZ) ROI were compared for each volunteer in the analysis. ROIs were selected by avoiding distorted regions where ssEPI measurements were used as a reference. The ROIs were co-localized for different imaging sequences.

5.2.3 Patient Study

A prospective IRB-approved HIPAA compliant study was performed and informed consent was obtained. Eligible subjects who were undergoing MRI of the prostate were recruited for additional add-on research sequences. Exclusion criteria included incorrect DWI acquisition parameters.

MRI acquisition/reconstruction:

Imaging was performed with 3.0T MRI (750w or Premier, GE Healthcare, Waukesha, WI). High-resolution, oblique axial T_2-weighted images were obtained (field of view =26 cm^2; in-plane resolution = 0.7 x 1.0 mm; slice thickness = 2.4 mm; echo time = 109.8 ms; repetition time = 3 s) during the clinical prostate MR protocol. Three oblique axial DWI sequences were acquired: 1) 'standard' ssEPI; 2) rFOV; 3) msEPI (acquisition parameters are shown in **Table 12**). Images of msEPI DWI were reconstructed with the phase-corrected multiplexed sensitivity encoding (MUSE) method[9]. ADC maps for each DWI sequence were calculated.

Quantitative distortion assessment:

Whole prostate contouring was completed using the T_2-weighted images and the b=100 s/mm^2 images of all three DWI sequences. Contours from the T_2-weighted images were used as the gold-standard volume and distortion vectors $\vec{d}(slice, \varphi)$ of each slice were calculated by matching the contours of diffusion images (i.e. distorted image volume) to the gold-standard volume[118]. The norm of the distortion vector measures the geometric displacement (mm) induced by distortion over a certain direction (angle φ in polar coordinate system). The final metric $d_{r.m.s.}$ was calculated using the root-mean-square value of the magnitudes of distortion vectors over all angles and slices to quantify the mean -distortion of the entire prostate. The algorithm was implemented in MATLAB R2019a following the method proposed by Gill AB, et al[118].

Quantitative assessment of biopsy correlated lesions:

ROI contouring: Freehand ROI contouring was performed in MATLAB using in-house software for all patients that had a 'target' lesion on MRI that could be colocalized to prostate biopsy results.

This was either (1) patients who received MR-fusion biopsy or (2) patients with a defined lesion on prostate MR who had a recent prostate biopsy with positive results in that sextant or prostate region. A single author (6 years of clinical prostate experience) drew the ROIs on each sequence with reference made to the other ADC maps and DWI series for consistency as well as the multi-planar T_2W-MRI for localization. Subsequently, an identical 'non-cancerous' ROI was placed in a similar region of the contralateral gland that was negative for malignancy on biopsy with an effort made to maintain a similar zonal location (peripheral versus transitional zone) and orientation.

Histogram assessment: Mean, standard deviation, median values, as well as the 20th and 80th percentile of the ADC histograms were calculated and compared among the three acquired sequences.

SNR and CNR assessment: SNR maps and CNR were calculated as follows:

$$SNR = \frac{\hat{S}_{normal}}{\hat{\sigma}_{normal}} \tag{29}$$

and

$$CNR_{PCa} = \frac{\hat{S}_{PCa} - \hat{S}_{normal}}{\hat{\sigma}_{normal}}, \tag{30}$$

where $\hat{S}$ is the estimated signal amplitude and $\hat{\sigma}$ is the estimate of noise standard deviation. Due to the use of parallel imaging, the signal amplitude and noise standard deviation maps were estimated using an iterative Rician expectation-maximization estimator, with spatially varying noise considered[16].

Image quality assessment:

Independent, blinded review of the three DWI series was completed by three board-certified radiologists (X, Y, Z years of clinical prostate MR experience, respectively). Oblique axial T_2-

weighted images and ADC maps were available to readers for reference. Image cropping to an identical small field of view around the prostate maintained the blinded nature of image assessment. For most of the criteria (resolution, capsule demarcation, zonal anatomy, overall image quality, qualitative SNR) the DWI image quality was evaluated on a 5-point Likert scale (1, poor; 2, below average; 3, average; 4, above average; 5, excellent). The image distortion/artifacts were also graded regarding their level and influence. For comparison between DWI acquisitions the scores of all three readers were averaged.

Wilcoxon signed-rank test and Student's t-test were used as appropriate to test for statistical significance (p-value ≤ 0.05 = statistically significant). When appropriate, the tested parameters are reported as mean ± standard error of the mean (SEM).

Table 10. Imaging Protocol in Diffusion Phantom Studies.

	Sequence	FOV (cm^2)	In-plane Resolution (mm^2)	Slice Thickness (mm)	TE(ms)	TR(s)	b-values (s/mm^2)	Average	Diffusion direction
3T scanner	ssEPI	24×24	1.9×1.9	6	86.3	4	50,150,300 500,800,1000	1	All
	msEPI(m1)	24×24	1.25×1.25	6	68.9			1	
	msEPI(m2)	24×24	0.94×0.94	6	70.0			1	
	msEPI(m3)	24×24	1.25×1.25	3	69.6			1	
	rFOV(r1)	24×7.2	1.9×2.25	6	74.1			1	
	rFOV(r2)	24×7.2	1.9×2.25	6	74.1			2	
	rFOV(r3)	24×7.2	1.9×2.25	3	73.4			1	
	rFOV(r4)	24×14.4	1.9×2.88	6	73.9			1	
	rFOV(r5)	24×14.4	1.9×2.88	6	73.9			2	
	rFOV(r6)	24×14.4	1.9×2.88	3	73.1			1	

Table 11. Imaging Protocols in Healthy Volunteer Study.

Healthy volunteer studies							
Sequence	FOV (cm^2)	In-plane Resolution (mm^2)	Slice Thickness/gap (mm)	TE (ms)	TR (s)	b-values * (s/mm^2)	Scan time
ssEPI	26×26	2.0×2.0	4/1	54.2	3	10(4),50(4),100(4),200(4), 400(16),600(16),800(16)	3min 21sec
	26×26	2.0×2.0	4/1	60.7	3	10(2),50(2),100(2),400(8), 800(8),1200(16),1500(16)	3min 57sec
rFOV	26×10.4	2.0×2.0	4/1	49.2	3	10(4),50(4),100(4),200(4), 400(16),600(16),800(16)	3min 21sec
	26×10.4	2.0×2.0	4/1	56.1	3	10(2),50(2),100(2),400(8), 800(8),1200(16),1500(16)	3min 57sec
msEPI	32×32	1.6×1.6	4/1	44.8	3	10(4),50(4),100(4),200(4), 400(16),600(16),800(16)	6min 48sec
	32×32	1.6×1.6	4/1	51.7	3	10(2),50(2),100(2),400(8), 800(8),1200(16),1500(16)	8min 48sec

*Numbers in the brackets are the average numbers of each b-value

Table 12. Imaging Protocols in Patient Evaluation.

Scanner	Coil	Sequence	FOV (cm^2)	Resolution	Parallel Imaging	Partial Fourier	Diffusion Direction	b-values (# Averages)	TE (ms)	TR (s)
GE Premier G_{max}=70mT/m; SR_{max}=200mT/m	32-channel Torso coil	ssEPI	28x28	2mmx2mmx4.8mm	2	75%	All in 1	100(6), 800(12)	55.5	4
		rFOV	28x14		N/A				55.9	
		msEPI	28x28		2				56.0	
GE 750W G_{max}=33mT/m; SR_{max}=120mT/m	Small 30-channel coil	ssEPI	28x28		2			100(6), 800(12)	70.6	
		rFOV	28x14		N/A				65.5	
		msEPI	28x28		2				71.0	

5.3 Results

5.3.1 Diffusion Phantom Experiment

Figure 25 shows representative diffusion-weighted images and ADC maps across three sequences acquired in the diffusion phantom. ssEPI images show distortion (Black arrows) where the vials have a circular cross-section. Both rFOV and msEPI acquisitions reduce the geometric distortion.

Overall, ADC measurements from both rFOV and msEPI are in good agreement ($R^2 > 0.99$) with the reference ssEPI as shown in **Figure 26**. Different slice thickness and resolution does not have a large effect on ADC measurements from either rFOV or msEPI. However, rFOV slightly underestimated ADC with thinner slice and smaller number of averages.

Multivariate analysis of the phantom measurements demonstrates no significant effect ($P>0.05$, effect size $\eta^2 <0.02$) of different sequences ($F=1.868$, $P=0.156$, partial $\eta^2 =0.008$), even with different acquisition parameters.

5.3.2 Healthy Volunteer Study in the Prostate

Diffusion-weighted images and ADC maps of the prostate of a healthy young volunteer are presented in **Figure 27**. Distortions within the prostate are improved in rFOV and msEPI (white arrows). Note that rFOV depicts only a limited FOV with lower SNR. The quantified image distortion for each pulse sequence is shown in **Figure 28**. Mean values and standard deviations of the diameter differences relative to the non-EPI T2-weighted imaging reference in R/L and A/P

directions are plotted. P-values from the t-test are shown adjacent to each bar. Significantly lower distortion ($P<0.05$) in the A/P direction is demonstrated for both rFOV and msEPI.

Quantitative diffusion measurements of peripheral zone (PZ) and central gland (CG) with each combination of sequence, b-value group and diffusion model are listed in **Table 12**(a). **Table 13** shows the Bland-Altman analysis of volunteer data across the three pulse sequences (a) and different b-value groups (b) with both mono-exponential model and kurtosis model. According to the bias results, no significant difference ($p>0.05$) has been shown across sequences, even though the in-plane resolution is different for msEPI; but significant bias of ADC estimations exists across b-value groups ($p<0.01$). From the width of the 95% confidence interval ($\pm 1.96\sigma$, where σ is the standard deviation of the difference between the quantitative measurements from different sequences), both rFOV and msEPI have moderate confidence intervals ($1.96\sigma < 0.3\times10^{-6}$ mm^2/s) relative to ssEPI ADC measurements from a mono-exponential model. However, the confidence intervals for both rFOV and msEPI relative to ssEPI are larger for the parameter D_k measured from the diffusion kurtosis model.

5.3.3 Patient Study

Thirty patients were recruited initially recruited. Five patients were excluded due to incorrect DWI acquisition parameters resulting in a final study group of 25 male patients. The average age was 63.9 years (range, 44-76 years) and average pre-scan PSA was 6.55 ng/mL (range, 1.13-10.84 ng/mL). The study group included 9 patients with biopsy proven prostate cancer, 4 patients currently in active surveillance, 6 patients without biopsy proven cancer but persistently elevated PSA, and one patient with biochemical recurrence after high intensity focused ultrasound treatment.

Additionally, 15 patients had biopsy proven prostate cancer that correlated with a suspicious lesion on MRI (n=7, MR fusion biopsy; n=8, correlative sextant biopsy result completed without MR fusion).

Quantitative distortion:

There was a small but statistically significant reduction in the average calculated $d_{r.m.s.}$ for rFOV compared to ssEPI (3.22±0.22 versus 3.40±0.25, respectively; p=0.033). A similar reduction was also seen when msEPI was compared to ssEPI (2.98±0.22 versus 3.40±0.25, respectively; p=0.003). The difference between rFOV and msEPI was not statistically significant (p=0.078). The graphical representation of this change is illustrated for an example patient in **Figure 29**.

Quantitative ADC results:

There was no significant difference across the 3 DWI acquisitions regarding histogram parameters for the cancerous ROIs (**Table 15**), including mean, standard deviation, 20^{th} percentile, median, or 80^{th} percentile. Conversely, the statistically significant decrease in average mean ADC was seen in the cancerous ROIs, compared to the corresponding non-cancerous tissue, for all three DWI sequences (**Figure 30**). There was a statistically significant reduction in the average non-cancerous mean ADC for rFOV compared to msEPI, 1511 x 10^{-6} mm^2/s versus 1619 x 10^{-6} mm^2/s, respectively ($p<0.05$).

Image quality results:

The multi-reader qualitative assessment of image quality, DWI artifacts, and distortion is detailed in **Table 16**. In particular, msEPI demonstrated significantly greater scores for overall image quality, influence of distortion/artifacts, and prostate zonal anatomy compared to both ssEPI and rFOV. The msEPI series also demonstrated significantly greater level of distortion/artifact scores, compared to ssEPI, and qualitative SNR scores, compared to rFOV.

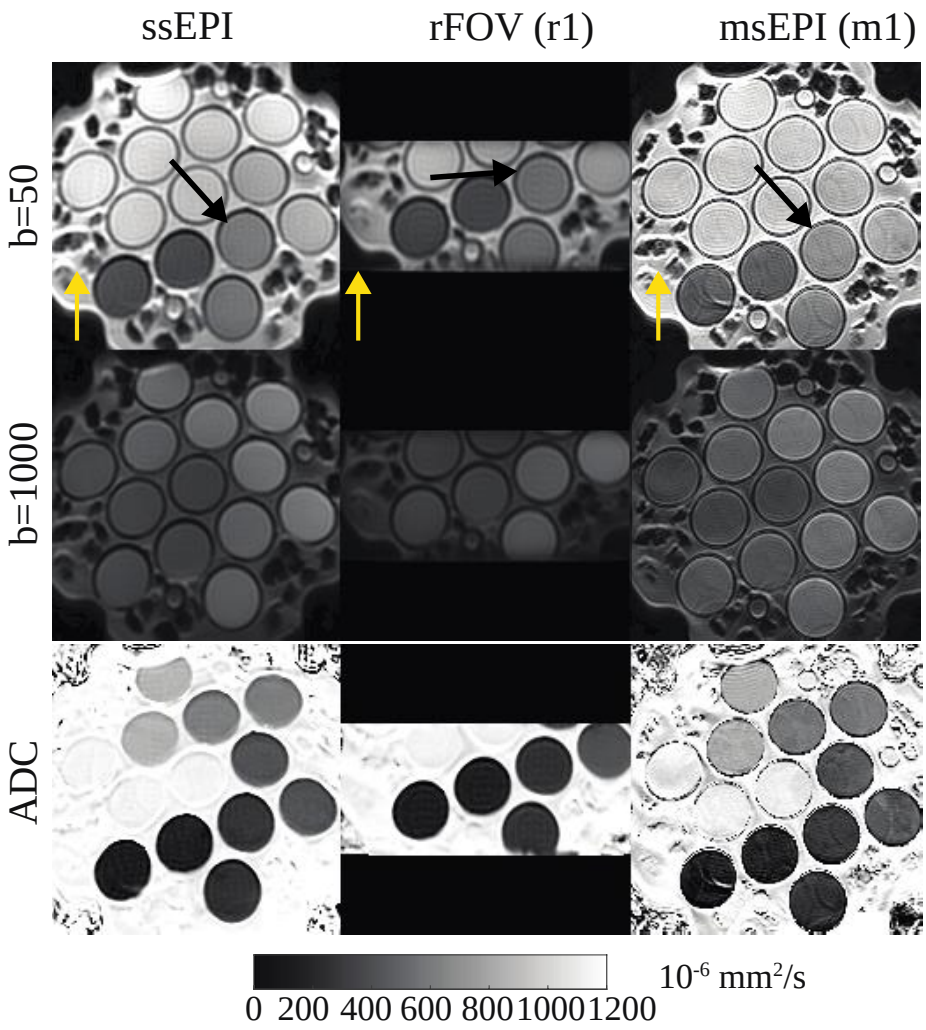

Figure 25. Diffusion Phantom Results. Representative diffusion-weighted images and ADC maps across three sequences on a diffusion phantom. Black arrows indicate an area with distortions in ssEPI images. Yellow arrows for each sequence represent the phase encoding direction.

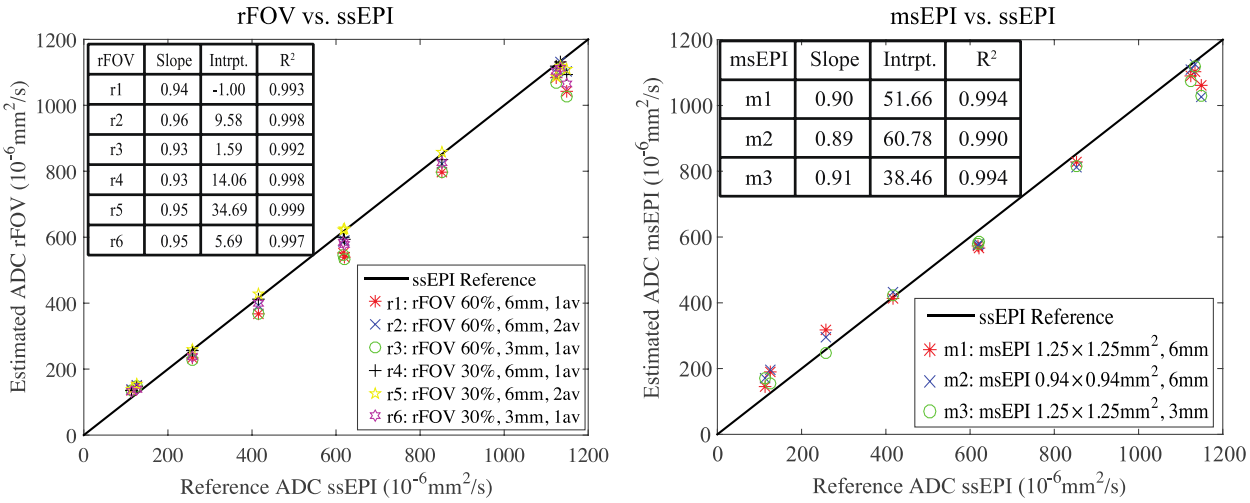

Figure 26. Linear regression analysis on phantom measurements. Comparison between the averaged estimated ADC values from rFOV and msEPI and the reference ADC values from ssEPI within different vials of the diffusion phantom.

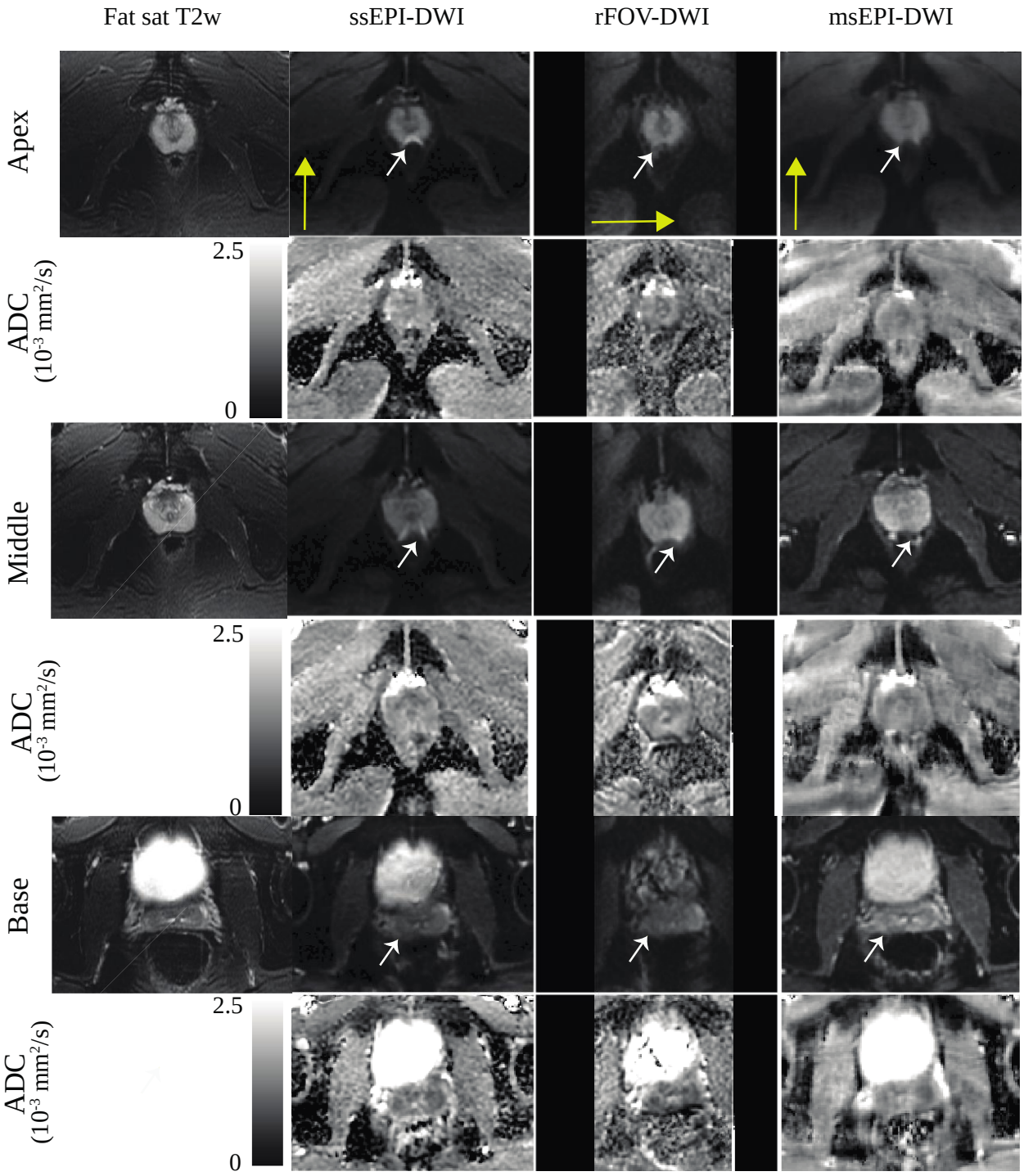

Figure 27. Healthy Prostate Volunteer Examples. Representative diffusion-weighted images and ADC maps across three sequences of a healthy volunteer. Three different slices from the apex, middle and base plane of the prostate respectively are shown with corresponding T2-weighted FSE images for illustration of the distortion. White arrows indicate an area with distortions in ssEPI images. Yellow arrows for each sequence represent the phase encoding direction.

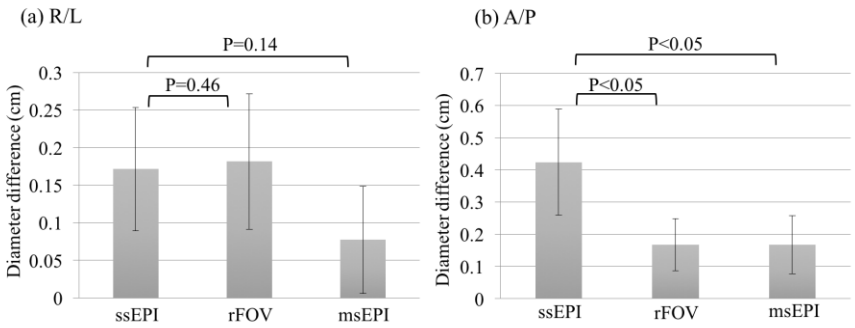

Figure 28. Diameter Differences in R/L and A/P directions. Diameter differences in R/L and A/P directions between diffusion-weighted images from different sequences and an axial, non-EPI, T2-weighted acquisition (used as the reference). These diameter differences are evaluated as a measure of image distortion for each diffusion pulse sequence. P-values from t-test are shown for rFOV and msEPI compared to ssEPI, respectively.

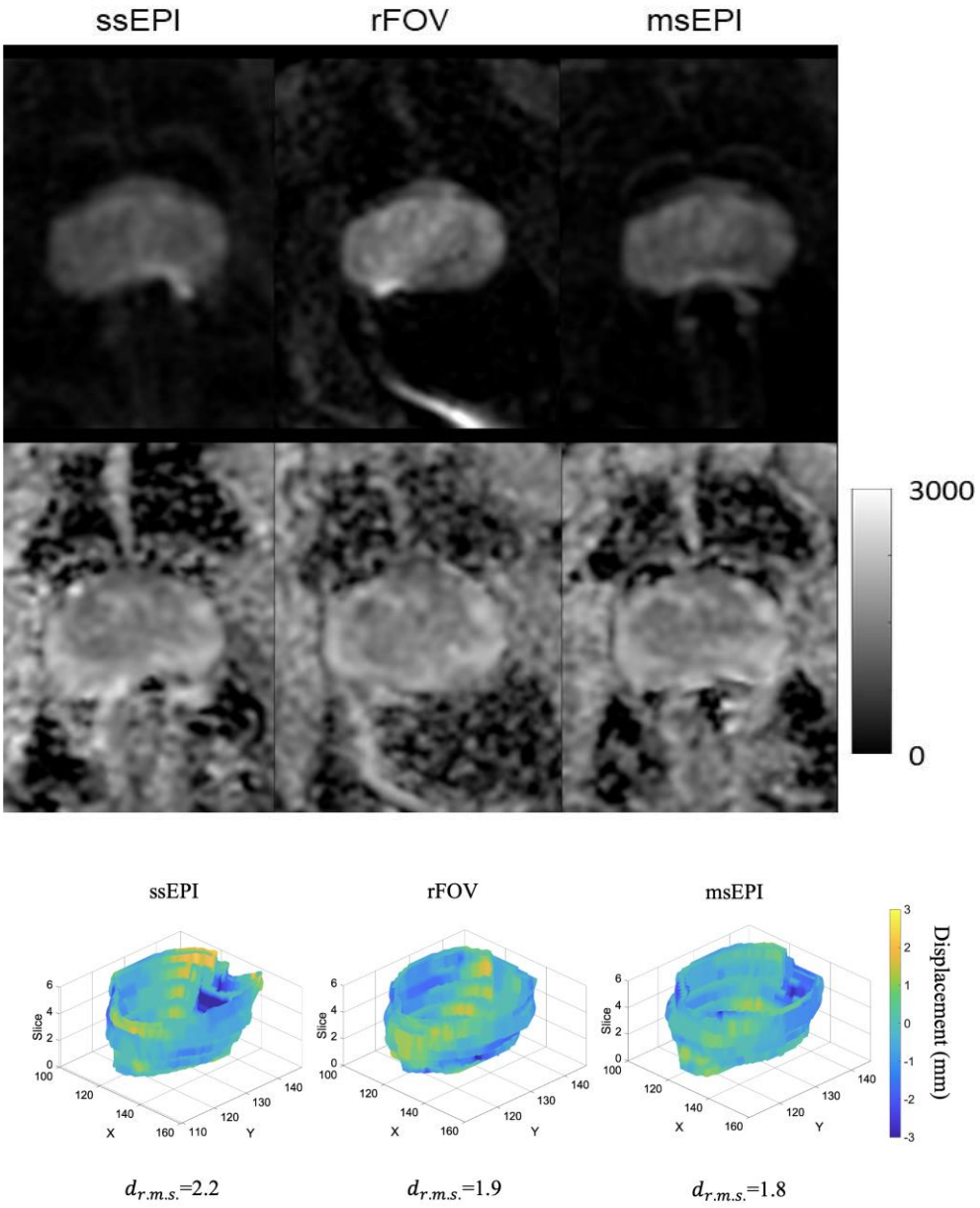

Figure 29. Example patient images and quantitative distortion map. Illustrative example detailing the reduction in diffusion-weighted imaging prostate distortion using the rFOV and msEPI techniques compared to the 'standard' ssEPI. A. Central slice of the high b-value DWI acquisition (top) and corresponding ADC map (bottom) for ssEPI, rFOV, and msEPI sequences (L-R, respectively). On the ssEPI images, rectal gas results in artifactual signal build-up (white arrow) and contour distortion (dashed arrow) of the posterior prostate. The artifact and distortion is reduced in both the rFOV and, to a greater extent, msEPI images. B. (L-R) The 3D distortion plots for the ssEPI, rFOV, and msEPI acquisitions from the same patient are displayed with slice number on the z-axis and pixel location in the x/y plane. Each pixel within the prostate region of interest is colored according to the magnitude of positive or negative displacement (see color bar) and the $d_{r.m.s.}$ is displayed under the plot for each acquisition. A small reduction in distortion for both rFOV and msEPI compared to ssEPI can be seen graphically, through the overall reduction

in regions with higher magnitude displacement, as well as in the reduction in $d_{r.m.s.}$ for rFOV and msEPI.

Table 13. Diffusion Measurements of Healthy Volunteer Studies.

(a) Diffusion measurements of healthy volunteers

Sequence	b-values group	Mono-exponential ADC×10^{-3} (mm^2/s)		Kurtosis D_k×10^{-3} (mm^2/s)		Kurtosis k	
		CG	PZ	CG	PZ	CG	PZ
ssEPI	Low	1.34±0.09	1.38±0.26	1.57±0.17	1.64±0.24	0.79±0.24	0.92±0.30
	High	1.24±0.09	1.29±0.27	1.59±0.17	1.68±0.31	0.76±0.10	0.81±0.16
rFOV	Low	1.33±0.09	1.39±0.15	1.59±0.18	1.67±0.22	0.86±0.36	0.85±0.37
	High	1.20±0.10	1.29±0.25	1.59±0.15	1.74±0.25	0.84±0.11	0.87±0.19
msEPI	Low	1.32±0.14	1.33±0.21	1.62±0.22	1.59±0.29	0.98±0.42	0.86±0.43
	High	1.23±0.14	1.24±0.22	1.53±0.23	1.57±0.24	0.70±0.15	0.76±0.12

Table 14. Bland-Altman Analysis of Healthy Volunteer Studies.

(a) Bland-Altman analysis across pulse sequences (Bias [95% confidence interval])

Models	Quantity	b-values group	rFOV vs. ssEPI Bias±1.96SD	p	msEPI vs. ssEPI Bias±1.96SD	p
Mono-exponential	ADC×10^{-3} (mm^2/s)	Low b-values	0.00 [-0.21, 0.22]	0.86	-0.03 [-0.22, 0.15]	0.12
		High b-values	-0.02 [-0.21, 0.18]	0.45	-0.03 [-0.28, 0.22]	0.30
Kurtosis	D_k×10^{-3} (mm^2/s)	Low b-values	0.03 [-0.39, 0.44]	0.60	0.00 [-0.36, 0.37]	0.95
		High b-values	0.03 [-0.29, 0.35]	0.49	-0.09 [-0.58, 0.40]	0.13

(b) Bland-Altman analysis across b-value groups (Bias [95% confidence interval])

Models	Quantity	ssEPI Low vs. High b-values Bias±1.96SD	p	rFOV Low vs. High b-values Bias±1.96SD	p	msEPI Low vs. High b-values Bias±1.96SD	p
Mono-exponential	ADC×10^{-3} (mm^2/s)	-0.09 [-0.26, 0.08]	0.00	-0.11 [0.33, 0.10]	0.00	-0.09 [-0.25, 0.07]	0.01
Kurtosis	D_k×10^{-3} (mm^2/s)	0.03 [-0.32, 0.38]	0.43	0.03 [-0.35, 0.42]	0.46	-0.06 [-0.40, 0.29]	0.16

* Low b-values group is b = [10, 50, 100, 200, 400, 600, 800] s/mm^2;
High b-values group is b = [10, 50, 100, 400, 800, 1200, 1500] s/mm^2.

5.4 Discussion

As an initial step towards further clinical studies, this study evaluated the reproducibility of quantitative diffusion measurements across different pulse sequences (ssEPI, rFOV and msEPI) in phantoms and prostate of healthy volunteers and clinical patients. From our results, quantitative diffusion measurements obtained from recently developed reduced-distortion pulse sequences (rFOV and msEPI) were in good agreement with the standard ssEPI-based measurements. In combination with the reduced distortion provided by these novel pulse sequences (as has been demonstrated in previous works[101–106,119] as well as in this study), these results demonstrate the potential of rFOV and msEPI, at the cost of FOV size or scan time, to provide reproducible quantitative diffusion measurements compared to ssEPI. This potential may have significant research and clinical implications for diffusion MRI of the prostate.

rFOV is able to reduce distortion in diffusion-weighted images through limiting the size of the FOV. In this work, both phantom experiments and volunteer studies have shown no significant difference ($p>0.05$) in quantitative diffusion measurements between rFOV and ssEPI. This agrees with the conclusions from other evaluation studies. However, it has been demonstrated that rFOV images tend to have lower SNR especially when the average number is small and b-value is high. This property will induce an underestimation in quantitative diffusion measurements, which can be fixed by using larger number of averages and choosing optimal b-values. In this work, it is shown from both phantom and patient studies that diffusion measurements of rFOV with larger number of averages have less bias than those with small number of averages.

msEPI has the capability for high resolution diffusion-weighted images with less distortion than ssEPI and without sacrificing scan coverage by reducing the FOV[104]. Overall, ADC measurements from msEPI have no significant difference from ssEPI and rFOV based on both

multivariate analysis of the phantom data and Bland-Altman analysis of volunteer studies shown in the results section. In principle, residual parallel imaging artifacts from the current implementation of msEPI reconstruction may increase the variability of msEPI-derived quantitative measurements, however no systematic bias was observed relative to ssEPI measurements.

Additionally, for all the three sequences, the choice of b-values and diffusion models will affect the quantitative diffusion measurements[109,114]. Previous studies have demonstrated significant difference of diffusion measurements between different combinations of b-values in both healthy and cancerous prostate tissues[114]. This difference may be induced by several causes, including the presence of perfusion or pseudo-diffusion effects at low b-values, as well as restricted diffusion and potentially noise floor effects at high b-values[120,121]. In this work, significant difference of ADC estimation between high b-values group and low b-values group has been shown in the healthy volunteer study ($p<0.05$ for all three sequences). On the contrary, there is no significant difference between two b-value groups in corrected diffusion coefficients from kurtosis model, with $p>0.1$ for all the three pulse sequences. This distinct behavior of the mono-exponential and kurtosis models may be due to the different effects of restricted diffusion or noise floor effects in the two diffusion models.

In addition to demonstrating reproducibility across pulse sequences, the quantitative diffusion measurements obtained in this study are in good agreement with previous works. In healthy young volunteers, ADC measurements with low b-value group ssEPI are $1.34\pm0.09\times10^{-3}$ mm^2/s in CG and $1.38\pm0.26\times10^{-3}$ mm^2/s in PZ. This agrees with the results from a previous prostate imaging study in young healthy subjects[65], where the ADC values are 1.22 (0.95-1.74) $\times10^{-3}$ mm^2/s in CG and 1.30 (1.21-2.08) $\times10^{-3}$ mm^2/s in PZ. In the patients, ADC values measured

from ssEPI within CG (BPH not excluded) and healthy PZ were $1.29\pm0.17\times10^{-3}$ mm^2/s and $1.74\pm0.23\times10^{-3}$ mm^2/s, respectively. The results are in good agreement with previous measurements[66,107].

Overall, novel pulse sequences like rFOV and msEPI have been shown to be good alternatives to ssEPI for high quality diffusion-weighted images with less distortion. Also, they are both promising techniques for reproducible quantitative diffusion measurements compared to ssEPI and reproducible measurements across different acquisition parameters. However, rFOV and msEPI have different characteristics in terms of FOV, SNR and acquisition time. Therefore, in practice, the choice between rFOV and msEPI may be driven by the desired FOV, resolution and possible scan time constraints.

This study had several important limitations. In this work, rFOV and msEPI measurements are compared to ssEPI because there is no available gold standard reference for ADC in tissues (particularly in the presence of restricted diffusion). Further, an important motivation of this work was to assess whether previously derived quantitative criteria (e.g., relevant ADC thresholds derived using ssEPI[100,111,122]) can potentially be applicable to ADC measurements obtained using rFOV or msEPI. In addition, we optimized each sequence for performance, hence different spatial resolutions and readout directions were used for different pulse sequences. The different spatial resolutions may have effects on the visualization of edges or lesion in DWI, but it does not affect the ADC measurements as shown in the phantom results. Most importantly, only healthy tissues in the clinical patients were evaluated in the statistical analysis of this study. Based on the promising preliminary data provided by this study in phantoms, healthy volunteers, and healthy tissues in patients, future clinical studies are needed to evaluate the ability of rFOV and msEPI to assess prostate cancer. Additionally, future studies will be needed to assess the reproducibility of

diffusion measurements from rFOV and ssEPI at different field strengths, different coils, and using scanners from different vendors.

5.5 Conclusion

In conclusion, quantitative diffusion measurements demonstrate good reproducibility across diffusion MRI pulse sequences. Measurements from two novel sequences (rFOV and msEPI) with reduced image distortion are in good agreement with a standard ssEPI sequence. Therefore, both rFOV and msEPI have the potential to provide high image quality with reproducible quantitative diffusion measurements in prostate diffusion MRI.

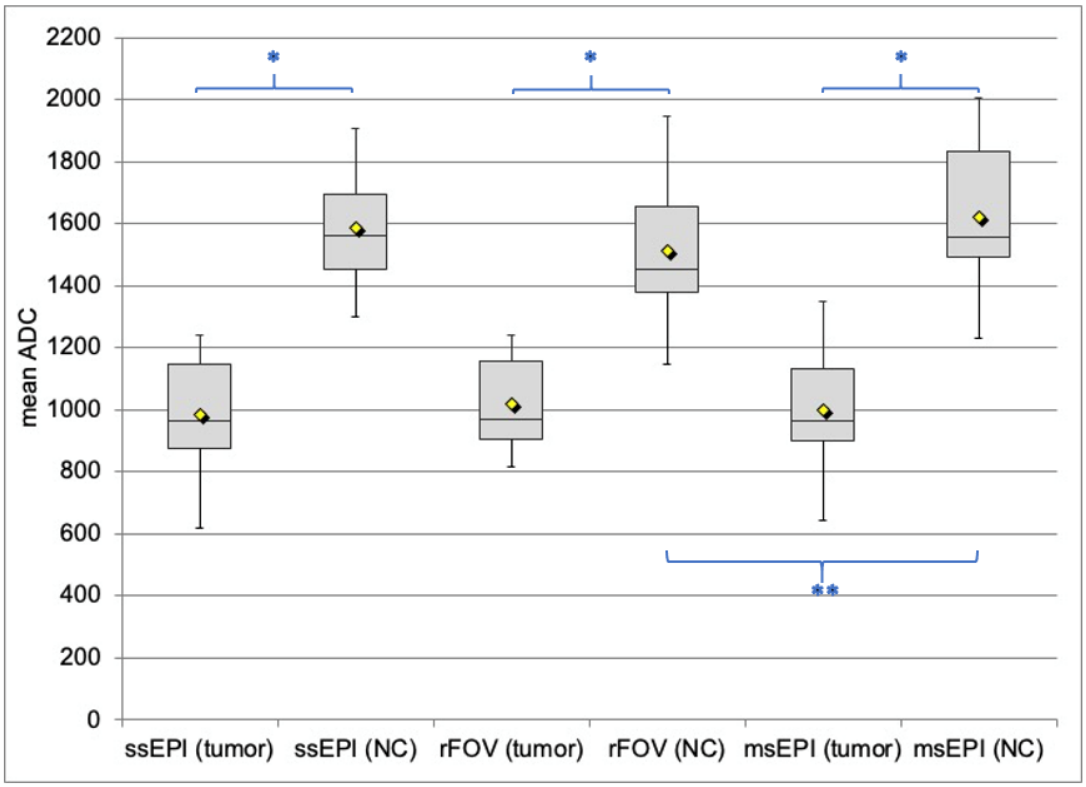

*Statistically significant difference between tumor and non-cancerous for each DWI sequence ($p<0.0001$)
**Statistically significant difference between non-cancerous values for rFOV compared to msEPI ($p<0.01$)

Figure 30. Boxplots for mean ADC from tumor and non-cancerous ROIs.

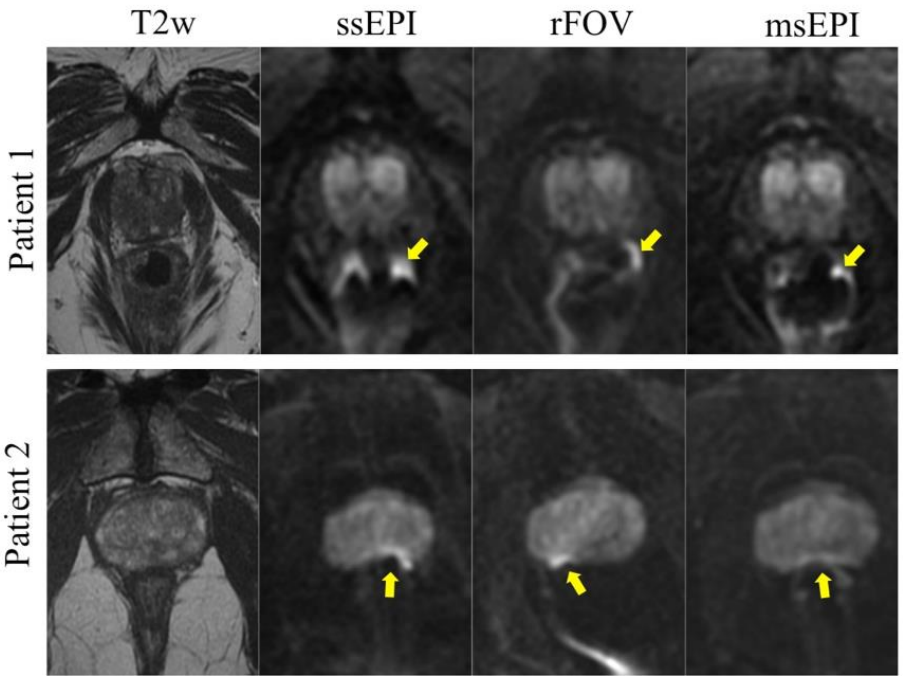

Figure 31. Representative images from two patients. Representative images from two patients demonstrating reduced artifactual distortion on DWI with of rFOV and msEPI compared to ssEPI. The qualitative improvement in distortion is greatest for msEPI in both patients which results in reduced signal buildup due to rectal gas and less anterior-posterior distortion of the prostate shape. (ssEPI, single shot echo planar image; rFOV, reduced field of view; msEPI, multi-shot echo planar image).

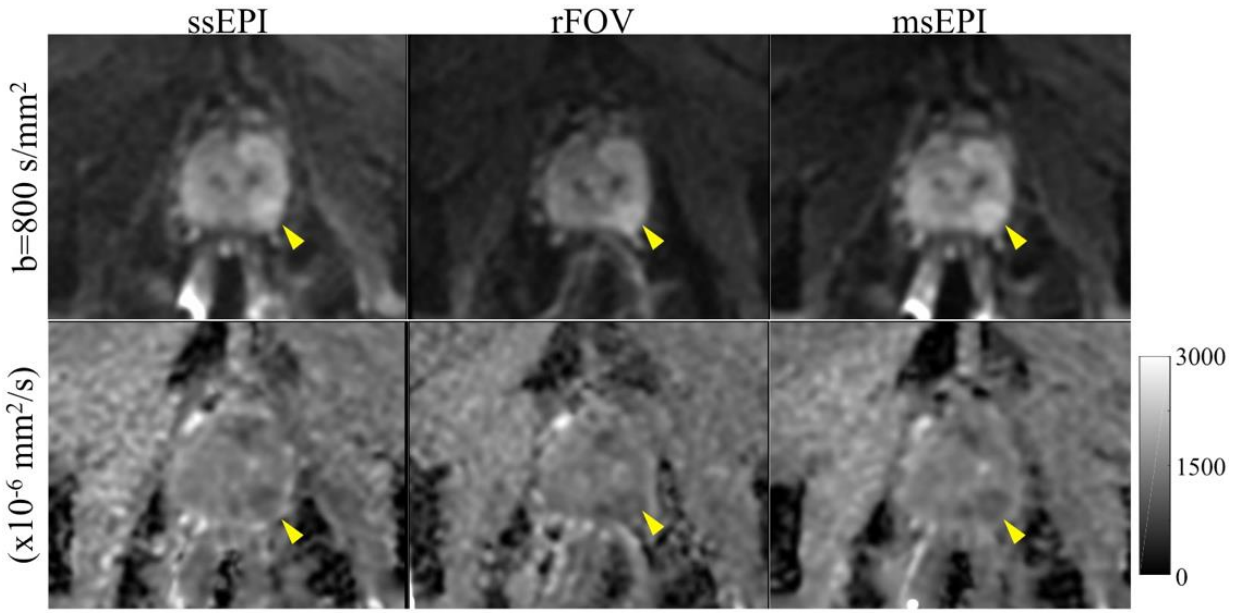

Figure 32. Example patient images with PCa. 60-year old male with elevated prostate specific antigen (4.46 ng/mL) and suspicious lesion on prostate MRI. The suspicious lesion (yellow arrows) in the left peripheral zone is identified on all three DWI sequences, including the b=800 series (top row) and calculated ADC map (bottom row). The mean ADC value for the lesion was 1075.8, 1098.8, and 1067.5 $x10^{-6}$ mm^2/s on ssEPI, rFOV, and msEPI, respectively. The patient subsequently underwent radical prostatectomy and was found to have Gleason 3+4 disease.

Table 15. Histogram parameters for cancerous ROIs.

ADC parameters ($x10^{-6}$ mm^2/s)	**ssEPI**	**rFOV**	**msEPI**
Standard deviation	138.1 ± 33.2	139.8 ± 30.2	156.8 ± 45.4
Mean	985.1 ± 178	1019 ± 144	997.4 ± 186
20^{th} percentile	859.0 ± 180	889.9 ± 137	856.7 ± 205
Median	975.2 ± 172	995.7 ± 144	992.3 ± 184.1
80^{th} percentile	1099 ± 178	1139 ± 158	1133 ± 182
Data are mean ± standard deviation ADC, apparent diffusion coefficient			

Table 16. Multi-reader qualitative assessment of image quality, DWI artifacts and distortion.

	All Readers		
	ssEPI	**rFOV**	**msEPI**
Resolution	3.24 ± 0.29	3.35 ± 0.31	3.47 ± 0.37
Capsule demarcation	2.91 ± 0.51	3.10 ± 0.44*	3.17 ± 0.46*
Zonal anatomy	2.46 ± 0.52	2.52 ± 0.56	2.78 ± 0.55**[t]
Qualitative SNR	3.41 ± 0.32	3.39 ± 0.28	3.57 ± 0.39[t]
Overall Image Quality	2.90 ± 0.59	3.03 ± 0.46	3.28 ± 0.57**[t]
Level of Distortion/Artifacts	3.04 ± 0.68	3.16 ± 0.70	3.35 ± 0.66*
Influence of Distortion/Artifacts	3.13 ± 0.80	3.23 ± 0.74	3.52 ± 0.64**[t]

* p-value < 0.05 between rFOV or msEPI and ssEPI
** p-value < 0.01 between rFOV or msEPI and ssEPI
[t] p-value < 0.05 between msEPI and rFOV

Chapter

6. Multi-Shot M1-Optimized Diffusion Imaging with Deep Learning Reconstruction for Motion-Robust, Distortion-Reduced, and SNR-Enhanced DW-MRI of the Liver

6.1 Introduction

Diffusion-weighted (DW)-MRI of the liver has various potential applications, including the detection, staging, and treatment monitoring of cancer[5,13,94,112,123–126], as well as the assessment of diffuse liver disease[94] (e.g. liver fibrosis). Apparent Diffusion Coefficient (ADC) is the mostly commonly used quantitative diffusion measurement to serve as a potential biomarker of cancer[5,80]. Other quantitative diffusion models including Diffusion Tensor Imaging (DTI)[13,94] and Intravoxel Incoherent Motion (IVIM)[127,128] have also been widely evaluated in the assessment of diffusion liver disease, hepatocellular carcinoma and liver metastases.

In the past decades, efforts have been made to improve the clinical accuracy and reproducibility of DW-MRI and ADC measurements[129,130]. However, DW-MRI in the liver is still complicated by the presence of substantial technical challenges[3,4,44], especially in the following aspects:

1) Signal voids in tissues, especially the left lobe of liver, that experience non-rigid motion (i.e. cardiac motion and cardiovascular pulsation) during the application of DW gradients. These signal voids complicate diagnostic image interpretation and introduce bias in quantitative measures of diffusion (e.g. ADC).

2) Unpredictable phase variations in the signal acquired from each excitation, which result in the widespread use of single shot echo-planar imaging (ssEPI) in DW-MRI. Unfortunately, ssEPI results in substantial image distortions and limited resolution in DW-MRI, particularly in complex magnetic susceptibility environments such as the abdomen.

3) Low Signal-to-Noise Ratio (SNR) in the liver due to the short T2 relaxation[64]. A typical DW-MRI sequence with a b-value at 500s/mm^2 has an echo time (TE) around 50ms while the T2 value of liver in healthy people shorter than 40ms. This short T2 relaxation and thus substantial SNR loss will limit the ability to reach higher b-value in liver DW-MRI and cause high uncertainty in quantitative measurements. It may also complicate the detection of small lesions.

To address the challenges from physiological motion and image distortion, advanced techniques have been proposed in the recent years. Optimized motion-robust DW gradients techniques[45,46,131] have shown excellent promise to overcome the signal voids present in tissues that experience substantial motion, leading to reliable imaging and quantitative ADC mapping throughout the entire liver. In addition, phase-corrected multi-shot reconstruction techniques[51] has been proposed for reduced-distortion, high-resolution multi-shot EPI (msEPI) based DW-MRI,

which has been proved effective in multiple applications[132–135]. However, the potential synergy between the optimized motion-robust DW gradients and msEPI technique has not been investigated. The reconstruction of msEPI is challenging because the phase inconsistency between shots, which is even more difficult in the liver due to the existence of phase variation from cardiac motion. With the motion-robust DW gradients, the unpredictable phase variations between multiple shots can be largely mitigated. This phase consistency between shots has the potential to provide a better reconstruction result.

Nonetheless, SNR is still a challenging issue for liver DW-MRI. Particularly, when motion-robust DW gradients are used, the TE, though minimized, will still be significantly longer than traditional monopolar diffusion gradients. Fortunately, in recent years, Deep-Learning (DL) based methods have demonstrated outstanding potential for denoising of low-SNR data[136–138]. Application of DL-based reconstruction and denoising in liver DW-MRI has not been fully evaluated.

In this study, we hypothesize that a synergistic combination may be feasible between motion-robust DW gradient waveforms, msEPI techniques, and DL denoising for liver DW-MRI. The feasibility, robustness and reproducibility will be tested and evaluated in a quantitative motion phantom, and healthy liver volunteers.

6.2 Methods

6.2.1 Anthropomorphic Liver Phantom Validation

An anthropomorphic, in vitro model of the liver was constructed using a hybrid additive manufacturing process. The liver was segmented from a computed tomographic dataset of a healthy adult and used to generate a STL model. The STL was imported to 3MATIC (Materialise NV, Leuven, Belgium) where it was used to generate both halves of a hallow-core liver mold, which was 3D printed using stereolithography printer (SLA; Formlabs, Somerville, MA) to ensure it was watertight. Space was removed in order to leave room for a bifurcation representing an idealized portal vein that could be placed near its anatomical location in the liver. The bifurcation was 3D printed using water-soluble polyvinyl alcohol (PVA) and coated with latex. After the latex cured, the PVA core was dissolved leaving a hallow vessel of distensible latex, which could be hooked up to a pulsatile flow pump. The pseudo-tissue liver was constructed using a hydrogel material base solution by dissolving two polymer components -acrylamide and bis-acrylamide (Fisher Scientific, Hampton, NH, USA)- into de-ionized water with a gel composition of 8% to provide desired stiffness. Cross-linking of the gel was initiated by the addition of Tetramethylethylenediamine (TEMED) and ammonium persulfate (Fisher Scientific, Hampton, NH, USA). After the two halves of the mold were secured together using RTV silicone sealant with the bifurcation in place, the hydrogel solution was poured into the mold and allowed to cure over 24 hours, producing a fully distensible liver around the bifurcation tube.

After the phantom is manufactured, it was scanned on a 3T scanner (GE Signal Premier) with high density receive array coils (AIR coil, GE Healthcare, Waukesha, WI). The phantom was

set up on the patient table while connected to a water pump in the control room. The pump is controlled by a computer program where the amplitude and period of flow pulses can be designed and implemented. The design and phantom setup are shown in **Figure 33**.

The average flow amplitudes were set as 0 L/min, 0.15 L/min and 0.6 L/min, respectively. For each flow setup, five diffusion series were acquired, including MONO-ssEPI, ODGD-ssEPI, MODI-ssEPI, MONO-msEPI and MODI-msEPI. A T2-weighted FSE sequence was acquired at 0 L/min as the anatomical reference.

6.2.2 Healthy Volunteer Experiments

After IRB approval and informed written consent, eight healthy volunteers were scanned on a 3T scanner (GE Signa Premier) with high density receive array coils (AIR coil, GE Healthcare, Waukesha, WI).

In comparison to the conventional MONO gradient waveform, MODI gradient waveform design was applied to achieve motion-robust diffusion waveforms with a small first-moment to suppress blood signal. For each DW waveform (MONO and MODI), two separate DW-MRI acquisitions using ssEPI and msEPI, respectively, were obtained. Detailed acquisition parameters are in **Table 17**. msEPI was obtained with two shots and each shot had acceleration factor =2. DW-MRI acquisitions were performed during multiple breath-holding periods at the end of expiration.

Non-EPI T2-weighted (T2w) images were acquired with a 2D Fast Spin-Echo sequence as a reference of anatomic structure. The same spatial resolution and prescribed locations were used to match the DW-MRI acquisitions.

Table 17. Image acquisition parameters of healthy volunteer experiment.

Readout	Diffusion waveform	FOV (cm^2)	Resolution (mm^2)	Slice Coverage	Acceleration factor	Partial Fourier factor	Diffusion direction	b-values (# averages)	TE (ms)	TR (s)	Inversion Time (s)	Scan time per breath-hold/ #breat-hholds
ssEPI	MONO	36x36	2.8x2.8	6mm x 20 slices	2	75%	A/P	[50(2), 500(4)] s/mm^2	44.3	5	99	20s / 2
	MODI								66.1	5		20s / 2
msEPI	MONO					100%			44.6	3.6	75	22s / 3
	MODI								66.3	3.6		22s / 3

6.2.3 Image Reconstruction

For both MONO and MODI acquisitions, ssEPI data were reconstructed with traditional parallel imaging and partial Fourier technique and msEPI data were reconstructed with a multiplexed sensitivity-encoding method[51].

For the healthy volunteer data, though, the diffusion raw data from MODI acquisition was then reconstructed in two ways, first using the standard echo planar reconstruction and second using a DL Recon algorithm based on a Convolutional Neural Network (CNN)[136] trained to optimize SNR. For this second series, images were reconstructed with a tunable noise reduction factor set to 75%.

6.2.4 Data Analysis

ADC measurements

ADC maps were calculated for all DW-MRI series. Co-localized ROIs were drawn on each ADC map in both the left and right liver lobes. The ADC in the non-motion-corrupted right liver lobe was used as reference ADC value[45,46,131]. Bland-Altman analysis was performed between the ADC measurements of the left and right lobe for each diffusion sequence to evaluate the consistency of ADC between left and right lobes.

Distortion Level

Distortion level was assessed using the normalized cross-correlation coefficient (CCC)[139], which quantifies the geometric alignment between the T2w reference and the low b-value DW images for each slice (**Equation 31**). Masks were selected from T2w references to remove the

background noises. The CCC measurements were compared between ssEPI and msEPI images for both MONO and MODI waveforms.

$$CCC = \frac{\sum_i \sum_j (T2_{ij} - \overline{T2})(DWI_{ij} - \overline{DWI})}{\sqrt{(\sum_i \sum_j (T2_{ij} - \overline{T2})^2)(\sum_i \sum_j (DWI_{ij} - \bar{DWI})^2)}} \quad (31)$$

Evaluation of ADC SNR

As a surrogate measure of SNR, the standard deviation of ADC within each of the ROIs described above was also measured in the healthy volunteer data for MONO, MODI, and MODI-DL series.

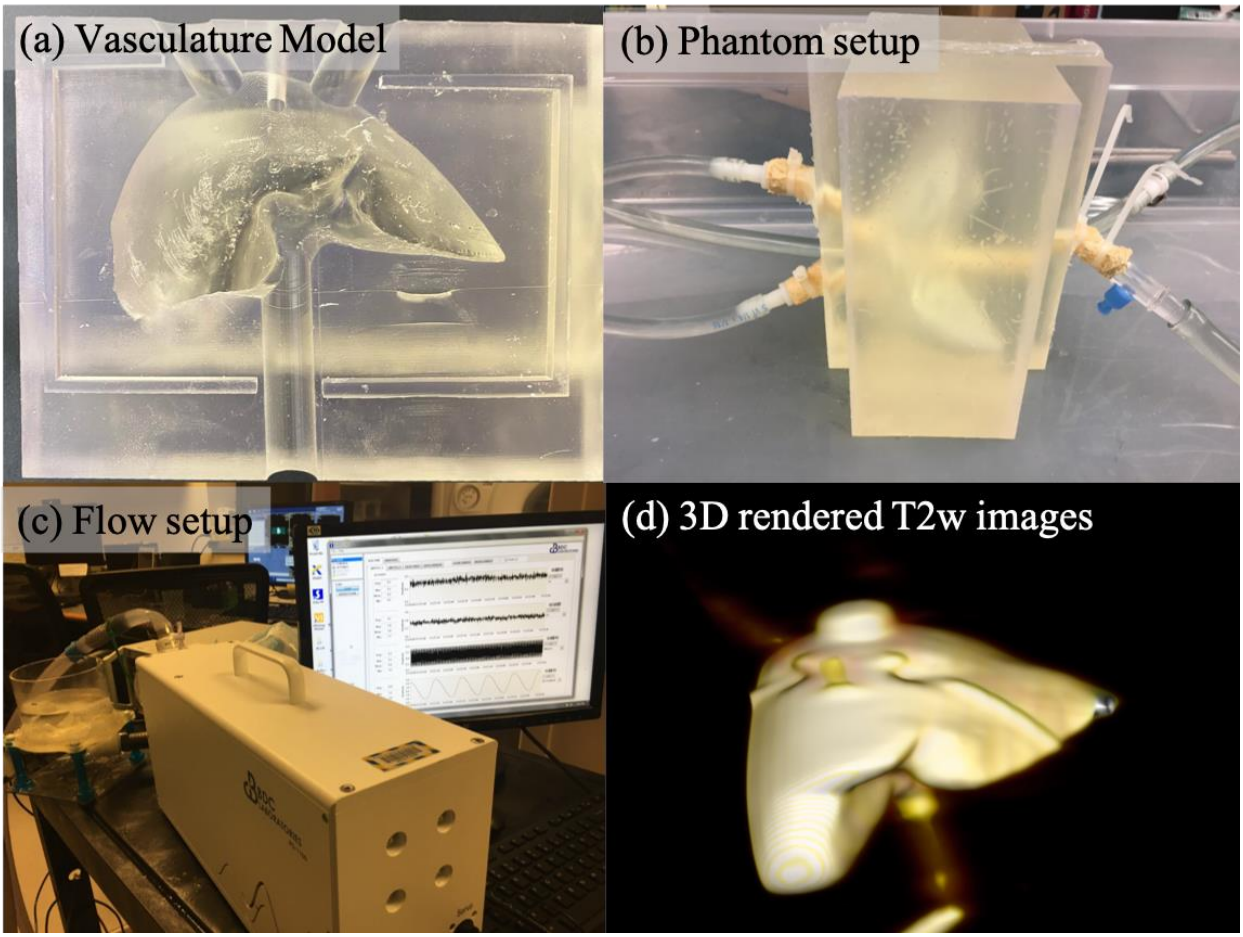

Figure 33. Design and setup of the anthropomorphic liver motion phantom. Flow chart A vasculature liver model was designed and made with hydrogel. Water is pumped from the control room into the scanner room to induce periodic pulsatile motion to the elastic hydrogel. The periodic flow is programmable and controllable by users to adjust the flow amplitude and period.

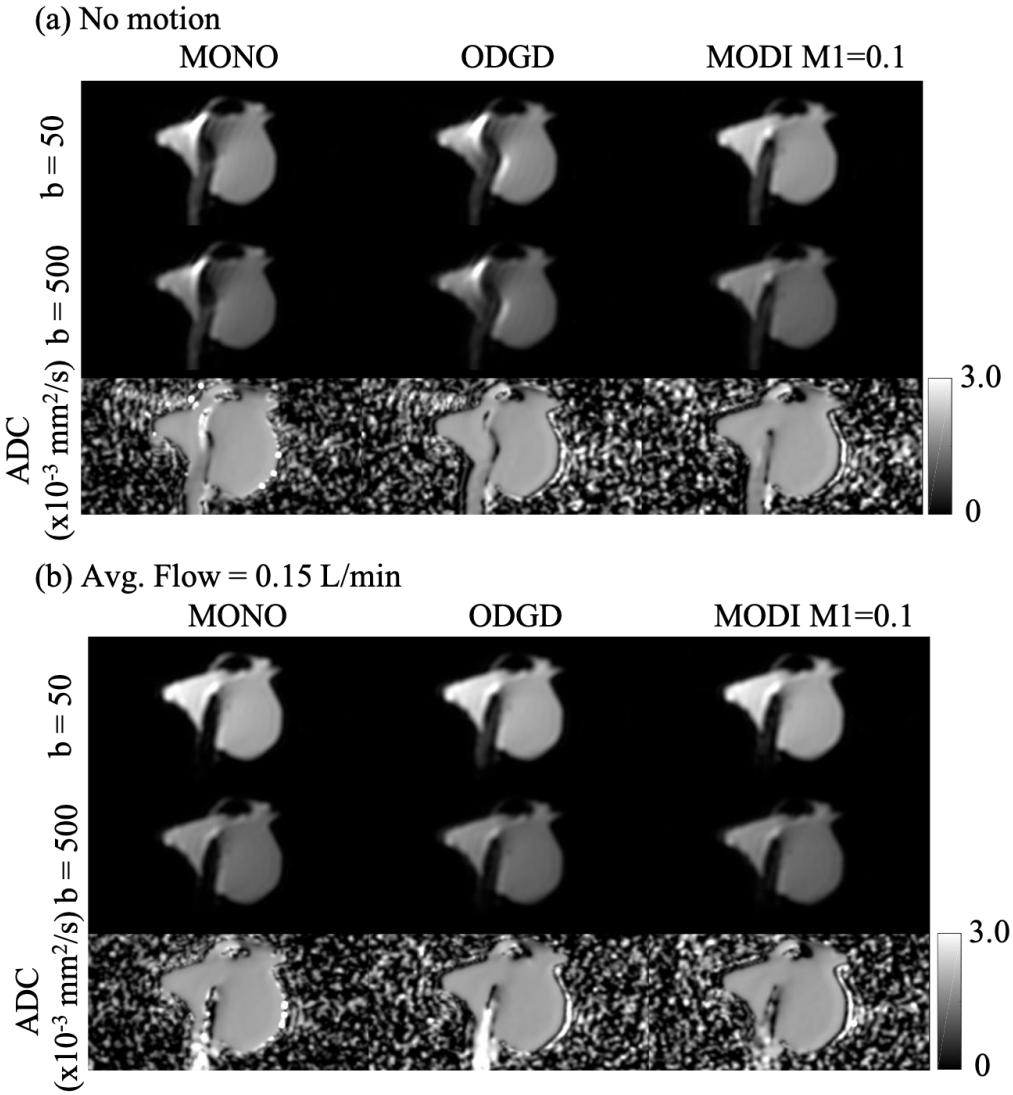

Figure 34. Demonstration of blood suppression effect in the liver motion phantom.
(a) Without added flow, the static 'blood' signal is visible in all three sequences. (b) When imposing a slow flow rate to mimic the blood flow in real liver, the 'blood' signal disappeared in MONO series at both b = 50 s/mm2 and 500 s/mm2. Due to the fully nulled first moment, the 'blood' signal comes back in b = 50 s/mm2 with ODGD waveform and thus shows up bright in the ADC map. In contrast, MODI with a small residual first moment, is able to suppress the blood signal, similar to the MONO waveform, and provide a clean ADC map around the vessel.

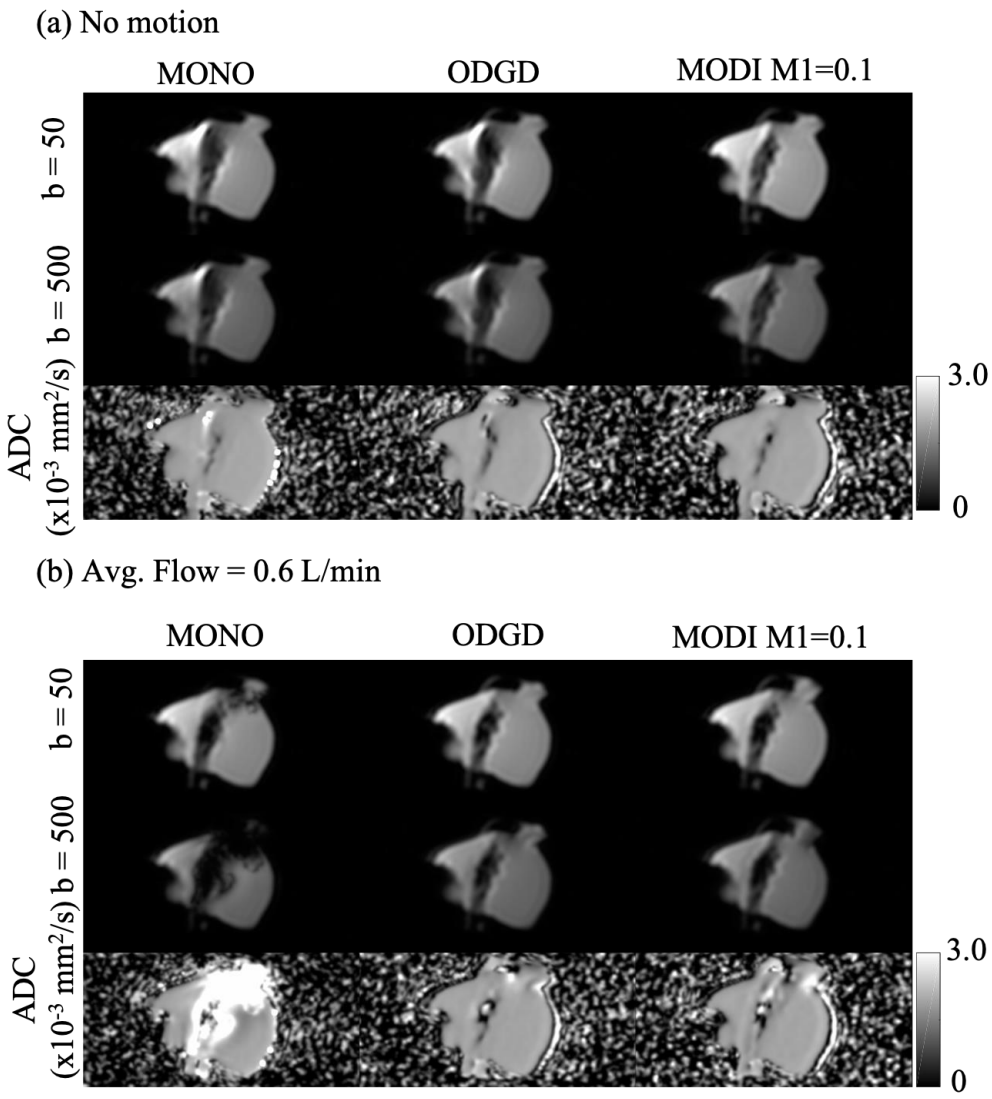

Figure 35. Demonstration of motion compensation in the liver motion phantom.

(a) Without added flow to impose pulsation motion, the DW images showed no motion artifacts in all three sequences, with or without motion compensation. (b) With added motion through the controlled water pump, substantial signal loss and ADC bias showed up in adjacent to the vessel with MONO acquisition. At the same average flow amplitude (i.e. the same motion level), both ODGD and MODI waveforms are insensitive to motion and have no ADC bias compared to the ones without motion.

6.3 Results

6.3.1 Anthropomorphic Liver Phantom Validation

Figure 34 demonstrates the blood-suppression effect of MODI waveform at a slow added flow. Without added flow, the static 'blood' signal is visible in all three sequences, MONO, ODGD, and MODI. When imposing a slow flow rate to mimic the blood flow in real liver, the 'blood' signal disappeared in MONO series at both b = 50 s/mm^2 and 500 s/mm^2. Due to the fully nulled first moment, the 'blood' signal comes back in b = 50 s/mm^2 with ODGD waveform and thus shows up bright in the ADC map. In contrast, MODI with a small residual first moment, is able to suppress the blood signal, similar to the MONO waveform, and provide a clean ADC map around the vessel.

The motion compensation effect of motion-compensated waveforms is presented in **Figure 35**. Without added flow to impose pulsation motion, the DW images showed no motion artifacts in all three sequences, with or without motion compensation. With added motion through the controlled water pump, substantial signal loss and ADC bias showed up in adjacent to the vessel with MONO acquisition. At the same average flow amplitude (i.e. the same motion level), both ODGD and MODI waveforms are insensitive to motion and have no ADC bias compared to the ones without motion.

The synergy between the motion-compensated waveform (i.e. MODI) and msEPI acquisition is also proved with the liver motion phantom, as shown in **Figure 36**. Substantial geometric distortion can be identified in ssEPI images as pointed by the red arrows as an example. msEPI has be capability to greatly mitigate the distortion artifacts, though not fully eliminate them. With the presence of imposed motion from water pump around the knob area, significant signal

loss and ADC bias are introduced (yellow arrowheads). With MODI, the motion artifacts are compensated in both ssEPI and msEPI acquisitions. Furthermore, at the same window level of the DW images, we are able to see that the parallel imaging performance is not ideal for MONO-msEPI, which is likely due to the variation between shots. The synergy between MODI and msEPI can be observed with the improved reconstruction performance.

6.3.2 Healthy Volunteer Experiment

Figure 37 shows example DW images from two out of the eight healthy volunteers. The yellow curve in volunteer (a) depicts the contour of the liver from the T2w reference. The mis-alignment between the contour and the liver anatomy due to distortion in the DW images is indicated by yellow arrowheads. Images with msEPI acquisition have substantially reduced distortion artifacts. Blue arrowheads show the motion-induced signal voids and ADC bias in the left liver lobe, which was reduced by MODI acquisition. The worm-hole artifacts indicated by red arrows in the msEPI reconstruction with MONO acquisition were likely due to the motion-induced rapid spatial phase variations, which were mitigated when combining msEPI with MODI.

CCC comparison in **Figure 38** illustrates the synergy between motion-robust diffusion waveform and msEPI acquisition. The alignment between DW images from MONO-ssEPI and the T2w reference is higher than MONO-msEPI ($p=0.0051$) even though the visually observed distortion artifact is largely reduced in MONO-msEPI (**Figure 37**). This is likely due to the substantial signal voids in the left liver lobe and the worm-hole artifacts. With MODI waveform (ii), msEPI has significant improvement ($p<0.0001$) in terms of alignment, which indicates significantly reduced distortion.

Bland-Altman analysis in **Figure 39** demonstrates reduced ADC bias of the left liver lobe due to the motion-robust MODI acquisition. The ADC values in the left liver lobe of MONO-ssEPI and MONO-msEPI have significant bias compared to the right lobe. However, with MODI acquisitions, no significant bias was observed in both ssEPI and msEPI acquisitions.

The detailed average CCC and ADC measurements across volunteers, as well as their standard deviation and t-test results, are listed in **Table 18**.

Finally, **Figure 40** shows an example in healthy volunteer of how DL denoising improve the SNR of DW images acquired with MODI waveform. The yellow arrows indicate the left lobe of the liver where MONO leads to severe shading and signal dropouts in DWI and bias (overestimation) in ADC maps. MODI is able to mitigate the signal dropouts with consistent ADC throughout the liver. However, MODI DWI had lower SNR compared to MONO. By combining MODI with the DL reconstruction, MODI-DL DWI shows higher SNR and is able to maintain excellent motion-robustness throughout the liver.

Figure 42 is an example of the combination of motion-compensated waveform, msEPI acquisition and DL denoising reconstruction, which demonstrated the ability of achieving motion-robust, low-distortion, and high-SNR DW-MRI in the liver.

The mean ADC measurements and the STD of ADCs are analyzed with boxplots in **Figure 41**. The top plots show the mean ADC measurements in left lobe and right lobe ROIs, respectively, across the eight healthy volunteers. This demonstrates that the DL denoising reconstruction will not impact the accuracy of ADC measurements in the liver. The bottom boxplots illustrate the difference of standard deviation of ADC measurements within ROIs between MONO, MODI, and MODI with DL denoising. The blue dashed lines show the individual change of STD without and

with DL denoising. It is shown that DL denoising is able to consistently reduce the STD of ADC in both left and right lobes of liver, thus increase the ADC SNR.

6.4 Discussion

In this study, we have investigated the feasibility and reproducibility of motion-robust and distortion-corrected DW-MRI by combining optimized motion-compensated diffusion waveforms (i.e. MODI) and msEPI acquisition. Deep Learning based denoising is also evaluated to further improve the SNR of DW images. The effectiveness of this combined approach to achieve motion-robust, low-distortion, and high-SNR liver DWI has been proved in an anthropomorphic liver motion phantom and healthy liver volunteers.

In the liver motion phantom experiment, we first proved the effectiveness of MODI in motion compensation at 0.6 L/min flow and blood suppression at 0.15 L/min flow, in comparison to the traditional monopolar waveform and the M1-nulled motion-compensated gradient waveform. The phantom experiment also demonstrated the synergies between the motion-compensated waveform (i.e. MODI in this study) and msEPI acquisition. The use of msEPI acquisition is able to reduce the geometric distortion but the combination of shots is impacted by the rapid magnitude and phase variation between shots under the presence of motion. In contrast, with the motion-compensated waveform, this variation is significantly reduced between shots. Thus, msEPI reconstruction, which is based on the smooth phase assumption, is facilitated to generate high-quality images.

Volunteer study showed promising image quality with reduced ADC bias in the left lobe as well as reduced distortion. The Bland-Altman analysis demonstrated the ADC bias with monopolar acquisitions in both ssEPI and msEPI series. The use of motion-compensated MODI

waveforms enables consistent ADC measurements across the liver in all healthy volunteers. More importantly, this work also demonstrated the potential synergy of combining MODI and msEPI techniques. The CCC measurements (**Figure 38**) provides convincing evidence of this synergy. Even though the distortion reduction effect of msEPI is visible in DW images, there is no prominent trend of increased CCC values from ssEPI to msEPI acquisitions. This is resulted from the unpredictable signal loss in the left lobe of liver. However, with MODI waveform, we are able to identify a significant increase of CCC when using msEPI readout.

Despite the advantages of motion-compensate waveform, SNR is an unavoidable trade-off due to the lengthened TE and the low T2 value of liver tissue. The application of Deep-Learning based reconstruction shows potential to restore the SNR without sacrificing boundary sharpness and ADC accuracy.

This study still has limitations. First of all, the motion phantom is using a pulsation model instead of directly mimicking the cardiac motion due to constructing limitations. The phantom also has higher T2 value compared to real liver with the current material. Future work will include better motion phantom design that considers realistic respiratory motion, cardiac motion and vessel pulsation. Besides, the volunteer study is conducted with breath-holding to save the total acquisition time and avoid the confounding effect from respiratory. Future study needs to explore the possibility of free-breathing liver DWI with inter-repetition respiratory motion correction. Finally, this study is only performed in phantom and healthy volunteers, without characterization of lesions. Patient study needs to be performed in the future to further evaluate the reproducibility and clinical viability of the proposed approach.

6.5 Conclusion

In conclusion, the synergetic effects of combined motion-compensated diffusion waveforms, msEPI acquisitions and deep-learning based denoising reconstruction can enable reproducible and robust liver DWI with motion-robustness, reduced distortion and high SNR.

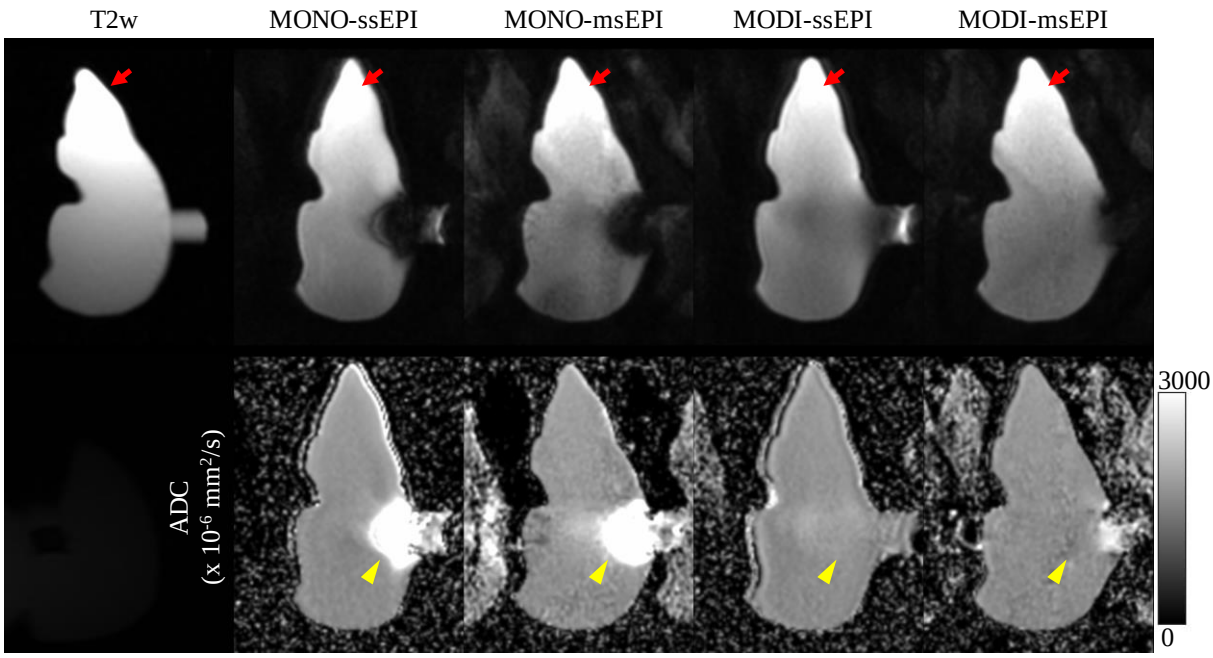

Figure 36. Demonstration of combined MODI and msEPI technique in liver motion phantom. The top row shows the non-EPI T2-weighted reference image and the b = 500 s/mm^2 DW images of the four imaging sequences. The bottom row are the ADC maps of the corresponding DWI series. Substantial geometric distortion can be identified in ssEPI images as pointed by the red arrows as an example. msEPI has be capability to greatly mitigate the distortion artifacts, though not fully eliminate them. With the presence of imposed motion from water pump around the knob area, significant signal loss and ADC bias are introduced (yellow arrowheads). With MODI, the motion artifacts are compensated in both ssEPI and msEPI acquisitions. Furthermore, at the same window level of the DW images, we are able to see that the parallel imaging performance is not ideal for MONO-msEPI, which is likely due to the variation between shots. The synergy between MODI and msEPI can be observed with the improved reconstruction performance.

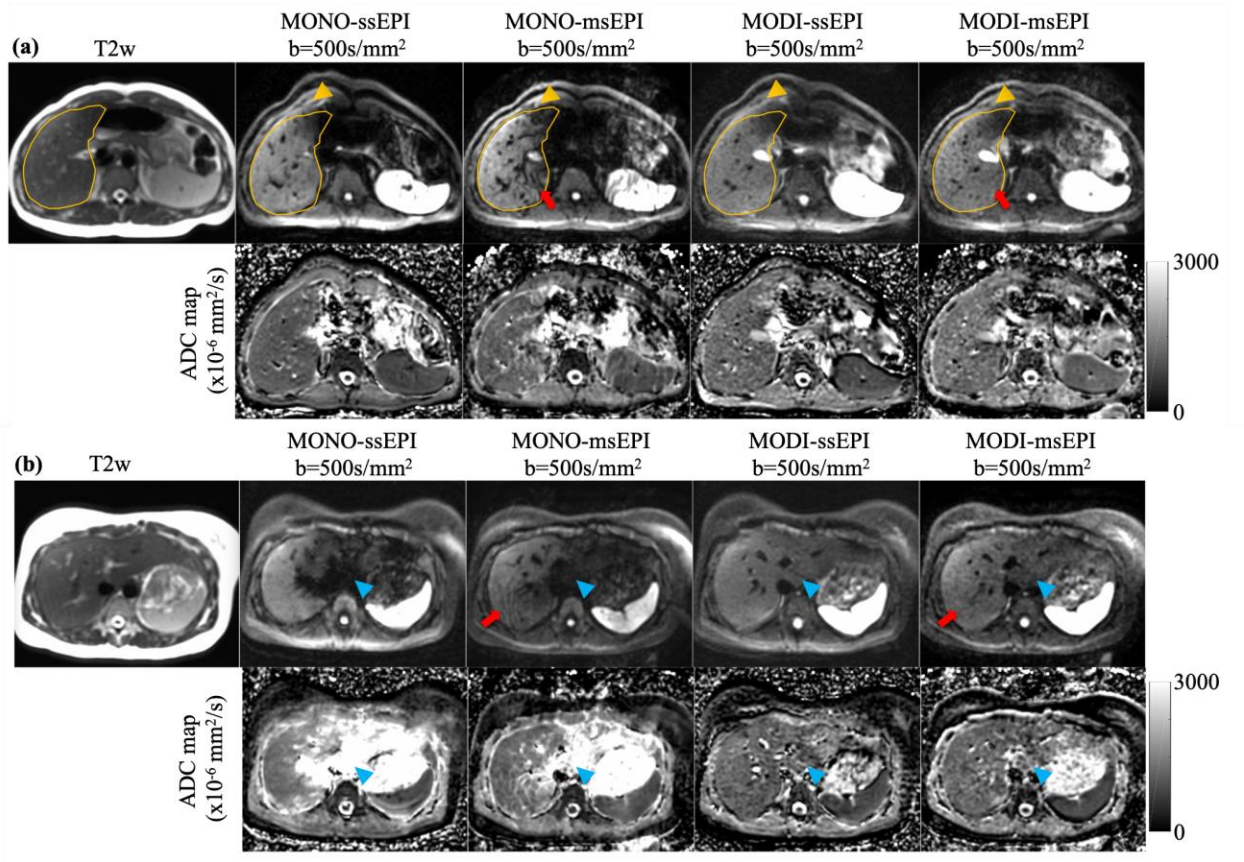

Figure 37. Example images of two healthy volunteers. This figure compares MONO and MODI waveforms, each using ssEPI and msEPI acquisitions. The yellow curve in volunteer (a) depicts the contour of the liver from the T2w reference. The mis-alignment between the contour and the liver anatomy due to distortion in the DW images is shown by the yellow arrowheads. Blue arrowheads show the motion-induced signal voids and ADC bias in the left lobe, which were significantly reduced by the MODI acquisition. Red arrows in both (a) and (b) point to the worm-hole artifacts in the MONO-msEPI reconstruction caused by the rapid spatial phase variation.

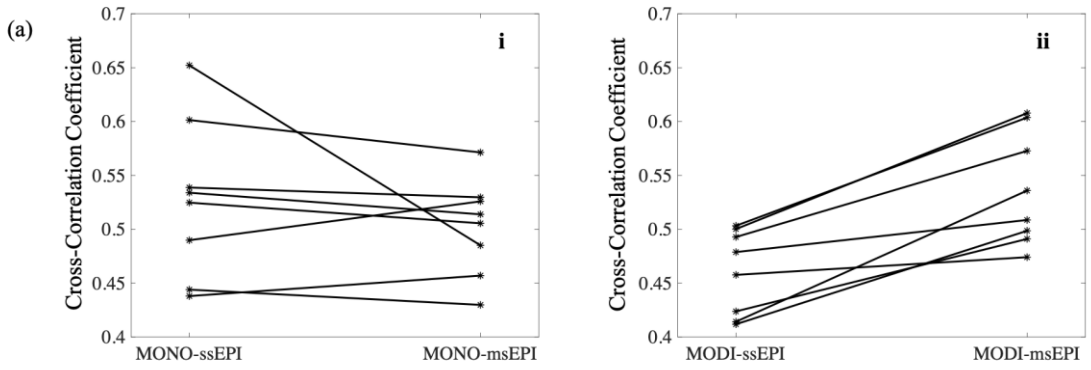

Figure 38. CCC measurements in healthy volunteers. Synergy between motion-robust diffusion waveform and msEPI acquisition. Each plot compares the CCC between ssEPI and msEPI acquisitions with MONO waveform (i) and MODI waveform (ii). Each point represents the averaged CCC over slices for one volunteer and each pair of connected points depicts the change of CCC between two acquisitions of the same volunteer.

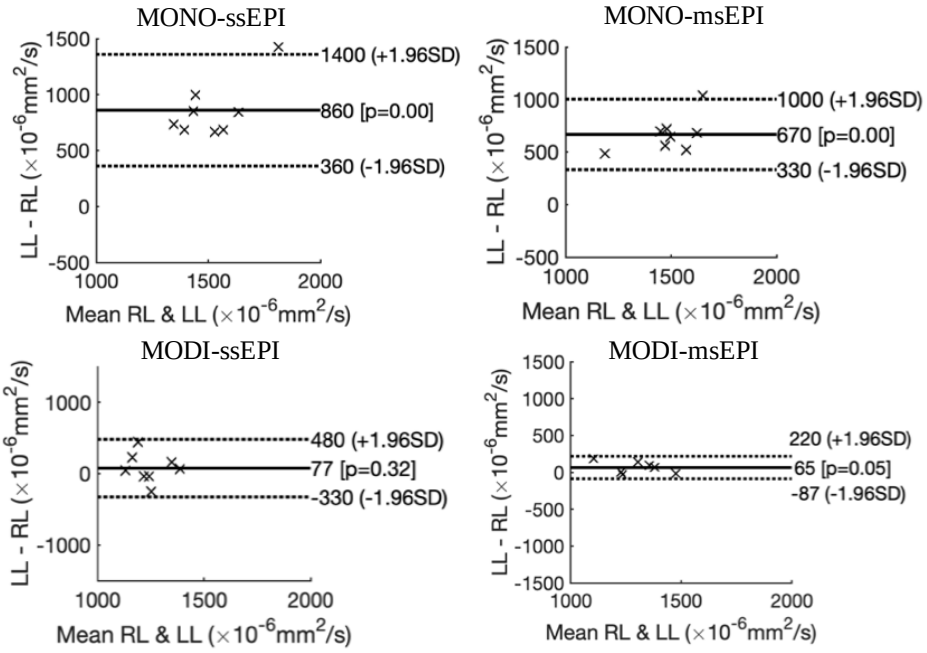

Figure 39. Bland-Altman analysis of ADC values in healthy volunteers. Bland-Altman analysis comparing ADC values between left and right liver lobes for the four techniques. Significant ADC bias of MONO acquisitions are observed in the left lobe, whereas both MODI acquisitions have no significant bias.

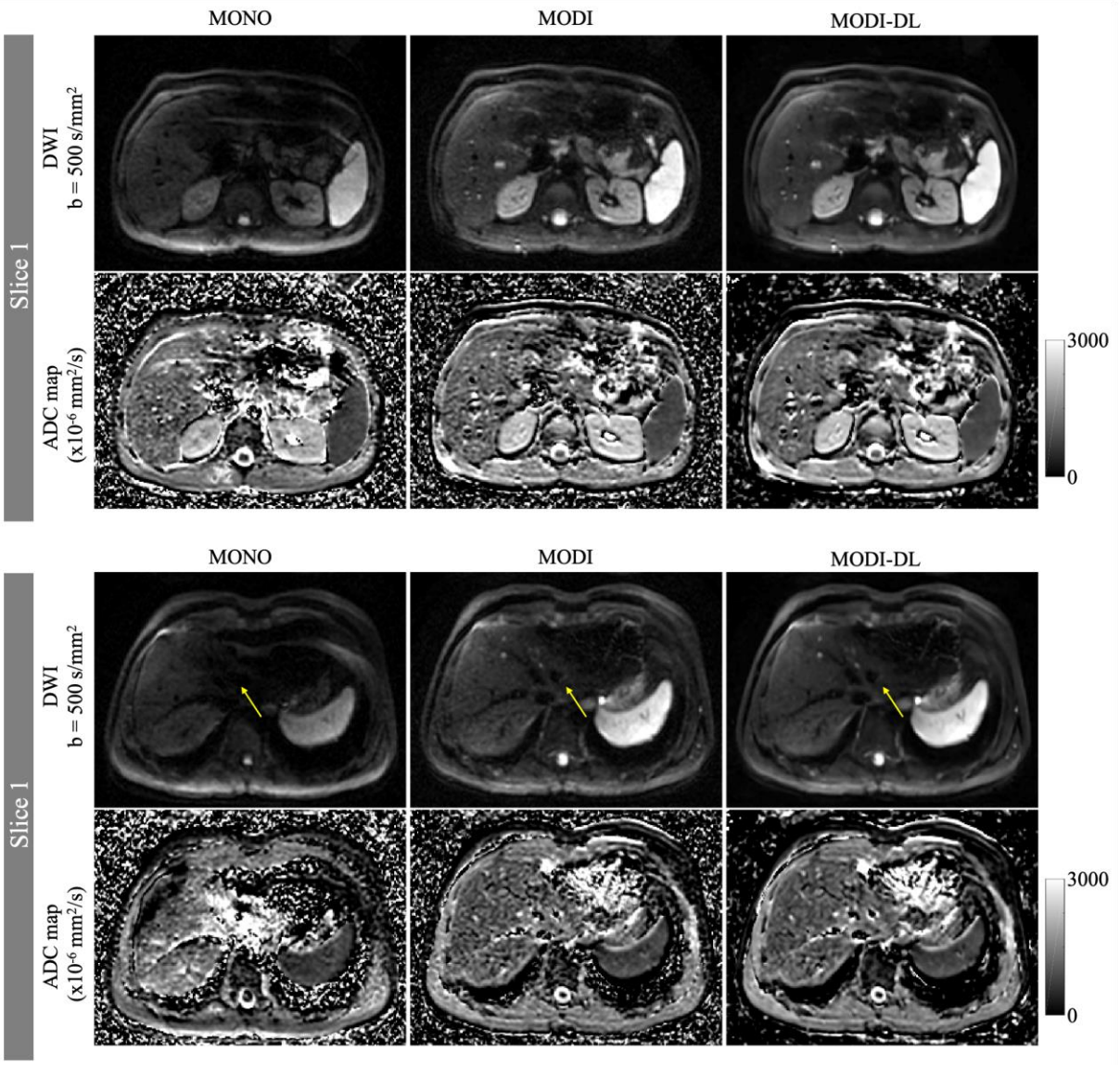

Figure 40. Example images of MONO, MODI and MODI-DL in a volunteer.
The yellow arrows indicate the left lobe of the liver where MONO leads to severe shading and signal dropouts in DWI and bias (overestimation) in ADC maps. MODI is able to mitigate the signal dropouts with consistent ADC throughout the liver. However, MODI DWI had lower SNR compared to MONO. By combining MODI with the DL reconstruction, MODI-DL DWI shows higher SNR and is able to maintain excellent motion-robustness throughout the liver.

Table 18. Average ADC and CCC measurements across healthy volunteers.

(a) ADC measurements		MONO-ssEPI	MONO-msEPI	MODI-ssEPI	MODI-msEPI
ADC ($x10^{-6}mm^2/s$)	Left Lobe	1951.0±257.3	1825.4±207.4	1155.1±229.3	1292.7±146.5
	Right Lobe	1090.4±110.7	1158.1±114.7	1202.6±145.1	1227.5±171.5
	p-value	<0.0001****	<0.0001****	0.7999	0.0512
(b) CCC evaluation		MONO-ssEPI	MONO-msEPI	MODI-ssEPI	MODI-msEPI
CCC	Meas.	0.53±0.08	0.50±0.06	0.46±0.06	0.54±0.07
	p-value	0.0051**		<0.0001****	

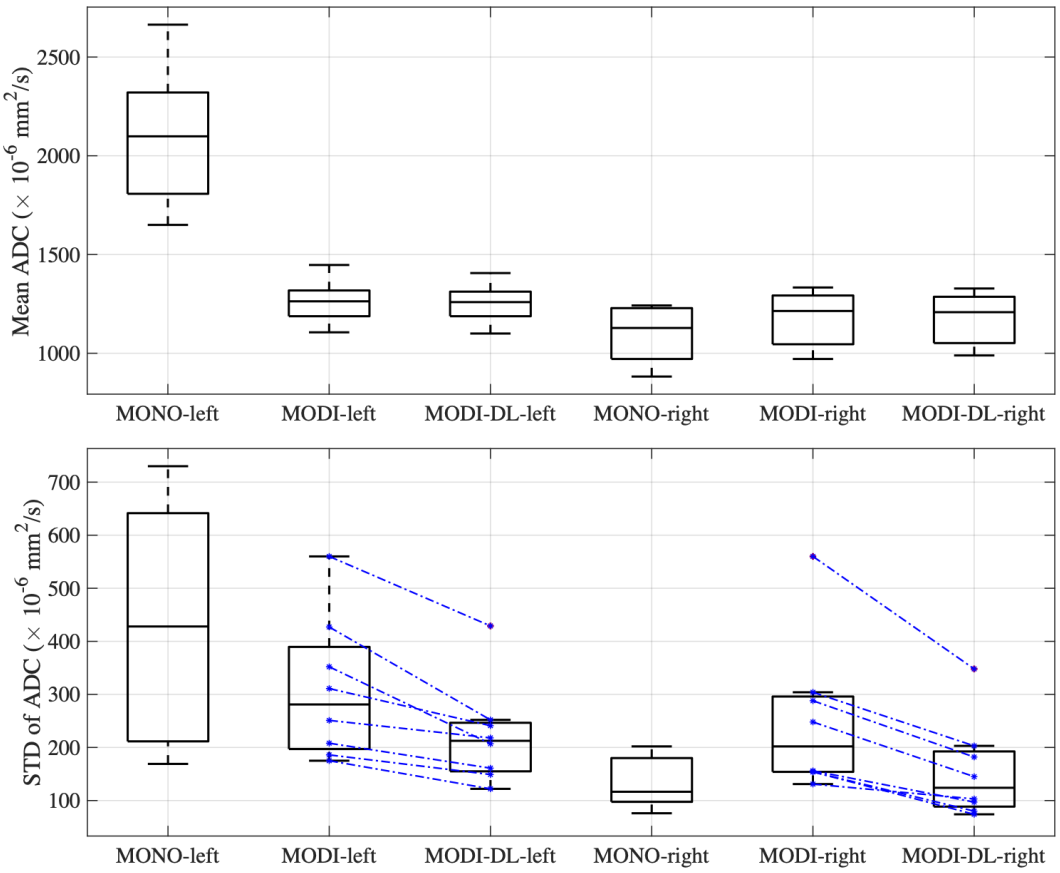

Figure 41. Boxplots of mean ADC and standard deviation measurements with and without DL denoising.

The top figure shows the box plots of mean ADC measurements in left lobe and right lobe ROIs across the eight healthy volunteers. This demonstrates that the DL denoising reconstruction will not alter the accuracy of ADC measurements in the liver. The bottom boxplots illustrate the difference of standard deviation of ADC measurements within ROIs between MONO, MODI, and MODI with DL denoising. The blue dashed lines show the individual change of STD without and with DL denoising. It is shown that DL denoising is able to consistently reduce the STD of ADC in both left and right lobes of liver, thus increase the ADC SNR.

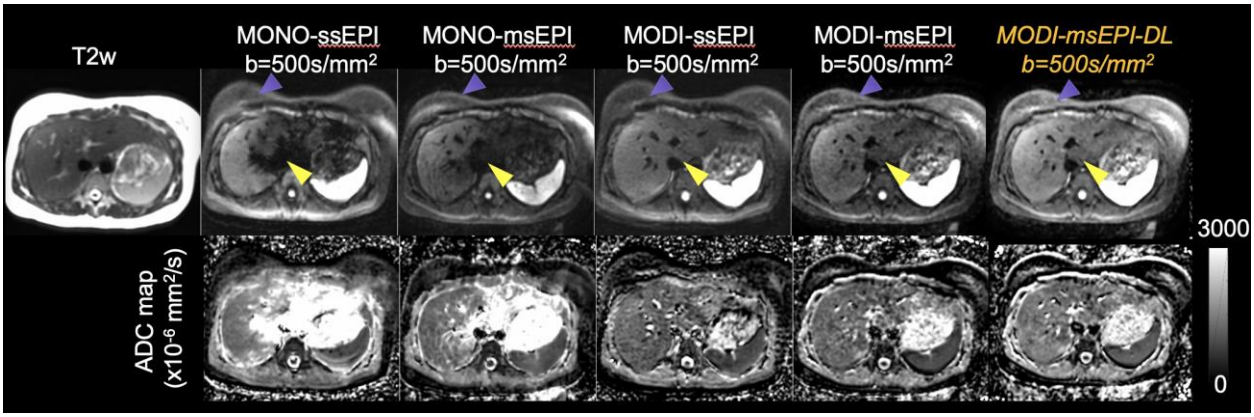

Figure 42. Volunteer example of motion-robust, low-distortion, and high-SNR DW-MRI in the liver. The top row shows the non-EPI T2-weighted reference image and the b = 500 s/mm^2 DW images of the four imaging sequences. The bottom row are the ADC maps of the corresponding DWI series. Purple arrowheads show the distortion artifacts in the Anterior-Posterior (phase encoding) direction and msEPI acquisitions are able to significantly mitigate the image distortion. Yellow arrowheads are cardiac motion induced signal dropouts, which are corrected with MODI waveform. Furthermore, DL-denoising reconstruction provides higher SNR in the diffusion weighted image and ADC map. Overall, the combination of MODI, msEPI acquisition, and DL reconstruction has the ability to achieve motion robustness, low distortion and high SNR at the same time.

Chapter

7. Summary and Future Works

7.1 Summary

This thesis incorporates MRI pulse sequence design, signal modeling, image reconstruction, data analysis, and assessment of techniques in simulation, phantom, and human studies.

A Stimulated-Echo based Mapping (STEM) method has been proposed for simultaneous quantitative T1, T2 and ADC mapping. The overall T1, T2 and ADC measurements have been shown to be accurate in phantom experiments, brain and prostate imaging. Further, protocol optimization was performed to achieve accurate STEM quantification within five minutes. The proposed STEM method may enable rapid and co-registered multi-parametric imaging, with potential clinical applications in the brain, prostate, and breast, among others.

The ability of STE DWI of the prostate to overcome the inherent tradeoffs with SE DWI has been assessed, in order to obtain high CNR and reliable ADC maps in a single acquisition. Based on quantitative evaluation, STE DWI at moderate b-value has significant advantage in SNR over high b-value SE DWI and comparable CNR performance to high b-value SE DWI. From qualitative assessment from the reader study, all readers have shown preference to STE b=800 s/mm^2 DWI over SE b=1500s/mm^2 in terms of SNR. Most readers prefer the CNR of SE b = 1500

s/mm^2 and the overall diagnostic confidence of SE b = 1500 s/mm^2 and STE b = 800 s/mm^2 is shown to be comparable. However, the number of identified lesions from SE b = 1500 s/mm^2 and STE b = 800 s/mm^2 indicates that both sequences have clinically reliable lesion detectability compared to SE b = 800 s/mm^2.

A M1-Optimized Diffusion Imaging (MODI) method was proposed to acquire motion-robust, blood-suppressed liver DWI with optimized diffusion encoding waveforms. Healthy volunteer experiments and a feasibility evaluation in patients have been performed to investigate the bias of the proposed MODI method. Compared to the conventional monopolar DWI, MODI is able to provide ADC measurements with reduced bias, particularly in the left lobe of the liver. In contrast to the moment-nulling waveforms, MODI can dephase most of the blood signal throughout the liver and generate more reliable ADC maps. Overall, the proposed MODI method is promising for obtaining reliable DW images and quantitative ADC measurements over the entire liver.

The reproducibility of quantitative diffusion measurements across different pulse sequences (ssEPI, rFOV and msEPI) are evaluated in phantoms and prostate of healthy volunteers and clinical patients. From our results, quantitative diffusion measurements obtained from recently developed reduced-distortion pulse sequences (rFOV and msEPI) were in good agreement with the standard ssEPI-based measurements. In combination with the reduced distortion provided by these novel pulse sequences, these results demonstrate the potential of rFOV and msEPI, at the cost of FOV size or scan time, to provide reproducible quantitative diffusion measurements compared to ssEPI. This potential may have significant research and clinical implications for diffusion MRI of the prostate.

We have also investigated the feasibility and reproducibility of motion-robust and distortion-corrected DW-MRI by combining optimized motion-compensated diffusion waveforms (i.e. MODI) and msEPI acquisition. Volunteer study showed promising image quality with reduced ADC bias in the left lobe as well as reduced distortion. Importantly, this work demonstrated the synergy of combining MODI and msEPI techniques resulted from the phase consistency between shots offered by the motion-robust diffusion waveforms.

7.2 Future Works

7.2.1 Evaluation of the proposed techniques in a large patient cohort

In this thesis work, technical developments have been described to address challenges in body DWI. Feasibility and reproducibility of the proposed techniques have been evaluated in phantoms, healthy volunteers, and a small cohort of patient population. However, to further assess the clinical robustness of these techniques, patient studies with a larger patient population are still needed. More specifically, the following clinical studies need to be investigated:

1) The proposed STEM method for simultaneous T1, T2 and ADC mapping needs to be evaluated in either brain or prostate patients. With a large patient cohort, we will have the possibility to explore the three-dimensional parametric space that could potentially characterize different diseases. By testing the optimized rapid STEM acquisitions, we will be able to evaluate the clinical viability of acquiring quantitative T1, T2 and ADC maps and using them as potential lesion diagnostic tools.

2) The STE-DWI acquisition with moderate b-values needs to be further evaluated across different gradient performance (i.e. different type of scanners) in prostate patients with suspected prostate cancer. A more thorough design of clinical study is needed to confirm the high-CNR performance and ADC robustness of the STE-DWI acquisitions in the prostate. This also has synergy with the previously described STEM study because they both use a similar pulse sequence design.
3) The proposed combined method of MODI and msEPI for motion-robust, distortion-reduced DWI in the liver also requires clinical validation in a large patient cohort with liver metastases. A systematic test-retest experiment and evaluation by experienced radiologists would be important to prove the clinical repeatability of this technique. In addition, multi-scanner and multi-center studies needs to be performed in order to assess the reproducibility.

7.2.2 Extension and improvement of the motion-robust DWI technique

Cardiac motion or cardiac pulsation introduced motion artifact is a major challenge of liver DWI. However, many other applications are facing the same issue. Example applications include, but not limited to, pancreas and esophagus DWI. The feasibility, reproducibility and repeatability of motion-robust diffusion gradient design are being evaluated in these applications with promising preliminary results. Future work needs to be conducted to optimize and evaluate the motion-robust DWI technique (i.e. MODI) performance in these extended applications in healthy volunteers and patients.

The MODI acquisition itself and the signal modeling of MODI signals need to be investigated in future studies as well. First, an empirical M1 value was used in this thesis and

proved to work. However, the M1 value needs to be optimized based on physiological parameters and/or Cramér-Rao Lower Bound performance with digital simulation. Besides, using a fixed M1 value across b-values will affect the Intravoxel Incoherent Motion (IVIM) effect where the signal decay behaves differently from using traditional monopolar diffusion encoding. Thus, a more accurate signal model for IVIM effect in the liver needs to be studied and evaluated.

Bibliography

1. Jones DK. *Diffusion MRI*. Oxford University Press; 2010.
2. Bammer R. Basic principles of diffusion-weighted imaging. *Eur J Radiol*. 2003;45(3):169-184. doi:10.1016/S0720-048X(02)00303-0
3. Dietrich O, Biffar A, Baur-melnyk A, Reiser MF. Technical aspects of MR diffusion imaging of the body. *Eur J Radiol*. 2010;76(3):314-322. doi:10.1016/j.ejrad.2010.02.018
4. Koh DM, Collins DJ. Diffusion-weighted MRI in the body: Applications and challenges in oncology. *Am J Roentgenol*. 2007;188(6):1622-1635. doi:10.2214/AJR.06.1403
5. Padhani AR, Liu G, Mu-Koh D, et al. Diffusion-Weighted Magnetic Resonance Imaging as a Cancer Biomarker: Consensus and Recommendations. *Neoplasia*. 2009;11(2):102-125. doi:10.1593/neo.81328
6. Follow-up T. Principles and Applications of Diffusion-weighted Imaging in Cancer. 2011.
7. Barentsz JO, Richenberg J, Clements R, et al. ESUR prostate MR guidelines 2012. *Eur Radiol*. 2012;22(4):746-757. doi:10.1007/s00330-011-2377-y
8. Rooij M De, Hamoen EHJ, Barentsz JO, Rovers MM. Accuracy of Multiparametric MRI for Prostate Cancer. 2014;(February). doi:10.2214/AJR.13.11046
9. Surov A, Jonas H, Wienke A. Correlations between Apparent Diffusion Coefficient and Gleason Score in Prostate Cancer : A Systematic Review. 2019;3:0-8. doi:10.1016/j.euo.2018.12.006
10. Chung W, Kim M, Chung YE, et al. Comparison of Gadoxetic Acid-Enhanced Dynamic Imaging and Diffusion-Weighted Imaging for the Preoperative Evaluation of Colorectal Liver Metastases. 2011;353:345-353. doi:10.1002/jmri.22671

11. Macera A, Lario C, Petracchini M, et al. Staging of colorectal liver metastases after preoperative chemotherapy . Diffusion-weighted imaging in combination with Gd-EOB-DTPA MRI sequences increases sensitivity and diagnostic accuracy. 2013:739-747. doi:10.1007/s00330-012-2658-0

12. Zhang H, Li W, Fu C, Grimm R, Chen Z, Zhang W. Comparison of intravoxel incoherent motion imaging , diffusion kurtosis imaging , and conventional DWI in predicting the chemotherapeutic response of colorectal liver metastases. *Eur J Radiol*. 2020;130(December 2019):109149. doi:10.1016/j.ejrad.2020.109149

13. Taouli B, Kow D-M. Diffusion Weighted MR Imaging of the Liver. *Radiology*. 2010;254:47-66. doi:10.1148/radiol.09090021

14. Neema M, Stankiewicz J, Arora A, et al. T1- and T2-based MRI measures of diffuse gray matter and white matter damage in patients with multiple sclerosis. *J Neuroimaging*. 2007;17(SUPPL. 1):16-21. doi:10.1111/j.1552-6569.2007.00131.x

15. Bohnen S, Radunski UK, Lund GK, et al. Performance of T1 and T2 Mapping Cardiovascular Magnetic Resonance to Detect Active Myocarditis in Patients with Recent-Onset Heart Failure. *Circ Cardiovasc Imaging*. 2015;8(6):1-7. doi:10.1161/CIRCIMAGING.114.003073

16. Kershaw LE, Hutchinson CE, Buckley DL. Benign prostatic hyperplasia: Evaluation of T1, T2, and microvascular characteristics with T1-weighted dynamic contrast-enhanced MRI. *J Magn Reson Imaging*. 2009;29(3):641-648. doi:10.1002/jmri.21674

17. Gibbs P, Tozer DJ, Liney GP, Turnbull LW. Comparison of quantitative T2 mapping and diffusion-weighted imaging in the normal and pathologic prostate. *Magn Reson Med*. 2001;46(6):1054-1058. doi:10.1002/mrm.1298

18. Yankeelov TE, Lepage M, Chakravarthy A, et al. Integration of quantitative DCE-MRI and ADC mapping to monitor treatment response in human breast cancer: initial results. *Magn Reson Imaging*. 2007;25(1):1-13. doi:10.1016/j.mri.2006.09.006

19. Li K, Dortch RD, Welch EB, et al. Multi-parametric MRI characterization of healthy human thigh muscles at 3.0 T - relaxation, magnetization transfer, fat/water, and diffusion tensor imaging. *NMR Biomed*. 2014;27(9):1070-1084. doi:10.1002/nbm.3159

20. Morvan D, Leroy-willig A. Simultaneous measurements of diffusion and transverse relaxation in exercising skeletal muscle. *Science (80-)*. 1995;13(7):943-948.

21. Barral JK, Gudmundson E, Stikov N, Etezadi-Amoli M, Stoica P, Nishimura DG. A robust methodology for in vivo T1 mapping. *Magn Reson Med*. 2010;64(4):1057-1067. doi:10.1002/mrm.22497

22. Deoni SCL, Rutt BK, Peters TM. Rapid combined T1 and T2 mapping using gradient recalled acquisition in the steady state. *Magn Reson Med*. 2003;49(3):515-526. doi:10.1002/mrm.10407

23. Deoni SCL, Peters TM, Rutt BK. High-resolution T1 and T2 mapping of the brain in a clinically acceptable time with DESPOT1 and DESPOT2. *Magn Reson Med*. 2005;53(1):237-241. doi:10.1002/mrm.20314

24. Gras V, Farrher E, Grinberg F, Shah NJ. Diffusion-weighted DESS protocol optimization for simultaneous mapping of the mean diffusivity, proton density and relaxation times at 3 Tesla. *Magn Reson Med*. 2017;78(1):130-141. doi:10.1002/mrm.26353

25. Jiang Y, Wright KL, Seiberlich N, Gulani V, Griswold MA. Simultaneous T1, T2, diffusion and proton density quantification with MR fingerprinting. *Proc 22nd Annu Meet ISMRM Meet Exhib Milan, Italy*. 2014:28. doi:10.1002/mrm.21165

26. Ma D, Coppo S, Chen Y, et al. Slice profile and B1 corrections in 2D magnetic resonance fingerprinting. *Magn Reson Med*. 2017;78(5):1781-1789. doi:10.1002/mrm.26580

27. Yu AC, Badve C, Ponsky LE, et al. Development of a Combined MR Fingerprinting and Diffusion Examination for Prostate Cancer. *Radiology*. 2017;283(3):729-738. doi:10.1148/radiol.2017161599

28. Merboldt, Klaus-Dietmar Hanicke WFJ. Diffusion Imaging Using Stimulated Echoes. *Magn Reson Med*. 1991;239:233-239.

29. Torre LA, Freddie Bray RL, Siegel JF, Lortet-Tieulent J, Ahmedin J. Global cancer statistics, 2012. *CA Cancer J Clin*. 2015;65(2):87-108.

30. Siegel RL, Miller KD, Jemal A. Cancer statistics, 2019. *CA Cancer J Clin*. 2019;69(1):7-34. doi:10.3322/caac.21551

31. Barentsz JO, Richenberg J. UROGENITAL ESUR prostate MR guidelines 2012. 2012:746-757. doi:10.1007/s00330-011-2377-y

32. Ahmed HU, Bosaily AE, Brown LC, et al. Diagnostic accuracy of multi-parametric MRI and TRUS biopsy in prostate cancer (PROMIS): a paired validating confi rmatory study. *Lancet*. 389(10071):815-822. doi:10.1016/S0140-6736(16)32401-1

33. Langer DL, Van Der Kwast TH, Evans AJ, Trachtenberg J, Wilson BC, Haider MA. Prostate cancer detection with multi-parametric MRI: Logistic regression analysis of quantitative T2, diffusion-weighted imaging, and dynamic contrast-enhanced MRI. *J Magn Reson Imaging*. 2009;30(2):327-334. doi:10.1002/jmri.21824

34. Tamada T, Kanomata N, Sone T, et al. High b value (2,000 s/mm2) diffusion-weighted magnetic resonance imaging in prostate cancer at 3 tesla: Comparison with 1,000 s/mm 2for tumor conspicuity and discrimination of aggressiveness. *PLoS One*. 2014;9(5):3-10.

doi:10.1371/journal.pone.0096619

35. Metens T, Miranda D, Absil J, Matos C. What is the optimal b value in diffusion-weighted MR imaging to depict prostate cancer at 3T? *Eur Radiol*. 2012;22(3):703-709. doi:10.1007/s00330-011-2298-9

36. Itajima KK, Aji YK, Uroda KK, Ugimura KS. High b-value Diffusion-weighted Imaging in Normal and Malignant Peripheral Zone Tissue of the Prostate : Effect of Signal-to-Noise Ratio. 2008;7(2):93-99.

37. Agarwal HK, Mertan F V., Sankineni S, et al. Optimal high b-value for diffusion weighted MRI in diagnosing high risk prostate cancers in the peripheral zone. *J Magn Reson Imaging*. 2017;45(1):125-131. doi:10.1002/jmri.25353

38. Xi Y, Liu A, Olumba F, et al. Low-to-high b value DWI ratio approaches in multiparametric MRI of the prostate: feasibility, optimal combination of b values, and comparison with ADC maps for the visual presentation of prostate cancer. *Quant Imaging Med Surg*. 2018;8(6):557-567. doi:10.21037/qims.2018.06.08

39. Tamada T, Sone T, Jo Y, Yamamoto A, Ito K. Diffusion-weighted MRI and its role in prostate cancer. *NMR Biomed*. 2014;27(1):25-38. doi:10.1002/nbm.2956

40. Tamada T, Kanomata N, Sone T, et al. Magnetic Resonance Imaging in Prostate Cancer at 3 Tesla : Comparison with 1 , 000 s / mm 2 for Tumor Conspicuity and Discrimination of Aggressiveness. 2014;9(5):3-10. doi:10.1371/journal.pone.0096619

41. Gatidis S, Schmidt H, Martirosian P. Apparent Diffusion Coefficient-Dependent Voxelwise Computed Diffusion-Weighted Imaging : An Approach for Improving SNR and Reducing T 2 Shine-Through Effects. 2015. doi:10.1002/jmri.25044

42. Shio KO, Kuda SO, Hinmoto HS. Removing Ambiguity Caused by T 2 Shine-through

using Weighted Diffusion Subtraction (WDS). 2016;15(1):146-148. doi:10.2463/mrms.2015-0001

43. Murphy P, Wolfson T, Gamst A, Sirlin C, Bydder M. Error model for reduction of cardiac and respiratory motion effects in quantitative liver DW-MRI. *Magn Reson Med*. 2013;70(5):1460-1469. doi:10.1002/mrm.24563

44. Kwee TC, Takahara T, Niwa T, et al. Influence of cardiac motion on diffusion-weighted magnetic resonance imaging of the liver. *Magn Reson Mater Physics, Biol Med*. 2009;22(5):319-325. doi:10.1007/s10334-009-0183-1

45. Aliotta E, Wu HH, Ennis DB. Convex optimized diffusion encoding (CODE) gradient waveforms for minimum echo time and bulk motion–compensated diffusion-weighted MRI. *Magn Reson Med*. 2017;77(2):717-729. doi:10.1002/mrm.26166

46. Peña-Nogales Ó, Zhang Y, Wang X, et al. Optimized Diffusion-Weighting Gradient Waveform Design (ODGD) formulation for motion compensation and concomitant gradient nulling. *Magn Reson Med*. 2018;(December 2018):989-1003. doi:10.1002/mrm.27462

47. Van AT, Cervantes B, Ogino T, et al. Partial velocity-compensated di usion encoding for combined motion compensation and residual vessel signal suppression in liver DWI. In: ; :10-12.

48. Kim H, Lee JM, Yoon JH, et al. Reduced field-of-view diffusion-weighted magnetic resonance imaging of the pancreas: Comparison with conventional single-shot echo-planar imaging. *Korean J Radiol*. 2015;16(6):1216-1225. doi:10.3348/kjr.2015.16.6.1216

49. Ma C, Li Y jun, Pan C shu, et al. High resolution diffusion weighted magnetic resonance imaging of the pancreas using reduced field of view single-shot echo-planar imaging at 3

T. *Magn Reson Imaging*. 2014;32(2):125-131. doi:10.1016/j.mri.2013.10.005

50. Saritas EU, Cunningham CH, Lee JH, Han ET, Nishimura DG. DWI of the spinal cord with reduced FOV single-shot EPI. *Magn Reson Med*. 2008;60(2):468-473. doi:10.1002/mrm.21640

51. Chen N kuei, Guidon A, Chang HC, Song AW. A robust multi-shot scan strategy for high-resolution diffusion weighted MRI enabled by multiplexed sensitivity-encoding (MUSE). *Neuroimage*. 2013;72:41-47. doi:10.1016/j.neuroimage.2013.01.038

52. Porter DA, Heidemann RM. High resolution diffusion-weighted imaging using readout-segmented echo-planar imaging, parallel imaging and a two-dimensional navigator-based reacquisition. *Magn Reson Med*. 2009;62(2):468-475. doi:10.1002/mrm.22024

53. Holdsworth SJ, Skare S, Newbould RD, Guzmann R, Blevins NH, Bammer R. Readout-segmented EPI for rapid high resolution diffusion imaging at 3T. *Eur J Radiol*. 2008;65(1):36-46. doi:10.1016/j.ejrad.2007.09.016

54. Lu H, Jensen JH, Ramani A, Helpern JA. Three-dimensional characterization of non-gaussian water diffusion in humans using diffusion kurtosis imaging. 2006;(March):236-247. doi:10.1002/nbm.1020

55. Hall MG, Bongers A, Sved P, Watson G, Bourne RM. Assessment of non-Gaussian diffusion with singly and doubly stretched biexponential models of diffusion-weighted MRI (DWI) signal attenuation in prostate tissue. 2015;(November 2014):486-495. doi:10.1002/nbm.3273

56. Provenzale M, Engelter S, Petrella R, Smith JS. A. MacFall1. 1999;(February):537-539.

57. Lemberskiy G, Rosenkrantz AB, Veraart J, Taneja SS, Novikov DS, Fieremans E. Time-dependent diffusion in prostate cancer. *Invest Radiol*. 2017;52(7):405-411.

doi:10.1097/RLI.0000000000000356

58. Wang X, Reeder SB, Hernando D. An Acetone-Based Phantom for Quantitative Diffusion MRI. 2017:1683-1692. doi:10.1002/jmri.25727

59. Helenius J, Soinne L, Perkio J, et al. Diffusion-Weighted MR Imaging in Normal Human Brains in Various Age Groups. 2002;(February):194-199.

60. Karlsen OT, Verhagen R, Bove WMMJ. Parameter Estimation From Rician-Distributed Data Sets Using a Maximum Likelihood Estimator : Application to T 1 and Perfusion Measurements. 1999;623(September 1998):614-623.

61. Sacolick LI, Wiesinger F, Hancu I, Vogel MW. B 1 Mapping by Bloch-Siegert Shift. 2010;1322:1315-1322. doi:10.1002/mrm.22357

62. Gilbert GE. Linear Mixed Models : A Practical Guide Using Statistical Software. 2012;1459. doi:10.1198/jasa.2008.s216

63. Clark CA, Hedehus M, Moseley ME. Diffusion Time Dependence of the Apparent Diffusion Tensor in Healthy Human Brain and White Matter Disease. 2001;1129(November 2000):1126-1129.

64. De Bazelaire CMJ, Duhamel GD, Rofsky NM, Alsop DC. MR Imaging Relaxation Times of Abdominal and Pelvic Tissues Measured in-vivo at 3.0T: preliminary results. *Radiology*. 2004;230:652-659.

65. Medved M, Sammet S, Yousuf A, Oto A. MR imaging of the prostate and adjacent anatomic structures before, during, and after ejaculation: qualitative and quantitative evaluation. 2014;271(2).

66. Gibbs P, Pickles MD, Hons BHS, Turnbull LW. Diffusion Imaging of the Prostate at 3.0 Tesla. 2006;41(2):185-188.

67. Tamada T, Sone T, Toshimitsu S, et al. Age-Related and Zonal Anatomical Changes of Human Prostatic Tissues. 2008;556:552-556. doi:10.1002/jmri.21117

68. Benjamini D, Basser PJ. Use of marginal distributions constrained optimization (MADCO) for accelerated 2D MRI relaxometry and diffusometry. *J Magn Reson*. 2016;271:40-45.

69. Kim D, Doyle EK, Wisnowski JL, Kim JH, Halder JP. Diffusion-relaxation correlation spectroscopic imaging: A multidimensional approach for probing microstructure. *Magn Reson Med*. 2017;78(6):2236-2249.

70. Zhang Y, Wells SA, Hernando D. Stimulated echo based mapping (STEM) of T1, T2, and apparent diffusion coefficient: Validation and protocol optimization. *Magn Reson Med*. 2018;(January 2018). doi:10.1002/mrm.27358

71. Zhang Y, Wells SA, Roldán-Alzate A, Hernando D. Simultaneous T1, T2 and ADC Mapping in Prostate Cancer and BPH using STimulated-Echo based Mapping (STEM). In: *Proc. Intl. Soc. Mag. Reson. Med. 27*. ; 2019:994.

72. Gudbjartsson H, Patz S. The Racian Distribution of Noisy MRI Data. *Magn Reson Med*. 1995;34(6):910-914.

73. Aja-fernández S, Pie T. Spatially variant noise estimation in MRI : A homomorphic approach. 2015;20:184-197. doi:10.1016/j.media.2014.11.005

74. Kim CK, Park BK, Kim B. High-b-value diffusion-weighted imaging at 3 T to detect prostate cancer: Comparisons between b values of 1,000 and 2,000 s/mm2. *Am J Roentgenol*. 2010;194(1):33-37. doi:10.2214/AJR.09.3004

75. KITAJIMA K, KAJI Y, KURODA K, SUGIMURA K. High b-value Diffusion-weighted Imaging in Normal and Malignant Peripheral Zone Tissue of the Prostate: Effect of

Signal-to-Noise Ratio. *Magn Reson Med Sci*. 2008;7(2):93-99. doi:10.2463/mrms.7.93

76. Kitajima K, Takahashi S, Ueno Y, et al. Clinical utility of apparent diffusion coefficient values obtained using high b-value when diagnosing prostate cancer using 3 tesla MRI: Comparison between ultra-high b-value (2000 s/mm 2) and standard high b-value (1000 s/mm 2). *J Magn Reson Imaging*. 2012;36(1):198-205. doi:10.1002/jmri.23627

77. Ueno Y, Kitajima K, Sugimura K, et al. Ultra-high b-value diffusion-weighted MRI for the detection of prostate cancer with 3-T MRI. *J Magn Reson Imaging*. 2013;38(1):154-160. doi:10.1002/jmri.23953

78. Chenevert TL, Lauren D, Taylor JMG, et al. Diffusion magnetic resonance imaging: an early surrogate marker of therapeutic efficacy in brain tumors. *J Natl Cancer Inst*. 2000;92(24):2029-2036.

79. Vederine FE, Wessa M, Leboyer M, Houenou J. A meta-analysis of whole-brain diffusion tensor imaging studies in bipolar disorder. *Prog Neuro-Psychopharmacology Biol Psychiatry*. 2011;35(8):1820-1826. doi:10.1016/j.pnpbp.2011.05.009

80. Galbán CJ, Hoff BA, Chenevert TL, Ross BD. Diffusion MRI in early cancer therapeutic response assessment. *NMR Biomed*. 2017;30(3). doi:10.1002/nbm.3458

81. Feuerlein, S Davenport, MS Krishnaraj, A, Merkle, EM Gupta R. Computed high b-value diffusion-weighted imaging improves lesion contrast and conspicuity in prostate cancer. *Prostate Cancer Prostatic Dis*. 2015;18:155-160.

82. Ning P, Shi D, Sonn GA, et al. The impact of computed high b-value images on the diagnostic accuracy of DWI for prostate cancer: A receiver operating characteristics analysis. *Sci Rep*. 2018;8(1):1-9. doi:10.1038/s41598-018-21523-6

83. Barrett T, Priest AN, Lawrence EM, et al. Prostate Tissue Apparent Diffusion Coefficient

as a Method for Quantifying DWI of the Prostate. 2015;(December):585-593. doi:10.2214/AJR.15.14338

84. Park BK, Kim B, Ck K, Bk P, Kim B. Diffusion-Weighted MRI at 3 T for the Evaluation of Prostate Cancer. 2010;(June):1461-1469. doi:10.2214/AJR.09.3654

85. Teruel JR, Cho GY, Rt MM, et al. (STEAM-DTI) with Varying Diffusion Times as a Probe of Breast Tissue. 2016. doi:10.1002/jmri.25376

86. von Deuster C, Stoeck CT, Genet M, Atkinson D, Kozerke S. Spin echo versus stimulated echo diffusion tensor imaging of the in vivo human heart. *Magn Reson Med*. 2016;76(3):862-872. doi:10.1002/mrm.25998

87. Lemberskiy G, Fieremans E, Veraat J, Deng F-M, Rosenkrantz AB, Novikov DS. Characterization of prostate microstructure using water diffusion and NMR relaxation. *Front Phys*. 2018;118(24):6072-6078. doi:10.1002/cncr.27633.Percutaneous

88. Moulin K, Aliotta E, Ennis DB. Effect of flow - encoding strength on intravoxel incoherent motion in the liver. 2019;(June 2018):1521-1533. doi:10.1002/mrm.27490

89. Van AT, Cervantes B, Ogino T, et al. Partial velocity-compensated diffusion encoding for combined motion compensation and residual vessel signal suppression in liver DWI. In: *Proc. Intl. Soc. Mag. Reson. Med. 26*. ; 2018:0079.

90. Guiu B, Cercueil J. Liver diffusion-weighted MR imaging : the tower of Babel ? 2017;(2011):463-467. doi:10.1007/s00330-010-2017-y

91. Hamilton G, Middleton MS, Hooker JC, et al. In Vivo Breath-Hold 1 H MRS Simultaneous Estimation of Liver Proton Density Fat Fraction , and T 1 and T 2 of Water and Fat , With a Multi-TR , Multi-TE Sequence. 2015. doi:10.1002/jmri.24946

92. Ozaki M, Inoue Y, Miyati T, et al. Motion Artifact Reduction of Diffusion-Weighted MRI

of the Liver : Use of Velocity-Compensated Diffusion Gradients Combined With Tetrahedral Gradients. 2013;178:172-178. doi:10.1002/jmri.23796

93. Zhou IY, Gao DS, Chow AM, et al. Effect of Diffusion Time on Liver DWI : An Experimental Study of Normal and Fibrotic Livers. 2014;1396:1389-1396. doi:10.1002/mrm.25035

94. Taouli B, Chouli M, Martin AJ, Qayyum A, Coakley F V., Vilgrain V. Chronic hepatitis: Role of diffusion-weighted imaging and diffusion tensor imaging for the diagnosis of liver fibrosis and inflammation. *J Magn Reson Imaging*. 2008;28(1):89-95. doi:10.1002/jmri.21227

95. Kim T, Murakami T, Takahashi S, Hon M, Tsuda K, Nakamuna H. Diffusion-Weighted Echoplanar MR Disease. 1999;(August):393-398.

96. Bruegel M, Holzapfel K, Gaa J, et al. Characterization of focal liver lesions by ADC measurements using a respiratory triggered diffusion-weighted single-shot echo-planar MR imaging technique. *Eur Radiol*. 2008:477-485. doi:10.1007/s00330-007-0785-9

97. Cui Y, Dyvorne H, Besa C, Cooper N, Taouli B. IVIM diffusion-weighted imaging of the liver at 3.0 T : Comparison with 1.5 T. *Eur J Radiol Open*. 2015;2:123-128. doi:10.1016/j.ejro.2015.08.001

98. Dyvorne H, Jajamovich G, Kakite S, Kuehn B, Taouli B. Intravoxel incoherent motion diffusion imaging of the liver : Optimal b-value subsampling and impact on parameter precision and reproducibility. *Eur J Radiol*. 2014;83(12):2109-2113. doi:10.1016/j.ejrad.2014.09.003

99. Beltran J, Johnson G. Fat Suppression in MR Imaging : Techniques. 1999:373-382.

100. Mazaheri Y, Vargas HA, Nyman G, Shukla-Dave A, Akin O, Hricak H. Diffusion-

weighted MRI of the prostate at 3.0 T: Comparison of endorectal coil (ERC) MRI and phased-array coil (PAC) MRI-THE impact of SNR on ADC measurement. *Eur J Radiol*. 2013;82(10):e515-e520. doi:10.1016/j.ejrad.2013.04.041

101. Rosenkrantz AB, Chandarana H, Pfeuffer J, et al. Zoomed echo-planar imaging using parallel transmission : impact on image quality of diffusion-weighted imaging of the prostate at 3T. 2015;(June 2014):120-126. doi:10.1007/s00261-014-0181-2

102. Ohgiya Y, Suyama J, Seino N, et al. Diagnostic accuracy of ultra-high- b -value 3 . 0-T diffusion-weighted MR imaging for detection of prostate cancer. *J Clin Imaging*. 2012;36(5):526-531. doi:10.1016/j.clinimag.2011.11.016

103. Korn N, Kurhanewicz J, Banerjee S, Starobinets O, Saritas E, Noworolski S. Reduced-FOV excitation decreases susceptibility artifact in diffusion-weighted MRI with endorectal coil for prostate cancer detection. *Magn Reson Imaging*. 2015;33(1):56-62. doi:10.1016/j.mri.2014.08.040

104. Fedorov A, Tuncali K, Panych LP, et al. Segmented diffusion-weighted imaging of the prostate : Application to transperineal in-bore 3 T MR image-guided targeted biopsy. *Magn Reson Imaging*. 2016;34(8):1146-1154. doi:10.1016/j.mri.2016.05.012

105. Barth BK, Cornelius A, Nanz D, Eberli D, Olivio F. Diffusion-Weighted Imaging of the Prostate. 2015;50(11):785-791. doi:10.1097/RLI.0000000000000184

106. Brendle C, Martirosian P, Schwenzer NF, et al. Diffusion-weighted imaging in the assessment of prostate cancer : Comparison of zoomed imaging and conventional technique. *Eur J Radiol*. 2016;85(5):893-900. doi:10.1016/j.ejrad.2016.02.020

107. Issa B. In Vivo Measurement of the Apparent Diffusion Coefficient in Normal and Malignant Prostatic Tissues Using Echo-Planar Imaging. 2002;200:196-200.

doi:10.1002/jmri.10139

108. Squillaci GME, Roma M Di, Mancino MCS. In vivo measurement of the apparent diffusion coefficient in normal and malignant prostatic tissue using thin-slice echo-planar imaging Misurazione in vivo del coefficiente apparente di diffusione nel tessuto prostatico sano e maligno con l ' utilizzo di sequenze EPI a strato sottile. 2006:1124-1133. doi:10.1007/s11547-006-0110-8

109. Roethke MC, Kuder TA, Kuru TH, et al. Evaluation of Diffusion Kurtosis Imaging Versus Standard Diffusion Imaging for Detection and Grading of Peripheral Zone Prostate Cancer. 2015;50(8):483-489.

110. Glazer DI, Hassanzadeh E, Fedorov A, et al. Diffusion-weighted endorectal MR imaging at 3T for prostate cancer : correlation with tumor cell density and percentage Gleason pattern on whole mount pathology. *Abdom Radiol*. 2017;42(3):918-925. doi:10.1007/s00261-016-0942-1

111. Reischauer C, Froehlich JM, Graf N, Padevit C, John H, Binkert CA. Bone Metastases from Prostate Cancer : Assessing Treatment Response by Using Diffusion- weighted Imaging and Functional Diffusion Maps — Initial Observations 1 Purpose : Methods : Results : 2010;257(2):523-531. doi:10.1148/radiol.10092469/-/DC1

112. Thoeny HC, Ross BD. Predicting and monitoring cancer treatment response with diffusion-weighted MRI. *J Magn Reson Imaging*. 2010;32(1):2-16. doi:10.1002/jmri.22167

113. Rabanillo I, Holmes JH, Guidon A, et al. ADC Measurement Accuracy in Quantitative Diffusion Phantoms using Reduced Field-Of-View and Multi-Shot Acquisitions. In: *In Proceedings of ISMRM Workshop on Breaking the Barriers of Diffusion MRI*. ; 2016.

114. Mazzoni LN, Lucarini S, Chiti S, Busoni S, Gori C, Menchi I. Diffusion-Weighted Signal Models in Healthy and Cancerous Peripheral Prostate Tissues : Comparison of Outcomes Obtained at Different b-values. 2014;518:512-518. doi:10.1002/jmri.24184

115. Babourina-brooks B, Cowin GJ, Wang D. Diffusion-weighted imaging in the prostate : an apparent diffusion coefficient comparison of half-Fourier acquisition single-shot turbo spin-echo and echo planar imaging. *Magn Reson Imaging*. 2012;30(2):189-194. doi:10.1016/j.mri.2011.09.024

116. Pierpaoli C, Sarlls J, Nevo U, Basser PJ, Horkay F. Polyvinylpyrrolidone (PVP) water solutions as isotropic phantoms for diffusion MRI studies. In: *In Proc Intl. Soc. Magn. Reson. Med*. ; 2009:1414.

117. Giavarina D. Understanding Bland Altman analysis. *Biochem Medica*. 2015;25(2):141-151.

118. Gill AB, Czarniecki M, Gallagher FA, Barrett T. A method for mapping and quantifying whole organ diffusion- weighted image distortion in MR imaging of the prostate. *Sci Rep*. 2017;(September):1-11. doi:10.1038/s41598-017-13097-6

119. Thierfelder KM, Scherr MK, Notohamiprodjo M, Weiß J, Theisen D. Diffusion-weighted MRI of the Prostate : Advantages of Zoomed EPI with Parallel-transmit-accelerated 2D-selective Excitation Imaging. 2014:3233-3241. doi:10.1007/s00330-014-3347-y

120. Jones DK, Basser PJ. " Squashing Peanuts and Smashing Pumpkins ": How Noise Distorts Diffusion-Weighted MR Data. 2004;993:979-993. doi:10.1002/mrm.20283

121. Scott AD, Nielles-vallespin S, Ferreira PF, Mcgill L, Pennell DJ, Firmin DN. The effects of noise in cardiac diffusion tensor imaging and the benefits of averaging complex data. 2016;(July 2015):588-599. doi:10.1002/nbm.3500

122. Thoeny HC, Ross BD. Predicting and Monitoring Cancer Treatment Response with Diffusion-Weighted MRI. 2010;16:2-16. doi:10.1002/jmri.22167

123. Chan JHM, Tsui EYK, Luk SH, et al. Diffusion-weighted MR imaging of the liver: Distinguishing hepatic abscess from cystic or necrotic tumor. *Abdom Imaging*. 2001;26(2):161-165. doi:10.1007/s002610000122

124. Barral M, Taouli B, Guiu B, et al. Diffusion-weighted MR imaging of the Pancreas. *Radiology*. 2015;274(1):45-63. doi:10.1148/radiol.14130778

125. Malayeri AA, El Khouli RH, Zaheer A, et al. Principles and Applications of Diffusion-weighted Imaging in Cancer Detection, Staging, and Treatment Follow-up. *RadioGraphics*. 2011;31(6):1773-1791. doi:10.1148/rg.316115515

126. Koh DM, Collins DJ. Diffusion-weighted MRI in the body: Applications and challenges in oncology. *Am J Roentgenol*. 2007;188(6):1622-1635. doi:10.2214/AJR.06.1403

127. Granata V, Fusco R, Catalano O, et al. Intravoxel incoherent motion (IVIM) in diffusion-weighted imaging (DWI) for Hepatocellular carcinoma : correlation with histologic grade. 7(48).

128. Granata V, Fusco R, Catalano O, et al. Early Assessment of Colorectal Cancer Patients with Liver Metastases Treated with Antiangiogenic Drugs : The Role of Intravoxel Incoherent Motion in Diffusion-Weighted Imaging. 2015:1-11. doi:10.1371/journal.pone.0142876

129. Chen X, Qin L, Pan D, et al. Liver diffusion-weighted MR imaging: reproducibility comparison of ADC measurements obtained with multiple breath-hold, free-breathing, respiratory-triggered, and navigator-triggered techniques. 2014;271(1).

130. Pathak R, Ragheb H, Thacker NA, et al. A data-driven statistical model that estimates

measurement uncertainty improves interpretation of ADC reproducibility : a multi-site study of liver metastases. *Sci Rep*. 2017;(June):1-10. doi:10.1038/s41598-017-14625-0

131. Zhang Y, Holmes JH. Motion - robust and blood - suppressed M 1 - optimized diffusion MR imaging of the liver. 2019;(September 2018):302-311. doi:10.1002/mrm.27735
132. Baxter GC, Patterson AJ, Woitek R, Allajbeu I, Graves MJ, Gilbert F. Improving the image quality of DWI in breast cancer: comparison of multi-shot DWI using multiplexed sensitivity encoding to conventional single-shot echo-planar imaging DWI. *Br J Radiol*. 2020;(July).
133. Chang H, Sundman M, Petit L, et al. NeuroImage Human brain diffusion tensor imaging at submillimeter isotropic resolution on a 3 Tesla clinical MRI scanner. *Neuroimage*. 2015;118:667-675. doi:10.1016/j.neuroimage.2015.06.016
134. Reconstructions LS, Hu Y, Ikeda DM, et al. Multishot Diffusion-Weighted MRI of the Breast With Multiplexed Sensitivity Encoding (MUSE) and Shot Locally. 2020:1-11. doi:10.1002/jmri.27383
135. Zhang Y, Holmes J, Rabanillo I, Guidon A, Wells S, Hernando D. Quantitative diffusion MRI using reduced field-of-view and multi-shot acquisition techniques: Validation in phantoms and prostate imaging. *Magn Reson Imaging*. 2018;51(September 2017):173-181. doi:10.1016/j.mri.2018.04.006
136. Lebel RM, Healthcare GE. Performance characterization of a novel deep learning-based MR image reconstruction pipeline.
137. Zhang K, Zuo W, Member S, Chen Y, Meng D. Beyond a Gaussian Denoiser : Residual Learning of Deep CNN for Image Denoising. *IEEE Trans Image Process*. 2017;26(7):3142-3155. doi:10.1109/TIP.2017.2662206

138. Bash S, Thomas M, Fund M, Lebel R, Tanenbaum L. Deep-Learning Reconstruction Improves Qualiity of Clinical Brain and Spine MR Imaging. In: *Radiological Society of North America 2019 Scientific Assembly and Annual Meeting*. ; 2019.

139. Hancu I, Lee S, Hulsey K, et al. Distortion Correction in Diffusion-Weighted Imaging of the Breast : Performance Assessment of Prospective , Retrospective , and Combined (Prospective 1 Retrospective) Approaches. 2017;253(April 2016):247-253. doi:10.1002/mrm.26328